THE UNIVERSITY *of* EDINBURGH

A Study of Nanosuspension Droplets

Free Evaporation and Electrowetting

By

Daniel Orejon

A thesis submitted for the Degree of Doctor of Philosophy

The University of Edinburgh, 2013

Declaration

The author declares that the work undertaken in this thesis has been carried out and composed by him unless stated otherwise. This work has not been submitted or accepted in the fulfilment of any other degree or qualification, at any other university.

Acknowledgments

This certainly is the least important scientific contribution included along this thesis but which is the most frequently read by colleges, family and friends, thus I will try to not forget any of you, who certainly have eased me through my PhD.

First of all I would like to thank the invaluable guidance, perseverance, understanding and advice received from my supervisor Professor Khellil Sefiane, during these years. Certainly he has been the main reference of this work and, both the trust, the freedom and the opportunity given to form part of this project, are truly appreciated.

I should not forget the precious help received from Professor Martin E. R. Shanahan whose support, discussions and demonstrations represent an enormous contribution to the work presented here. I truly thank Martin for letting me benefit from his experience and knowledge. Also I would like to show appreciation towards Dr. Vasileios Koutsos for his selfless help and support in different aspects during these years. Also my colleagues Alexandros and Jovana for their motivating and useful discussions related to the science presented here.

Once thanked those who have certainly contributed to the work presented in this thesis, I would like to acknowledge, also, all the people that have always been there for me showing their unconditional support. First of all, I would like to thank my family, in particular I dedicate this PhD to my parents Tere and Pepe, to my brother Javier and to my grandparents; who, despite the distance that stands between us, they have always been by my side offering their support and love.

In addition, I would like to thank all the people I have met since I moved to Edinburgh; flatmates, colleagues, friends and close friends, both inside and outside the university. You have been an invaluable source of support and amusement during these years, and you all have certainly made the daily routine more pleasurable and richer. To mention some: Pedro, Alex, David, Ares, Esme, Thimios, Isidora, Diego, Julieta, Wendy, Tommy, Michail, Apostolos, Emmanuela, Dimitrios, Jan, Mike, Juan, Molina and others.

Last but not the least important, to my friends back in Spain who know how much I love and I have missed during these years.

Layout Summary

The ubiquitous nature of wetting phenomenon, where a liquid comes into contact with a solid surface is commonly observed in everyday life. From rain droplets on windows (macro-) to dew droplets forming on a cobweb (micro-) or, to the condensation of water on atmospheric aerosol particles (nanoscale), the quotidian nature of wetting phenomenon is evident at any scale.

On other hand, equilibrium situations between solid surfaces and fluids are rarely found around us due to the particular nature of fluids being sensitive to changes in temperature and pressure, which stimulate shifts between phases. Paddle evaporation, formation of clouds and rain, dew droplets on leafs or melting of the poles are just some of the non-equilibrium examples present in everyday life where water molecules are subjected to a phase change, aiming to reach thermodynamic equilibrium between mentioned phases.

An experimental investigation on the evaporative behaviour of Nanofluids has been carried out aiming to uncover the fundamental physics and properties governing these novel fluids for heat transfer purposes or for the control of the patterns following the *free* evaporation. Another part to the project is the study of these fluids under Electrowetting (EW) conditions due to the ability of manipulating liquids without requiring mechanical parts at all. The enhancement in spreading for nanoparticle laden fluid due to adsorption of nanoparticles at the solid-liquid interface under an applied voltage besides the more homogeneous patterns with absence of rings-like stain are the most important findings reported within this thesis. The important contribution of this work in electrowetting field is evident.

In this thesis, the author aims to uncover the different mechanism governing the *free* evaporation of these novel fluids looking for the fundamental science underpinning the behaviour of these latter offering plausible applications where these fluids could be implemented.

Abstract

Evaporation and wetting of droplets are a phenomena present in everyday life and in many industrial, biological or medical applications; thus controlling and understanding the underlying mechanisms governing this phenomena becomes of paramount importance. More recently, breakthroughs in the fabrication of new materials and nanomaterials have led to the synthesis of novel nanoscale particulates that dispersed into a base fluid modify the properties of this latter. Enhancement in heat transfer or the self-assembly of the particles in suspension during evaporation, are some of the areas in which nanofluids excel. Since it is a relatively new area of study, the interplay particle-particle, particle-fluid or particle-substrate at the macro-, micro-, and nanoscale is yet poorly understood. This work is an essay to elucidate the fundamental physics and mechanisms of these fluids during *free* evaporation, of great importance for the manipulation and precise control of the deposits.

The evaporative behaviour of pure fluids on substrates varying in hydrophobicity has been studied and an unbalance Young's force is proposed to explain the effect of substrate hydrophilicity on the pinning and the depinning forces involved during droplet evaporation. On other hand, the addition of nanoparticles to a base fluid modifies the evaporative behaviour of the latter and: a more marked "stick-slip" behaviour is observed when increasing concentration on hydrophobic substrates, besides the longer pinning of the contact line reported on hydrophilic ones when adding nanoparticles. A deposition theory to explain the final deposits observed, for the outermost ring, after the complete vanishing of a 0.1% TiO_2-ethanol nanofluid droplet has also been developed. In addition, the evaporation of pinned nanofluid droplets on rough substrates at reduced pressures has been systematically studied.

A revisited Young-Lippmann equation is proposed as one of the main findings to explain the enhancement on electrowetting performance of nanoparticle laden fluid droplets when compared to the pure fluid case. On the other hand, of relevant importance is the absence of "stick-slip" behaviour and the more homogeneous deposits found after the complete evaporation of a nanofluid droplet under an external electric field applied when compared to *free* evaporation of these fluids.

Contents

Declaration ii

Acknowledgments iii

Layout Summary v

Abstract vi

Contents vii

List of Publications xi

Journals xi

Conferences, Workshops & Meetings xi

List of Figures xiii

List of Tables xx

Chapter 1: Introduction 1

Chapter 2: Background and Literature Review 9

2.1 Wetting 11

2.2 Droplet Evaporation 15

2.3 Evaporation of Colloidal Suspensions & Nanofluids 19

2.4 Electrowetting 27

2.5 Summary 32

Chapter 3: Experimental Techniques and Apparatus 35

3.1 Experimental Techniques 36

3.1.1 Droplet Shape Evolution 36
3.1.2 Electrowetting of Volatile Droplets 38
3.1.3 High Speed Camera 39
3.1.4 Additional Measurements 41
3.2 Fluids and Substrates 44
3.2.1 Fluids 44
3.2.2 Substrates 45
3.2.3 Chamber 47
3.2.4 Cleaning Procedure 47
3.3 Summary 48
Chapter 4: Effect of Substrate Hydrophobicity and Nanoparticle Concentration..... 49
4.1 Evaporation of Pure Fluids on Different Substrates 50
4.1.1 Water 51
4.1.2 Ethanol 52
4.2 Evaporation of TiO_2-water based Nanofluids 54
4.3 Evaporation of Al_2O_3-water based Nanofluids 60
4.4 Interpretation and Discussion..... 61
4.4.1 Pure Fluids 62
4.4.2 TiO_2-water Nanofluid 65
4.4.3 Al_2O_3-water Nanofluid 67
4.5 Summary 69
Chapter 5: Structuring of Nanoparticles during *Free* Evaporation..... 70
5.1 Evaporative Behaviour..... 71

5.2 Deposition at the Nanoscale 73

5.3 Deposition Theory 75

5.4 Quantitative Comparison and Discussion 79

5.5 Summary 82

Chapter 6: Evaporation of Nanofluid Droplets at Sub-Atmospheric Pressure 83

6.1 Evaporation Behaviour of Al_2O_3-water Nanofluid on Rough Aluminium 84

6.2 Evaporation Behaviour of Pure Water 87

6.3 Discussion 90

6.3.1 Al_2O_3-water Nanofluid 90

6.3.2 Water 92

6.3.3 Comparisson 93

6.3.4 Additional Considerations, Pinning of the Contact Line 95

6.4 Summary 96

Chapter 7: Electrowetting of Nanofluids, an Amended Young-Lippmann Equation 97

7.1 Effect of Dielectric Thickness for Pure Water 98

7.2 Effect of Nanoparticle Concentration 101

7.3 Dynamics of the Contact Line 103

7.4 Discussion 106

7.5 Summary 116

Chapter 8: Nanofluid Evaporation under Applied DC Electric Field 118

8.1 Evaporative Behaviour and Deposits 119

8.2 Electrophoresis versus Evaporation 124

8.2.1 Advective Flow 124

8.2.2 Electrophoresis 126

8.2.3 Comparison Between the Two Motions 128

8.2.4 Additional Considerations 131

8.3 Summary 132

Chapter 9: Conclusions and Further Work 133

9.1 Wetting and Dynamics of the Contact Line throughout Evaporation 134

9.2 Electrowetting 136

9.3 Future Work 137

References 139

List of Publications

Journals

Evaporation of nanofluid droplets with applied DC potential.
Orejon, D., K. Sefiane and M.E. R. Shanahan.
Journal of Colloids and Interface Science, Volume 407, Pages 29-38, ***2013****.*

Young-Lippmann equation revisited for nano-suspensions.
Orejon, D., K. Sefiane and M.E. R. Shanahan.
Applied Physics Letters, Volume 102, Issue 20, Pages 201601-1 to 201601-3, ***2013****.*

Stick-slip of evaporating droplets: substrate hydrophobicity and nanoparticle concentration.
Orejon, D., K. Sefiane and M.E. R. Shanahan.
Langmuir, Volume 27, Pages 12834-12843, ***2011***.

Nanoparticle deposits near the contact line of pinned volatile droplets: size, and shape revealed by atomic force microscopy.
Askounis, A., D. Orejon, V. Koutsos, K. Sefiane and M.E. R. Shanahan.
Soft Matter, Volume 7, Pages 4152-4155, ***2011***.

Conferences, Workshops & Meetings

Evaporation of Sessile Drops: Some Fundamental Parameters.
Shanahan, M.E.R. (Keynote Speaker), K. Sefiane, R. Moffat, D. Orejon, V. Koutsos and A. Askounis.
1st International Workshop on Wetting and evaporation: droplets of pure and complex fluids, Marseille, France 17th-20th June ***2013****.*

Dynamics of three phase contact lines of evaporating nanofluid droplets.
Sefiane, K., M.E. R. Shanahan and D. Orejon.
Workshop "Smart and Green Interfaces 2013 (Prague)" Prague, Czech Republic,21st-22nd March ***2013*** .

Electrowetting applied to nanofluids, suppressing stick-slip behaviour.
Orejon, D., K. Sefiane, M.E. R. Shanahan, Y. Li and A.J. Walton.
8th International Meeting on Electrowetting, Athens Greece, 21st -23nd June ***2012***.

Electrowetting applied to nanofluids, effect of dielectric layer and nanoparticle concentration.
Orejon, D., K. Sefiane and M.E. R. Shanahan.
5th International Workshop Bubble and Drop Interfaces 2012 (B&D 2012), Kraków, Poland, 20th-24th May ***2012***.

Pinned volatile droplets: Nanoparticle deposits near the contact line of pinned volatile droplets: size, and shape revealed by atomic force microscopy.
Askounis, A., D. Orejon, V. Koutsos, K. Sefiane and M.E. R. Shanahan.
5th International Workshop Bubble and Drop Interfaces 2012 (B&D 2012), Kraków, Poland, 20th-24th May ***2012***

Char for the Institute for Materials and Processes final year talks.
Orejon, Daniel (Chair IMP)
Graduate School of Engineering Postgraduate Research Conference, University of Edinburgh, Edinburgh, UK, 25th April ***2012***.

Droplet Evaporation Applied to Nanofluids (poster)
Orejon, D., K. Sefiane and M.E. R. Shanahan.
Graduate School of Engineering Postgraduate Research Conference, University of Edinburgh, Edinburgh, UK, 24th April ***2011***.

List of Figures

Figure 1. 1 – Different wetting situations including: self cleaning hydrophobic fabric, superhydrophobic substrate, antifogging coating, water interface modified by oil, reversing lens-like effect of water, and droplet resting on a hydrophobic and on a hydrophilic substrate. 4

Figure 1. 2 – 3D image of the TiO_2 nanoparticle deposits obtained by AFM (Figure 5. 2 (c)), drying of colloidal suspension, analogy between structuring of particles and Lego bricks, electrowetting of droplets, and liquid electro-optics based on electrowetting. 6

Figure 2. 1 – Different phenomena tackled in this work: wettability; drying colloidal suspensions such as inks, coffee and blood; and electrowetting. …….. 10

Figure 2. 2 - Schematic representation of Young's force balance at the triple contact line. ……..……..……..……...12

Figure 2. 3 – Different fluids on substrates varying in hydrophobicity: (a) deionized water-glass, (b) green pH 7 buffer-silicon, (c) TiO_2-water nanofluid-parylene and (d) green pH 7 buffer-Teflon. ……..……..……..14

Figure 2. 4 – Different evaporative regimes depending on the nature of the substrate and the fluid either at (a) constant contact radius (CCR), (b) constant contact angle (CCA) or (c) mixed mode [39]. ……..……..……. 16

Figure 2. 5 – Examples of deposits after the complete dry-out of different colloidal suspensions: blood serum [96], blue ink, TiO_2 nanoparticle deposits [97] , SiO_2 nanoparticle deposits at the macroscale, order -disorder transition at the TCL of micron-size spherical particles [98], cDNA microarray [99], and the well known coffee ring stain. ……..……..…….20

Figure 2. 6 – (a) Schematic representation of the evaporative behaviour of a droplet containing colloidal particles on hydrophobic and hydrophilic substrates [57] and (b) evaporative and capillary flux presented on the work of Deegan et al. [28] . ……... 22

Figure 2. 7 –Qualitative evaporative behaviour and patterns left after the complete evaporation, depending on nanoparticle concentration, observed during this experimental research. (a) Homogeneous deposit, (b) "stick-slip" behaviour and (c) a dot-like deposit. ……..……..……..25

Figure 2. 8 - Optical tweezers [110], electronic paper [116], lab-on-a-chip [2009 Finalist: Art in Science Award], water droplet as a lens [photograph: Gadi Fishel], variable-focus liquid lens [117], coloured pixels [114], electrowetting on paper [118] and hydrodynamic flows [68]. ……..……..……... 28

Figure 3. 1 – DSA100 from Krüss consists of: a moveable sample table, a back light, a CCD camera and dosing system and DSA1 v1.9 software snapshot. …….37

Figure 3. 2 – Electrowetting setup and DSA100. DC power supply, positive (red wire) and negative (black wire) electrodes, substrate holder and EWOD substrate are included. ……..……..……..…….. 38

Figure 3. 3 – (a) 3D view of typical experimental EWOD setup used to capture the instantaneous movement of the contact line when switching voltage On/Off. EWOD substrate, high-speed camera, and positive and negative electrodes connected to the substrate are included. (b) Cross-sectional view of the EWOD substrate and droplet is included. ……..……..……..……... 40

Figure 3. 4 – Contact angle and base radius versus time for deionized water at 30 volts during 7 cycles On/Off on $Cytop_{300}$. ……..……... 41

Figure 3. 5 - Height profiles of "smooth" silicon (thick solid red line) and "rough" Teflon (thin solid black line) showing the roughness in nanometres. Root mean square of both substrates has been calculated and included along. ……... 46

Figure 4. 1 – (a) Evolution of the contact radius, R (mm), and (b) evolution of the contact angle, θ (deg), for water on substrates ranging from the most hydrophilic to the most hydrophobic. ……..……..……51

Figure 4. 2 – (a) Evolution of the contact radius, R (mm), and (b) evolution of the contact angle, θ (deg), vs. time, t (seconds), on different substrates. …….. 53

Figure 4. 3 – (a) Evolution of contact radius, R (mm), and (b) contact angle, θ (deg), versus time, t (s), for 0.0005, 0.001, 0.005, and 0.01% of TiO_2-water concentration by weight besides the pure fluid case on silicon ($\theta_0 \approx 60°$). ……55

Figure 4. 4 – (a) Evolution of contact radius, R (mm), and (b) contact angle, θ (deg), versus time, t (s), for 0.01, 0.025, 0.05, and 0.1% of TiO_2-water concentration by weight besides the pure fluid case on Cytop ($\theta_0 \approx 110°$).…… 56

Figure 4. 5 – (a) Evolution of contact radius, R (mm), and (b) contact angle, θ (deg), versus time, t (s), for 0.01, 0.025, 0.05, and 0.1% of TiO_2-water concentration by weight besides the pure fluid case on Teflon ($\theta_0 \approx 115°$).…….. 57

Figure 4. 6 – Magnitudes of the jumps, δR (mm), of the contact line for the different TiO_2-water concentrations: 0.1%, 0.05%, 0.025, 0.01 and 0.001% on Teflon. Linear trends for each concentration are also included. ……..…….58

Figure 4. 7 - Change in contact angle, $\delta\theta$ (deg) for the different TiO_2-water concentrations: 0.1%, 0.05%, 0.025%, 0.01% and 0.001% on Teflon. Linear trends for each concentration are also included. 59

Figure 4. 8 - (a) Evolution of contact radius, R (mm), and (b) contact angle, θ (deg), versus time, t (s), for 0.001, 0.005, and 0.01% of Al_2O_3-water concentration by weight besides the pure fluid case on Cytop ($\theta_0 \approx 110°$).……..61

Figure 4. 9 – Schematic representation at the vicinity of the triple contact line region with the liquid interface at the equilibrium contact angle, θ_0, and at a slightly smaller angle, $(\theta_0 - \delta\theta)$. ……..……..……..…….62

Figure 4. 10 - The unbalance force right before the depinning of the contact line, $\delta\vec{F}$, calculated using Equation 4.3 on the following systems: glass*+aluminium-ethanol, C_4F_8-ethanol, glass-water, silicon-water, glass*+silicon-water, glass*+aluminium-water and parylene-water versus $\cos\theta_0$. Dotted line represents the minimum energy required for the depinning to ensue. ……..…… 64

Figure 4. 11 – Excess of free energy, $\delta\vec{G}$, for the first jump ($N \cdot 10^{-7}$) calculated for the different TiO_2-water nanofluid concentrations tested on Teflon using Equation 4.5 (squares) and Equation 4.6 (circles). Polynomial fits are included to illustrate trends. ……..……..……..……...67

Figure 4. 12 - Excess of free energy, $\delta\vec{G}$, for the first jump ($N \cdot 10^{-7}$) calculated for the different Al_2O_3-water nanofluid concentrations on Cytop and for the different TiO_2-water nanofluid concentrations on Teflon using Equation 4.5 and Equation 4.6. Polynomial fits are also included. ……..……..……..68

Figure 5. 1 – (a) Evolution of contact angle, θ (deg), and contact radius, R (mm), vs. time, t (seconds), for 0.1% TiO_2-ethanol and 0.2% TiO_2-ethanol and (b) inverted picture of solid substrate and deposits after complete evaporation. …….. 72

Figure 5. 2 - (a) 20 x 20 μm^2 topography image part of the outermost ring and (b) height (nm) and width (μm) of the profiles extracted from (a). (c) Three dimensional AFM image rotated 180º with respect to (a). ……..……...74

Figure 5. 3 – Schematic representation of the wetting front during a ‘stick’ period. 76

Figure 5. 4 – Shows height of the deposits, h (nm) versus time, t (seconds), calculated for the following characteristic lengths; $\varepsilon = 80nm$, $\varepsilon = 100nm$ and $\varepsilon = 150nm$ using Equation 5.7. ……..……..…… 80

Figure 5. 5 – Comparison between experimental and theoretical results. The curvature of the predictions stems from a variation of $\bar{J}$ as a function of $\lambda(\theta)$. …...81

Figure 6. 1 – Evolution of contact angle, θ (deg), base radius, R (mm), and volume, V (µl), versus time, t (sec) of 0.1% Al_2O_3-water nanofluid on rough Aluminium in nitrogen atmosphere at 80 kPa. ……..……..……..85

Figure 6. 2 - Rate of evaporation, dV/dt (µl/s), versus contact radius, R (mm), for 0.1% Al_2O_3-water in nitrogen atmosphere at 100, 80, 60, 40, 20, and 10 kPa. …….86

Figure 6. 3 – Evolution of contact angle, θ (deg), base radius, R (mm), and volume, V (µl), versus time, t (sec) of pure water on rough Aluminium in nitrogen atmosphere at 80 kPa. ……..……..……..... 88

Figure 6. 4 - Rate of evaporation, dV/dt (µl/s), versus contact radius, R (mm), for water at in nitrogen atmosphere at 100, 80, 60, 40, 20, 15, 10, 7 and 5 kPa. Rate of evaporation in air atmosphere is included for comparison. ……... 89

Figure 6. 5 – Rate of evaporation per base radius (µl/s/mm) represented versus radius, R (mm), for 0.1% Al_2O_3-water nanofluid in nitrogen atmosphere at different sub-atmospheric pressures (kPa). ……..…… 91

Figure 6. 6 –Evaporation rate per radius versus radius (µl/s/mm) for pure water case in nitrogen at different sub-atmospheric pressures (kPa). Results in atmospheric air are included for comparison. ……..……..……. 92

Figure 6. 7 – Log-log plot of rate of evaporation per unit of radius (µl/s/mm) versus pressure (kPa) for 0.1% Al_2O_3-water nanofluid and the pure water case in nitrogen

atmosphere. Power law correlation included for the pure water case to illustrate trend. ……..……..……..…… 93

Figure 6. 8 – Rate of evaporation per base radius (µl/s/mm) vs. base radius, R (mm), for water (solid symbols) and 0.1% Al_2O_3-water nanofluid (open symbols) in nitrogen atmosphere at different sub-atmospheric pressures. ……94

Figure 7. 1 – Electrowetting contact angle, $\theta(V)$ (deg), versus voltage, V (volts), for deionzied water on: $Cytop_{22}$ (squares), $Cytop_{300}$ (circles) and $Cytop_{500}$ (up triangles). Theoretical trends calculated using Equation 7.1 are shown to allow comparison (solid lines)..... 100

Figure 7. 2 – Electrowetting contact angle, $\theta(V)$ (deg), versus voltage, V (volts), on (a) $Cytop_{22}$ (squares), (b) $Cytop_{300}$ (circles) and (c) $Cytop_{500}$ (up-triangles) for; 0.1% (filled, dark yellow), 0.05% (filled-left, wine), 0.01% (filled-right, blue) and 0.001% (filled-up, red) TiO_2-water concentrations. Experimental (filled-down, green) and theoretical (straight solid line) values for deionized water, are included along for comparison 102

Figure 7. 3 – Contact radius evolution, R (mm), versus time, t (seconds), for (a) 0.001%, (b) 0.01% TiO_2-water and (c) for the same change in R for 0.01% TiO_2-water nanofluid. All R profiles were averaged from the first 7 experimental On/Off switching cycles on $Cytop_{22}$ (squares), $Cytop_{300}$ (circles) and $Cytop_{500}$ (up-triangles). 105

Figure 7. 4 – Theoretical trends for $\theta(V,\%)$ calculated using the proposed Equation 7.5 are presented for all three substrates and for the different TiO_2-water concentrations tested; 0.1% (dashed line), 0.05% (dot-dot-dashed line), 0.01% (dot-dashed line), 0.001% (dotted line) and for the pure water case (solid line) on $Cytop_{22}$, $Cytop_{300}$ and $Cytop_{500}$. 110

Figure 7. 5 – Electrowetting contact angle, $\theta_{(V,\%)}$ (degs), versus voltage, V (volts), for 0.1% (filled), 0.05% (filled-left), 0.01% (filled-right), 0.001% (filled-up) TiO_2-water nanofluid and for the pure water case (filled-down) on $Cytop_{22}$ (squares), $Cytop_{300}$ (circles) and $Cytop_{500}$ (triangles). 112

Figure 7. 6 - Average of 7 profiles of the contact radius, R (mm), versus time, t (seconds), for 0.01% TiO_2-water during the receding movement of the contact line at different voltages, (volts), on $Cytop_{22}$ (squares), $Cytop_{300}$ (circles) and $Cytop_{500}$ (up-triangles) besides theoretical trends calculated using Equation 7.7. 115

Figure 8. 1 – Substrate, droplet and electrode immersed into a 0.05% TiO_2-water nanofluid droplet under (a) EW conditions and (b) no EW for $t = 0$, $t = 1/4 t_{evap}$, $t = 2/4 t_{evap}$ and $t = 3/4 t_{evap}$. Base line and Circle Fitting Fit are included. 120

Figure 8. 2 - Evolution of the contact radius, R (mm) (squares), contact angle, θ (deg) (circles), and height of the droplet, h_0 (mm) (up-triangles), with time, t (seconds); (a) under electrowetting conditions and (b) under free evaporation for: 0.1%. Corresponding deposits also included. 121

Figure 8. 3 – As for Figure 8. 2, but for 0.05% TiO_2-water nanofluid. 121

Figure 8. 4 – As for Figure 8. 2, but for 0.025% TiO_2-water nanofluid. 122

Figure 8. 5 – As for Figure 8. 2, but for 0.01% TiO_2-water nanofluid. 122

Figure 8. 6 – Sketch of the different forces present during evaporation and under an electric field applied. 124

List of Tables

Table 3. 1 - Average surface tension liquid-gas and standard deviation for water and for the following TiO_2-water concentrations by weight: 0.001%, 0.01% and 0.1% at 15 ºC. 42

Table 3. 2 – Electrophoretic mobility and zeta potential for 0.01%, 0.05% and 0.1% of TiO_2 nanoparticle concentration by weight in deionized water. 44

Table 3. 3 - Equilibrium contact angle, θ_0, measured right after the deposition of the drop on the substrate ($t = 0$) for both water and ethanol on different substrates. 45

Table 7. 1 - K (1/volt^2) values for the different dielectric substrates varying in aFP thicknesses. ……..……..……..…… 107

Table 8. 1 - Electrophoretic, v_{ep}, advective, v_{adv}, and contact line, v_{CL}, speeds (µm/s), particle migration distance (m), and characteristic time, t_c (seconds), are included. ……..……..……..…… 130

Chapter 1: Introduction

The ubiquitous nature of wetting phenomenon, where a liquid comes into contact with a solid surface is commonly observed in everyday life. From rain droplets on windows (macro-) to dew droplets forming on a cobweb (micro-) or, to the condensation of water on atmospheric aerosol particles (nanoscale), the quotidian nature of wetting phenomenon is evident at any scale. Typically, when a liquid encounters a solid surface the liquid profile evolves until thermodynamic equilibrium, i.e. state of minimum energy, between the phases present at the triple contact line (TCL) is reached. This equilibrium depends on the physical and chemical binary interactions between the three different phases present: solid-liquid, liquid-gas and solid-gas.

It was more than two centuries ago when the English scientist Thomas Young [1] related the forces of attraction between the "particles" present within the different phases, i.e. liquid and solid molecules, to the observable contact angle adopted between a liquid and the same solid surface. Since then, many studies have been carried out to uncover the mechanisms present in phenomena such as wetting, dewetting, or adsorption of liquids onto solid substrates. Despite the major scientific contributions in the static and dynamics of the contact line, mostly by Dussan [2] and de Gennes [3], recent advances in the synthesis of new materials, miniaturization, or manipulation techniques, are constantly modifying and suggesting new interactions and mechanisms around interfacial phenomena. Understanding the physics and chemistry of this interfacial phenomena becomes of paramount importance for many pharmaceutical, biological or industrial applications such as self-cleaning surfaces [4], crop dusting [5], photoinduced materials [6], waterproofing, superspreaders [7].

On other hand, equilibrium situations between solid surfaces and fluids are rarely found around us due to the particular nature of fluids being sensitive to changes in temperature and pressure, which stimulate shifts between phases. Paddle evaporation, formation of clouds and rain, dew droplets on leafs or melting of the poles are just some of the non-equilibrium examples present in everyday life where water molecules are subjected to a phase change, aiming to reach thermodynamic equilibrium between mentioned phases. Typically, liquids experience evaporation

when molecules near the surface have enough energy to undergo phase change from liquid to gas, provided that the surroundings are not saturated with the latter. On the contrary, if the energy of the gas molecules is not high enough, the opposite phenomenon takes place and gas molecules condense.

A phenomenon, at first sight, as simple as the evaporation of a water droplet on a surface, for instance after spilling some water on a desk, has received important attention in the past decades to try to understand the complex mechanisms and physics present at the macro and microscale during the phase change from liquid to gas [8-11]. Evaporation of liquid droplets on solid substrates is an intricate transient process where an exchange of mass and energy between phases takes place. This phenomenon depends on many factors such as; wettability controlled by the physical and chemical nature of the solid and liquid, adhesive forces within the liquid, composition of the surroundings, temperature, or pressure amongst others [1-3]. Despite all the work carried out in this topic, both experimentally and theoretically [10, 12-20], there is still much knowledge to be gained from the complete understanding of the interactions solid-liquid, liquid-gas or solid-gas in both wetting and droplet evaporation. Research carried out in this area has been beneficial in many industrial, biological or agricultural applications [3] such as two-phase heat transfer [5], spray drying [21], combustion engines, DNA stretching [22] or the characterization of solid surfaces [2] .

Another topic that has been under intensive research, for more than a decade now, is the evaporation of fluids containing particles in suspension or colloidal suspensions, which exhibit potential applications in different fields including crystallography [23], synthesis of new materials [24], self-assembly [25], electronics [26], optics or patterning [27]. Indeed, the analysis of the evaporative behaviour of colloidal suspensions and the deposits left after the complete dry-out, led Deegan et al. [28] to elucidate the main mechanism responsible for the mass transport within the droplet during evaporation of pinned volatile droplets. An advective liquid flow from the bulk of a droplet towards the self-pinned triple contact line to replenish the liquid evaporated was observed from the drying of a coffee droplet on a desk. How particles organize and self-assemble at the triple contact line during evaporation

depends on particle-particle, particle-liquid, particle-solid, solid-liquid and liquid-gas interactions amongst others. Understanding of these interplays becomes of great importance for the control and reproducibility of the patterns and deposits following *free* evaporation [29-33]. Due to the complex nature of the system: liquid laden with particles evaporating on a solid substrate, many studies have been conducted to address the physics and the mechanisms underpinning the evaporation of these suspensions [27, 34-39].

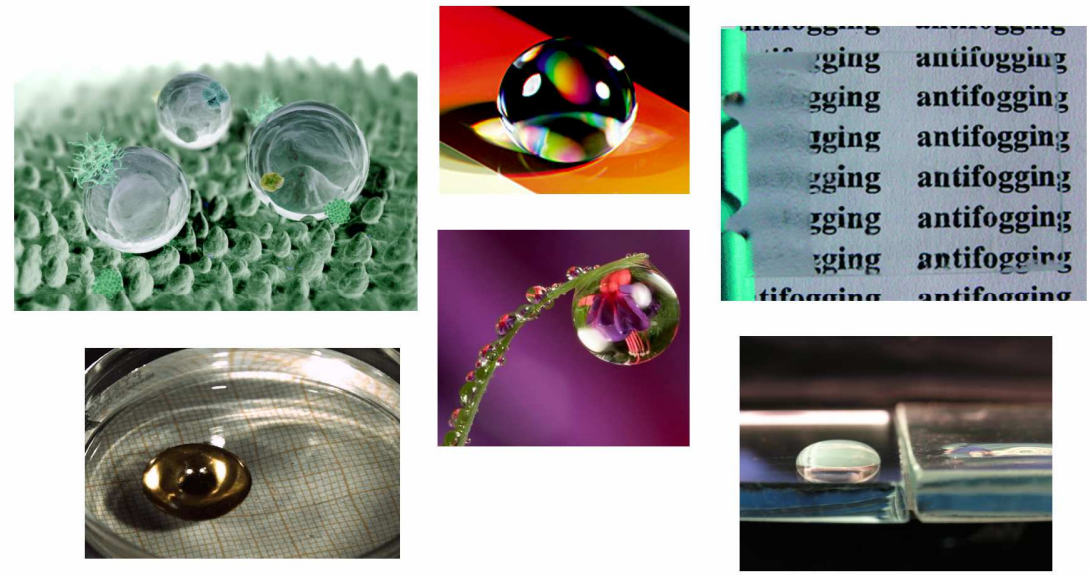

Figure 1. 1 – Different wetting situations including: self cleaning hydrophobic fabric, superhydrophobic substrate, antifogging coating, water interface modified by oil, reversing lens-like effect of water, and droplet resting on a hydrophobic and on a hydrophilic substrate.

In the same line of research, a new type of colloidal suspensions has emerged from the dispersion of particles with at least one dimension in the nanometre range into a base fluid [40-42]. The addition of these particles modifies the properties of the base fluid enhancing thermal conductivity [40], heat transfer [41], electrokinetic properties [43], wetting and spreading [44], or mass transfer [45] . In the last decade, numerous studies have suggested these novel fluids for potential applications in

boiling [46], optics [47], electronics [48], nanomedicine [49], solar energy [50], synthesis or for the fabrication of nanostructured materials [51] .

Despite the many applications where nanofluids can be implemented, in this work we are interested on the complex phenomenon of droplet evaporation. Special attention is paid to the effect of nanoparticles on the dynamics of the triple contact line and to the nanoparticle deposits left after the complete evaporation [26, 51-53]. Although this topic has been widely studied during the past fifteen years, mostly for colloidal suspensions, predicting the patterns left throughout evaporation is a complicated subject. Particles present in a particular system organize and structure differently depending on: the nature of both substrate and fluid or solvent [54], as well as on the size, concentration [55], shape [56] or type of nanoparticles in suspension [57], hydrophobicit of the substrate [58] or an external force applied [59]. Thus, in this experimental project, an experimental research has been undertaken to elucidate the fundamental physics, chemistry and engineering governing the *free* evaporation of pure fluids and fluids containing different nanoparticles in suspension, aiming for the complete understanding of this transient phenomenon for different applications.

The potential of manipulating liquid interfaces without mechanical components has also received the attention of the scientific community during the past decade [59, 60]. An external voltage applied to a droplet, Electrowetting (EW), has been proposed for the control of the droplet interface or for the manipulation of the meniscus interface in the case of capillaries by an external electric field [61]. Recent studies have reported this technique due to its promising potential applications, mainly in microfluidics [62], optics [63], internal mixing [64] or droplet surgery [65] amongst others. The combination of evaporation of colloidal suspensions under electrowetting conditions aims to shed further light in the mechanisms ruling the interactions particle-particle, particle-substrate, particle-liquid, or liquid-substrate under an external voltage applied [66-69]. Despites electrowetting was proposed more than a century ago, we are still far from the complete understanding of the manipulation of fluids under an external electric field applied [70-72].

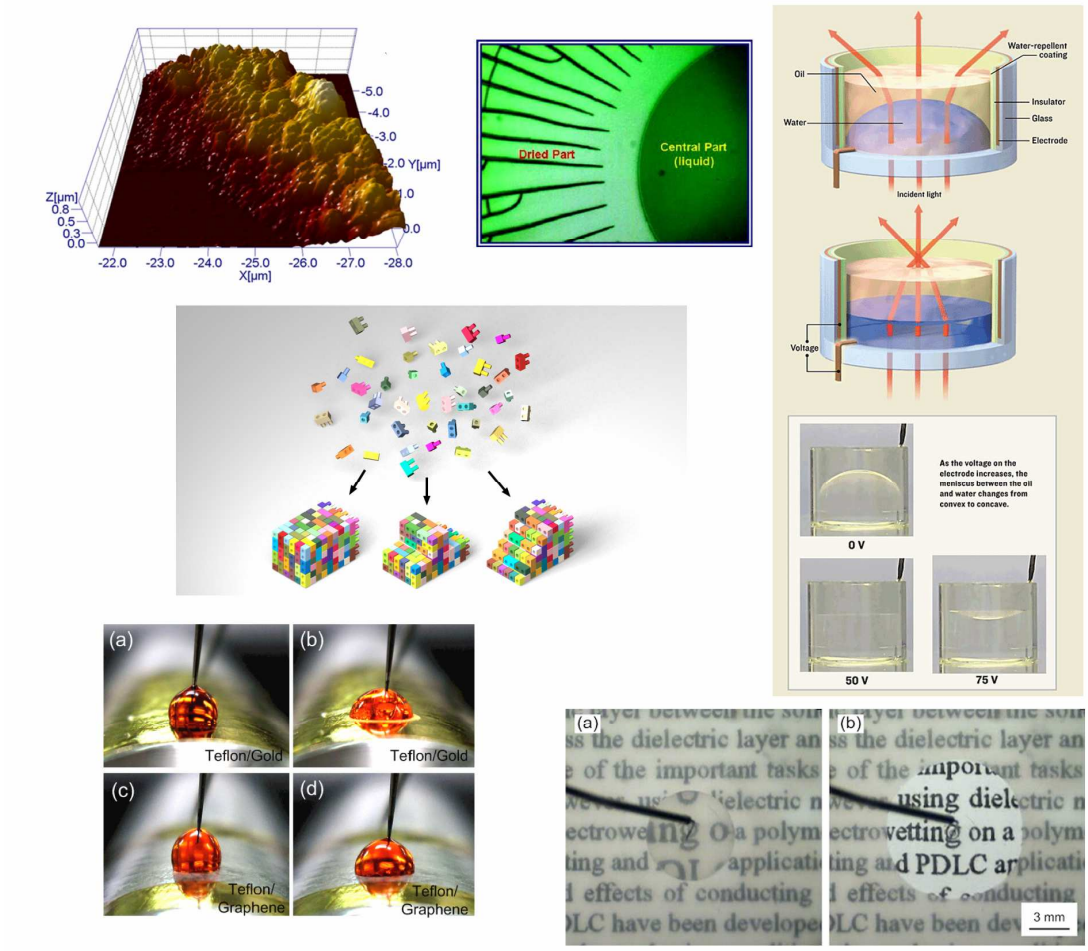

Figure 1. 2 – 3D image of the TiO_2 nanoparticle deposits obtained by AFM (Figure 5. 2 (c)), drying of colloidal suspension, analogy between structuring of particles and Lego bricks, electrowetting of droplets, and liquid electro-optics based on electrowetting.

This thesis is organized into 9 chapters. The first three chapters include the basic knowledge and background in wetting, evaporation and electrowetting as well as the experimental techniques and apparatus adopted during this experimental research. These three introductory chapters will ease the reader into the science underpinning the next five experimental parts. Finally, main conclusions are drawn in Chapter 9.

Chapter 1 includes a brief overview of wetting, evaporation, and electrowetting phenomena, underlining the most important findings and potential applications. In addition, a quick outline of what is found in each of the chapters of the present thesis

is included along. Chapter 2 brings background and knowledge required for the understanding of the physics, chemistry and engineering aspects surrounding wetting, evaporation and electrowetting phenomena. The structure is as follows; to begin, the fundamentals of wetting on solid substrates are introduced, which are closely linked with the droplet evaporative mode adopted during evaporation and depending on the hydrophobicity of the substrate. Third, remarks are made on the specific nature of fluids laden with nanoparticles and essential scientific background in this area is presented. Finally, an overview on the current status on electrowetting and electrowetting on dielectric including the most important findings and applications bring this chapter to a close. Chapter 3 includes the methodology and experimental techniques adopted this experimental research as well as the fluids, substrates and apparatus used.

In Chapter 4, the dynamics of the contact line and the pinning/depinning forces acting at the TCL of evaporating sessile droplets are studied for different pure fluids and fluids containing nanoparticles on substrates varying in hydrophobicity. The analysis of the deposits left after the complete evaporation of TiO_2-ethanol nanofluid droplets using atomic force microscope (AFM) is included in Chapter 5. In this chapter the evaporative behaviour observed at the macroscale is coupled with the deposits imaged at the nanoscale through a deposition theory. In Chapter 6, a systematic study on the evaporation of Al_2O_3-water nanofluids and deionized water on rough substrates has been conducted, to address the evaporative behaviour of nanofluid and pure fluid for completely pinned contact lines and at different sub-atmospheric pressures.

The second part of this experimental research involves the study of fluids and fluids laden with nanoparticles under an external electric voltage applied. First, the dynamics of the contact line under an external DC voltage applied (DC step voltage test as On/Off cycles) for deionized water and for different TiO_2-water nanofluid concentrations have been investigated. In addition to widen the experimental research presented in Chapter 7, three different electrowetting on dielectrics (EWOD) substrates varying in thickness of the insulating layer covering the dielectric electrode have been studied. Additionally, the complete evaporation of

TiO_2–water nanofluid droplets at different concentrations and under DC voltage applied has been undertaken in Chapter 8. A detailed discussion on the electrokinetic motion of the TiO_2 nanoparticles subjected to an external voltage is included along.

To conclude, this thesis represents an important contribution towards uncovering the mechanisms present during wetting, electrowetting and evaporation of fluids and fluids laden with nanoparticles, useful to both industry and academia. Experimental results coupled with extended discussions and theory have been presented to shed further light on these phenomena for future industrial, biological, medical or pharmaceutical applications.

In the next chapter, the main findings and the most relevant literature in wetting and evaporation of both pure fluids and colloidal suspensions related to this work, as well as the fundamentals of electrowetting and its limitations are presented.

Chapter 2: Background and Literature Review

Wetting and evaporation are a complex phenomena relevant to many industrial and everyday applications that have attracted the attention of the scientific community for many years. In order to ease the reader through the work included in this thesis, firstly, the fundamentals of wetting on solid substrates and the dependence of the equilibrium contact angle on the different interfacial tensions solid-liquid, liquid-gas and solid-gas are presented. Secondly, the different mechanisms involved during the evaporation of pure fluid droplets on substrates varying in hydrophobicity is studied, which will help to highlight the differences between the evaporative behaviour of pure fluids and nanoparticle-laden fluids. The particular behaviour of theses fluids containing particles in suspension requires a introduction of the main mechanisms governing the evaporation of these colloidal suspensions and a description of the potential applications in self-assembly, DNA stretching or bioanalysis, which are included third. The last part consists of the study of nanofluid droplets under an external voltage applied, therefore fundamentals of electrowetting and the evaporative behaviour of different fluids and colloidal suspensions under an applied external voltage are introduced last.

Figure 2. 1 – Different phenomena tackled in this work: wettability; drying colloidal suspensions such as inks, coffee and blood; and electrowetting.

2.1 Wetting

Wetting is defined as the ability of a liquid to wet either a solid surface or an immiscible liquid. Situations where a solid is wetted by a liquid are present all around us, from rain droplets on windows to paints, inks, crop dusting, or heat transfer. Due to the common nature of this phenomenon, understanding the different interactions between liquids and solids becomes crucial for many industrial, biological, agricultural or everyday applications [5, 14, 26, 73].

Wettability is governed by the different interfacial tensions between the phases present (solid-liquid-gas) and it has been used to characterize solid surfaces for years [1-3]. Interfacial tensions are typically neglected for fluids at the macroscale, although these forces become extraordinarily important when studying liquids at the microscale where gravitation forces are ruled out. Since this experimental work focuses on the study of the static and dynamics of dewetting of the contact line and on the interactions between liquid droplets and solid substrates during evaporation, an introduction to the fundamentals of wetting is essential.

It was more than two centuries ago since the publication of *"An essay on the cohesion of fluids"* by Thomas Young [1], which, despite all these years, is still considered as the foundation of modern wetting and capillary phenomena. Young observed the reproducibility of the contact angle adopted between droplets of the same liquid on the very same solid surface, which was described in terms of the interfacial tensions between the different phases present. Thereafter, using thermodynamics and the principle of minimum energy [74], Dupré [75] introduced the reversible work of adhesion to demonstrate the well known Young-Dupré equation, Equation 2.1 . On other hand, Gauss [76] combined Young's [1] theoretical description of surface tension with Laplace [77] mathematical approach to develop the Young-Laplace equation for capillary pressure between two immiscible liquids at capillary equilibrium .

Immediately after the gentle deposition of a droplet on an ideal, flat, rigid solid substrate, droplet profile evolves until thermodynamic equilibrium between the

phases present is reached. At equilibrium, the internal free energy of the system is minimized and different equilibrium profiles can be adopted depending on the physical and chemical properties of substrate [78], liquid and surroundings. A balance of the different interfacial forces acting at the triple contact line is represented in Figure 2. 2:

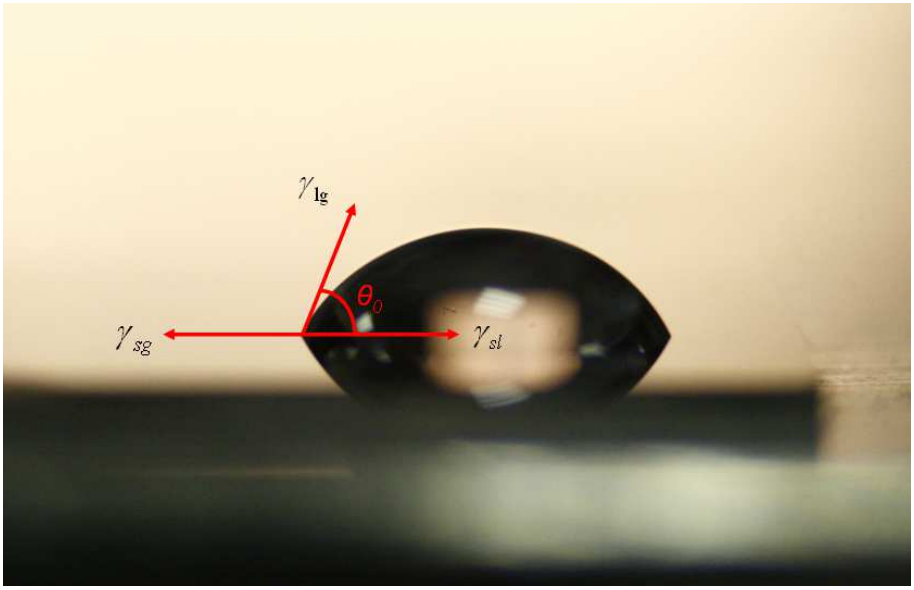

Figure 2. 2 - Schematic representation of Young's force balance at the triple contact line.

Where γ_{sg}, γ_{lg} and γ_{sl} are the different interfacial tensions solid-gas, liquid-gas and solid-liquid respectively, and θ_0 is the macroscopically equilibrium contact angle adopted by the droplet between the solid-liquid and the solid-gas interface, neglecting gravity effects. This force balance proposed more than two centuries ago by Thomas Young [1] and completed by Dupré [75] is still valid and widely used nowadays, Equation 2.1:

$$\frac{\gamma_{sg} - \gamma_{sl}}{\gamma_{lg}} = \cos\theta_0 \qquad (2.1).$$

Wetting and interfacial phenomena of droplets are considered as an area of research where the following disciplines; fundamental physics, chemistry and engineering come together, and which have attracted the attention of the scientific community for decades [5]. In the mid-sixties, Zisman [78] thoroughly reviewed wetting, spreading and adhesion of different fluids on a wide variety of substrates ranging from low- to high-energy surfaces. At this point the empirical linearity between $\cos\theta$ and the surface tension of the liquid for low energy substrates was proposed [78]. Between the seventies and eighties, the invaluable contributions of Dussan [2] and de Gennes [3] also led the static and dynamics of the contact line to a different level of understanding. Dussan proposed the idea of a microscopic contact angle at the vicinity of the triple contact line different from the macroscopic one, whereas de Gennes unified different concepts previously reported on physical chemistry, statistical physics and fluid dynamics, for the characterization of the static and dynamics of the contact line.

However, and despite all the work carried out in this topic, many of the mechanisms present during static, wetting, or dewetting of the contact line are still not completely understood. A brief description of wetting phenomena is included next. On an ideal substrate and at thermodynamic equilibrium a droplet can exhibit either complete or partial wetting depending on the properties of the phases present, i.e. interactions solid-liquid, liquid-gas and solid-gas. Typically on high-energy substrates, like metals, where surface tension solid-gas is greater than the sum of the other two surface tensions (liquid-gas and solid-liquid one), the triple contact line is pulled towards the solid-gas phase and the liquid spreads over the surface, i.e. complete wetting is observed [3]. On the other hand, partial wetting is reported for an observable finite contact angle between the solid-liquid and the liquid-gas interfaces. Furthermore within partial wetting regime, non-wetting is associated to contact angles greater than 90º whereas partial wetting is observed for contact angles ranging from 1º to 90º.

Additionally, depending on the wettability of the solid substrate, a surface can be considered hydrophilic when a water droplet exhibits either complete or partial

wetting (equilibrium contact angles for water below 90º), or hydrophobic when equilibrium contact angles are above 90º. Contact angle has been used for years to characterize the wettability of solid substrates [79]. The next figure illustrates different degrees of hydrophobicity ranging from hydrophilic to hydrophobic (from left to right):

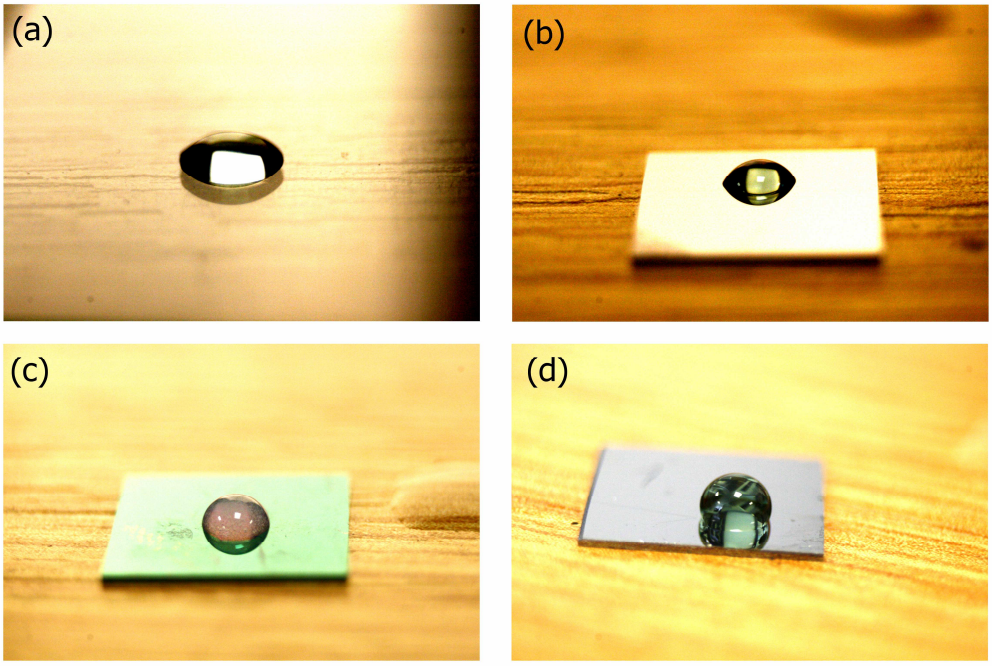

Figure 2. 3 – Different fluids on substrates varying in hydrophobicity: (a) deionized water-glass, (b) green pH 7 buffer-silicon, (c) TiO_2-water nanofluid-parylene and (d) green pH 7 buffer-Teflon.

It is worth noting that slightly different equilibrium contact angles can be observed when placing the same liquid on real surfaces, in contrast to ideal ones. These differences are due to the presence of physical or chemical heterogeneities or defects on the substrate such as cavities, bumps or scratches that lead the equilibrium contact angle to a range of values between the advancing and the receding one [80].

In the last century, many studies have been carried out to try to shed light on the complex world of wetting and interfacial phenomena between phases. For instance different mechanisms have been successfully reported to enhance the wettability of a

liquid on a substrate such as; the addition of surfactants to a base fluid reported by Marmur and Lelah more than three decades ago [81], or the development of anti-fog and self-cleaning superhydrophilic surfaces [7]. In addition, observing and mimicking the phenomena present in nature have led Neinhuis et al.[4] to the development of new superhydrophobic substrates based on the lotus leaf with an equilibrium contact angle for water greater than 150º. Non-wetting substrates are also important for self-cleaning applications or as water repellents for textiles and fibres.

On other hand, other techniques have also been successfully reported to control the droplet interface and to modify the extent of wetting by an external force applied. Electrowetting [82], dielectrowetting [83], or the development of new photoinduced materials [6] are some of the new techniques reported for the manipulation of the droplet interface in absence of mechanical parts.

Based on all the latter, understanding wettability and spreading becomes crucial for many industrial and everyday life applications and despite all the work carried out in this topic for more than two centuries, the interactions solid-liquid, liquid-gas and solid-gas are not completely understood yet and most of the scientific contributions can only be applied to particular solid-liquid systems.

2.2 Droplet Evaporation

Evaporation is also a phenomenon of great importance for many industrial or energy applications such as two-phase heat transfer [84], production of steam to power turbines, drying, or separation processes like mass transfer [85] amongst others. More precisely, in this work, we are interested in the evaporative behaviour of small volumes of liquid, i.e. the evaporation of microlitre droplets. For such small droplets, the main forces governing equilibrium contact angle are surface tension, heat and mass transfer, evaporative cooling, convection, and changes in surface tension [86].

Immediately after the deposition of a liquid droplet on a substrate and unless the atmosphere is saturated, a droplet will experience some evaporation, i.e. liquid

molecules are subjected to a phase change from liquid phase to gas phase, and heat is removed from the substrate. This loss of mass experienced by the liquid phase due to evaporation is observed as a change in droplet profile; either by a decrease in contact angle, a reduction in base radius or combination of both, depending mainly on the nature of the substrate. The different evaporation regimes proposed by Picknett and Bexon [8] are gathered in Figure 2. 4:

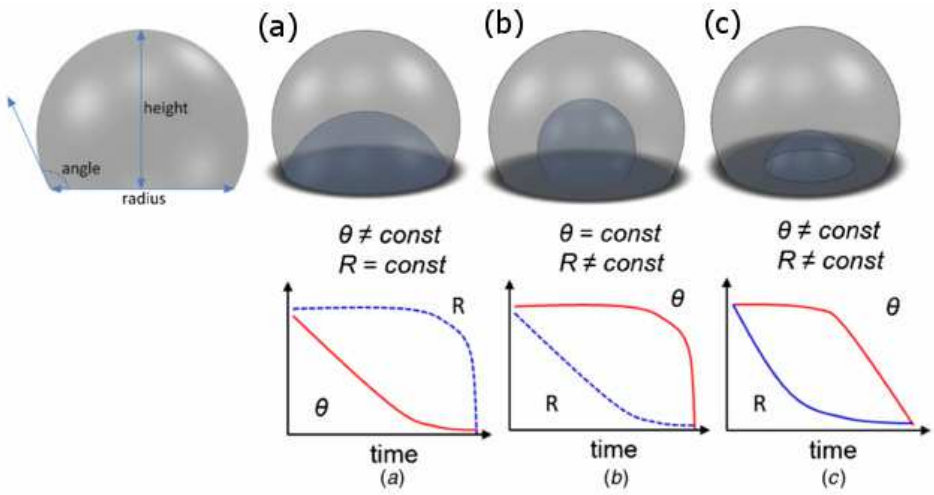

Figure 2. 4 – Different evaporative regimes depending on the nature of the substrate and the fluid either at (a) constant contact radius (CCR), (b) constant contact angle (CCA) or (c) mixed mode [39].

It was more than three decades ago when the different evaporative regimes, presented in Figure 2. 4, were observed [8], although it was not until few years later that the evaporation mode was linked to the wetting behaviour. Birdi and Vu [10], identified different evaporative modes depending on the wettability of the substrate, i.e. a droplet evaporates differently on a hydrophilic substrate than on a hydrophobic one . Typically on hydrophilic substrates, droplet evaporation proceeds at constant contact radius (CCR) leading to a steady rate of evaporation over time, this being greater for bigger droplet radiuses due to diffusion-driven evaporation as reported in literature [9, 14]. The constant rate of evaporation proposed for droplet evaporation at CCR was further supported by the work of Panwar et al. [16] where a linear

decrease of mass in time, for droplets evaporating at CCR, was tracked using a microbalance. It is worth mentioning that the linear relationship between evaporation rate and the radius of iodine spheres was already reported by Morse more than a century ago [87]. On the other hand, on smooth and hydrophobic substrates a different evaporative regime is reported. In this case, contact radius decreases monotonically and contact angle remains constant (CCA) leading to a non linear evolution of mass or volume loss in time as reported in literature by Mc Hale et al. [88] and Erbil and co-workers [13].

Of great importance is also the contribution of Bourgès-Monnier and Shanahan [11] who thoroughly studied the evaporative behaviour of two different fluids on substrates varying in hydrophobicity and four different stages of evaporation were identified. During the first stage, features of the droplet remain nearly unaltered since the surroundings are saturated with the evaporating liquid and practically no evaporation takes places. Once the atmosphere is not saturated any longer, a decrease in both contact angle and height of the droplet to account for the volume of liquid evaporated is noticed. Third, and depending on the substrate, base radius decreases while contact angle remains constant, and last, the mixed evaporative behaviour observed by Picket and Bexon [8] where both contact angle and base radius decrease in time, until the complete vanishing of the droplet is found [11].

Attending to droplet lifetime, this latter certainly depends on the evaporative mode either at CCR or at CCA dictated by the hydrophobicity of the substrate. For a given droplet volume, evaporation on hydrophilic substrates proceeds quicker due to lower equilibrium contact angle and therefore greater base radius than that adopted on hydrophobic ones. Since evaporation rate is proportional to the base radius, shorter timescales are observed for droplet evaporation on hydrophilic substrates when compare to low energy ones, as reported by Shanahan et al. [89]. This is also consistent with the work of Chandra et al. [90] where, for a given droplet volume, quicker evaporation was reported when using surfactants due to induced spreading . It is worth noting that irregularities and defects on the substrate play an important role in droplet evaporation. These heterogeneities can suppress, partially or completely, the dynamics of the contact line on hydrophobic substrates if roughness

and defects are great enough. The evaporation of water on superhydrophobic substrates at CCR mode has been further addressed by Gelderblom et al. [91].

From the theoretical point of view, a diffusion model to account for the transport of vapour molecules from the surface of a spherical droplet towards an infinite medium analogous to that of heat diffusion, was also proposed by Maxwell long time ago [92]. Almost a century later, Fuchs [93] confirmed Maxwell equation for stationary evaporation of millimetre sized spherical droplets with radii bigger than the mean free path of that of the vapour molecules, and it was given as Equation 2.2:

$$-\frac{dm}{dt} = -4\pi RD(c_s - c_\infty) \qquad (2.2),$$

where $-dm/dt$ is the loss of mass in time, R the spherical droplet radius, D the diffusion coefficient, and c_s and c_∞ the vapour concentration of saturation and that of the infinite medium respectively.

Thereafter Picknett and Bexon [8] tackled the more complex problem of evaporation of a liquid droplet wetting a solid substrate. A decrease in the rate of evaporation was observed due to there is lesser liquid-gas interface area sensitive to evaporation when compared to that of a sphere, i.e. smaller surface area for the diffusion of the vapour molecules. This reduction in evaporation rate was modelled by introducing a factor, $f(\theta)$, analogous to the one used for obtaining the electrostatic potential of an equiconvex lens. Mentioned factor is function of both droplet contact angle and radius of curvature [8]:

$$-\frac{dm}{dt} = -4\pi RD(c_s - c_\infty) f(\theta) \qquad (2.3).$$

Bringing together all the findings reported in this subsection, it is evident that evaporation of sessile droplets depends strongly on the evaporation mode either at constant contact angle or at constant contact radius dictated by the dynamics of the contact line, and these in turn depend on the nature of the substrate and the fluid, i.e. substrate wettability.

In this thesis the dynamics of dewetting are tackled in terms of competition between pinning forces anchoring the contact line to the substrate in one hand, and depinning forces due to the free energy gained by the droplet throughout evaporation on the other, which is included in Chapter 4 of the present thesis [58]. Uncovering the interactions and interfacial forces between the different phases (solid-liquid-gas) present during wetting and dewetting of evaporating droplets is of great importance for the complete comprehension of surface-based phenomena.

Once introduced the different mechanisms reported in literature for the evaporation of pure fluids on solid substrates, an overview of the mechanisms present during evaporation of volatile droplets containing particles in suspension is included next.

2.3 Evaporation of Colloidal Suspensions & Nanofluids

Colloidal suspensions can be defined as a disperse phase of solid particles in the micrometer range homogeneously mixed in a continuous medium or base fluid. This description was introduced more than 150 years ago by the Scottish scientist Thomas Graham [94]. Colloidal suspensions are also found all around us. Inks, paints, milk, tea, coffee, or blood, are some of the most common examples of these suspensions, which have been proposed for many industrial, food processing, self-assembly [26], pharmaceutical or biological applications [5] such as DNA stretching [14, 33] or as diagnosis tools [95]. Despite the numerous applications where colloidal suspensions can be implemented, in this work we are more interested on the science underpinning the mechanisms by which particles remain in suspension, interact with the solid substrate or organize at the TCL.

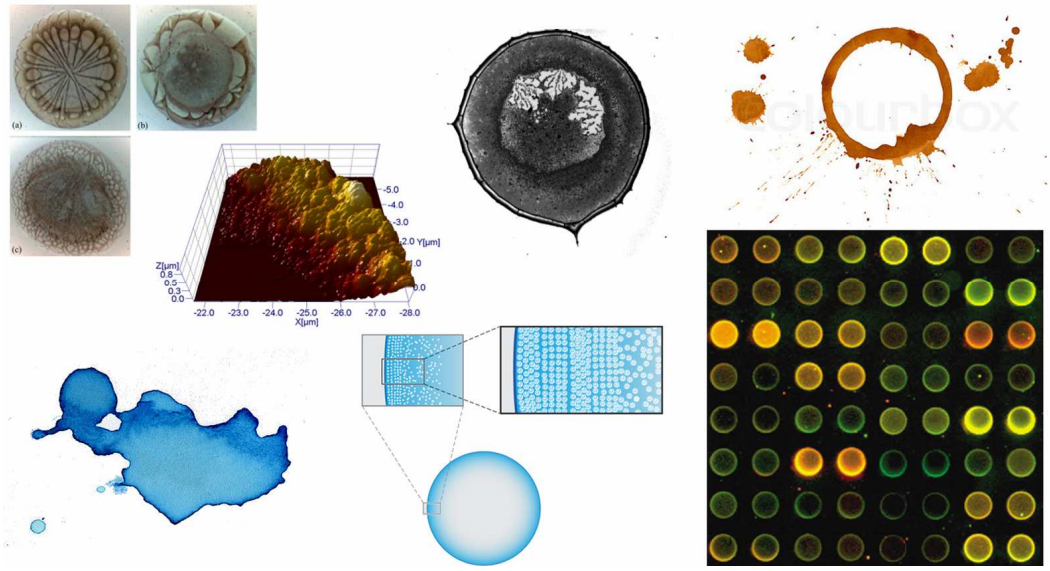

Figure 2. 5 – Examples of deposits after the complete dry-out of different colloidal suspensions: blood serum [96], blue ink, TiO_2 nanoparticle deposits [97] , SiO_2 nanoparticle deposits at the macroscale, order -disorder transition at the TCL of micron-size spherical particles [98], cDNA microarray [99], and the well known coffee ring stain.

It is predictable that the presence of particles of different shapes and sizes dispersed into a base fluid modifies the properties of the latter; enhancing thermal conductivity [100], increasing viscosity (predicted long ago by Einstein) [101], changing refractive index, or altering the evaporative behaviour, when compared to the pure fluid case [27, 46]. In this thesis special interest has been paid to the macroscopic evaporative performance of the droplet profiles and to the accumulation of particles at the TCL [58]. The latter essential to understand the internal mechanisms governing the patterns and deposits left during and after the complete dry-out of a droplet containing colloidal particles in suspension [97].

The relatively recent interest in the evaporation of colloidal suspensions has stemmed mostly since the work of Deegan et al. [28] and the analogy between evaporation of colloidal suspensions and the coffee ring stain left after the complete dry-out of coffee . It is foreseen that the evaporative behaviour of such suspensions becomes more intricate than the *simple* vanishing of the base fluid, and despite all the work carried out on this topic during the past years, the different interactions; particle-

particle, particle-fluid, particle-substrate and fluid-substrate are not yet fully understood and there is still considerable knowledge to be gained. Studying *free* evaporation of these suspensions potentially pursues the understanding of the internal mechanisms governing the motion of particles during evaporation. These particles in suspension have been reported to have a big impact on the dynamics of the contact line and for self-assembly [26, 27, 36].

The heuristic problem of particle deposition following *free* evaporation was tackled for the first time by Deegan et al. [102], who developed a mathematical model to demonstrate the averaged radial flow, J, and the velocity, $\bar{v}$, with which colloidal particles move from the bulk of the droplet towards a self-pinned triple contact line. In essence, for volatile droplets, there is a radial outward flow from the bulk of the droplet towards the TCL to replenish the liquid evaporated named capillary flow [102]. Capillary flows govern the internal flow of particles in suspension and therefore the macroscopic behaviour of the contact line. Since evaporation takes place mainly at the TCL [14], particles homogeneously suspended are dragged from the bulk towards the contact line prompting the accumulation of solute at the edge, thus hindering the receding movement of the contact line [27, 28]. The induced radial outward flow and the accumulation of particles at the droplet edge, besides the evaporative flux at the droplet surface are included in Figure 2. 6 (b):

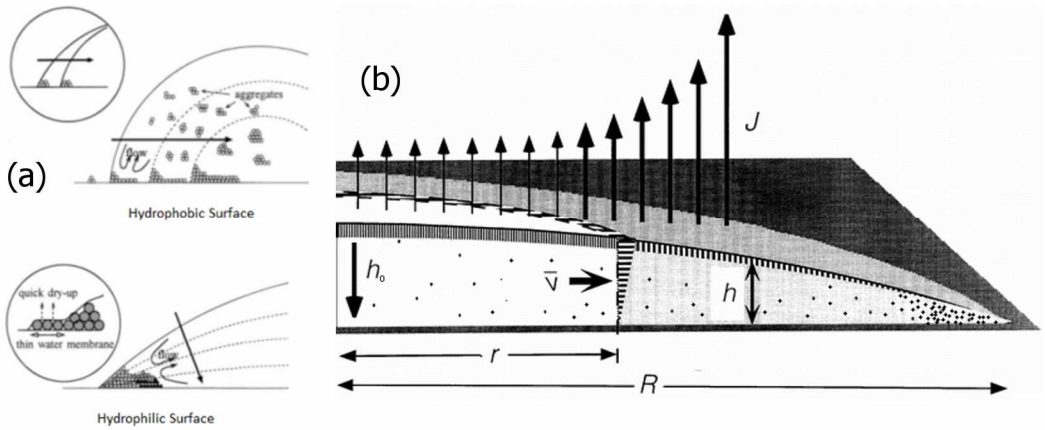

Figure 2. 6 – (a) Schematic representation of the evaporative behaviour of a droplet containing colloidal particles on hydrophobic and hydrophilic substrates [57] and (b) evaporative and capillary flux presented on the work of Deegan et al. [28] .

Equation 2.4 describes the radial outward velocity, $\bar{v}$, based on an vertically averaged radial flow [102]:

$$\bar{v}(r,t) = -\frac{1}{\rho r h}\int dr \cdot r\left(J(r,t)\sqrt{1+\left(\frac{\partial h}{\partial r}\right)^2} + \rho\frac{\partial h}{\partial t}\right) \qquad (2.4),$$

where h is the position of the liquid-gas interface, J the mass flux in Kg·m^2/s, r the radial position, and ρ the fluid density. The main mechanism of transport of solute towards the contact line is then identified.

Thereafter, Hu and Larsson [14] supported and completed the observations proposed by Deegan et al. [102] for the evaporation of pinned sessile droplets. These authors developed an analytical model, function of contact angle, for the description of the nonuniform distribution of both vapour and evaporative flux at the droplet surface during droplet evaporation. A good agreement between the proposed analytical solution, a finite element method (FEM) model and experimental results was reported [14]. In consequent publications, the same authors proposed and

demonstrated a lubrication theory to describe the velocity fields within the droplet; first, in absence of Marangoni stresses [103] and second, in presence of these stresses due to surface tension gradients caused mainly by a nonuniform temperature distribution along the droplet interface [18]. It was found that coffee ring patterns are a combination of; pinned contact line, accumulation of particles at the triple contact line and low recirculation of fluid within the bulk of the droplet, i.e. low Marangoni flow [104]. Theoretical and experimental contributions arising from the work of both groups, Deegan's and Hu and Larsson's, resulted vital towards a better understanding of the mechanisms governing the internal motion of both particles in suspension and liquid molecules during droplet evaporation

At this point, the addition of colloidal particles to a base fluid certainly modifies the evaporative behaviour of the pure fluid offering an attractive, efficient and costless mean to create desired patterns using *free* evaporation. It is worth mentioning that evaporation of colloidal suspensions and patterns created depend on the specific system studied, i.e. size, shape, concentration and nature of colloidal particles, type of fluid, characteristic and nature of the substrate, and properties of the surroundings.

More recently current advances in miniaturization and manufacturing techniques have led to the fabrication of novel nanoscale particulates, that added to a base fluid constitute a new class of colloidal suspensions called nanofluids [41, 42]. These nanofluids have been reported to exhibit unique thermal, electrical and mechanical properties. In addition a different evaporative behaviour when compared to those of the base fluid or of colloidal suspensions was observed. Addressing the dynamics of the contact line for these suspensions can help to elucidate the different mechanism controlling the interactions particle-particle, particle-fluid, particle-substrate, or fluid-substrate, the latter of great importance for the reproducibility of the deposits and patterns formed after the complete dry-out of these nanoparticle-laden liquids.

Using video microscopy, Wasan and Nikolov [44] observed for the first time the ordering of nanoparticles at the triple contact line. Mentioned ordering of the nanoparticles increases the disjoining pressure at the TCL, thus enhancing the extent of spreading of these nanosuspensions when compared to the base fluid. Another

imaging technique such as optical fluorescence microscopy led Wong et al. [105] to visualize three different rings according to sizes and nature of three different biologic substances. On other side, using atomic force microscopy (AFM), Askounis et al. [97] demonstrated the patterns and deposits left during the evaporation of colloidal suspensions and nanofluids, which are closely associated with the evaporative behaviour at the macroscale [106], the latter governed by the type, size and concentration of the particles present in the bulk . Based on all the later, the combination of different techniques at the nano-, micro- and macro-scale becomes crucial to understand and control the deposits for many biological, industrial, medical or pharmaceutical applications [107].

When looking into the evaporative behaviour of these novel fluids at the macroscale, different regimes of evaporation have been reported depending on nanoparticle concentration. On an ideal, smooth and solid substrate a nanofluid droplet may evaporate at CCR if the concentration of particles is high enough to prompt the complete pinning of the contact line, leading to ring-like but homogeneous stain [107]. On other hand, “stick-slip” of the contact line and a set of eccentric rings, preferentially pinned on one side, were reported by Moffat et al. [106] for the evaporation of 0.1% TiO_2-ethanol nanofluid droplet on hydrophobic substrates . Last, if the concentration of nanoparticles is decreased further close to 0%, similar evaporative behaviour to that of the pure fluid case with a decrease in the intensity of jumps and rings is observed on both hydrophobic and hydrophilic substrates [58]. The connection between evaporative behaviour and nanoparticle concentration is further discussed in Chapter 4 of the present work.

The different evaporative regimes described above and the patterns left depending on nanoparticle concentration are shown in Figure 2. 7:

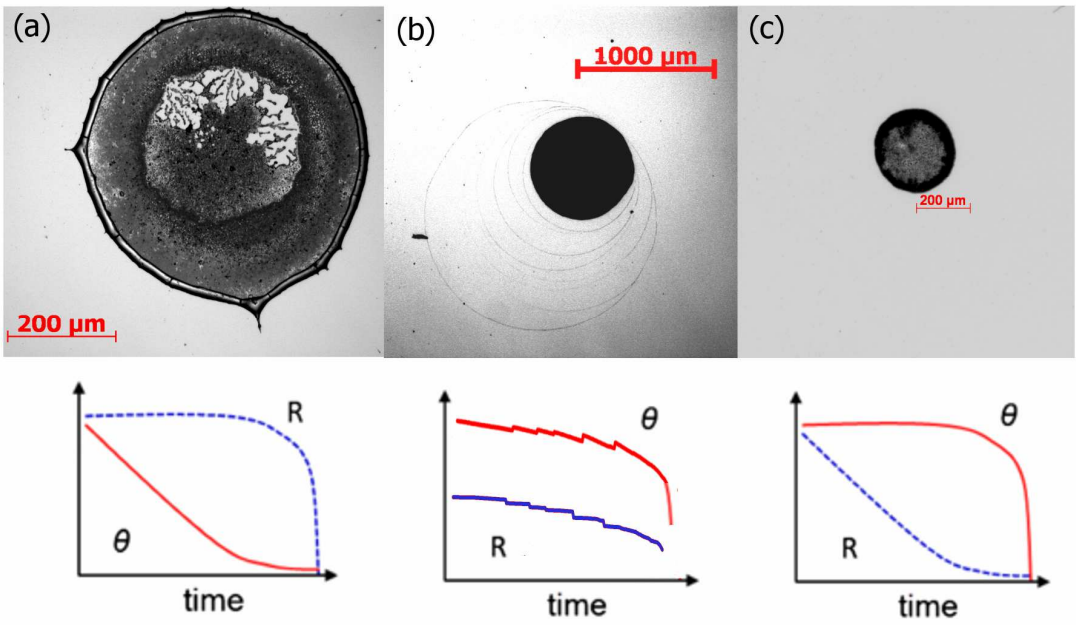

Figure 2. 7 –Qualitative evaporative behaviour and patterns left after the complete evaporation, depending on nanoparticle concentration, observed during this experimental research. (a) Homogeneous deposit, (b) "stick-slip" behaviour and (c) a dot-like deposit.

The potential of controlling the patterns left throughout *free* evaporation is evident. It is worth mentioning that Maenosono et al. [108] succeeded in reproducing nanometre size arrays by *free* evaporation of CdS and CdSe/Cd nanoparticles, only two years after the analogy established between evaporation of colloidal suspension and that of the coffee ring stain . On other hand, droplet geometry was successfully proven to separate and concentrate three different biological substances by size due to the curvature of the meniscus following *free* evaporation [105]. This size segregation represents potential applications as on-site separation and concentration for nanocromatography purposes. In addition, aiming to understand how colloidal particles in suspension perform and organize during evaporation, led Askounis et al. [97] to investigate the deposits left after the complete evaporation of a TiO_2-ethanol nanofluid droplet using AFM. A peak of 1 micron high and 5 microns wide was imaged and a deposition theory that agrees fairly well with experimental results was also demonstrated (see Chapter 5). On the same line of research, Marin et al. [98] visualized the advective motion of particles at the vicinity of the triple contact line, in

this case using microparticle image velocity (μPIV). In addition, analysis of the deposits scanning electron microscopy (SEM), presented an ordered region in a square and hexagonal fashion at the contact line that evolved into disorder when moving towards the centre of the deposits. This disorder region agrees with the high advective velocities found for the last period of evaporation named “rush hour”. All these studies aim to fully elucidate the phenomena underpinning the evaporative behaviour of colloidal suspensions and nanofluids, trying to understand the reproducibility of the patterns, and to control the deposits left throughout evaporation.

On other hand, since coffee ring stain is undesired in many industrial and biological applications [102, 105], in the past decade, the suppression of this coffee ring stain has been thoroughly investigated. Hu and Larson [104] were the first ones to report both experimentally, using fluorescent tracers, and theoretically that high Marangoni flows within the droplet can certainly reverse the coffee-ring stain . Bhardwaj et al. [38] looked into the different deposits left after the complete evaporation of TiO_2-water nanofluids at different pHs. Uniform layer, coffee ring, or a bump in the centre; were the types of structures found depending on the different electrostatic interactions and van der Waals forces altered when modifying the pH. Other authors reported the suppression of the coffee ring stain by using different shapes of particles dispersed. A more homogeneous deposit rather than the accumulation of particles at edge (coffee ring) was observed when using ellipsoids and spherical particles respectively [56]. In addition, Eral et al. [66, 109] successfully reported the suppression of the coffee ring stain under alternate current (AC) electrowetting conditions applied to a droplet containing polystyrene particles in the micrometer range.

It is clear then that the addition of nanoparticles to a base fluid changes the dynamics of the contact line and the deposits found at the macro-, micro- and nanoscale depending on the evaporative mode reported; constant contact radius, “stick-slip” or constant contact angle mode. In Chapter 4 and Chapter 5, an attempt to underline the most important mechanisms governing wetting and evaporation of pure fluids

besides the more complex evaporation of fluids laden with nanoparticles is included. Special attention is paid to the understanding of how nanoparticles organize and self-assembly during *free* evaporation.

2.4 Electrowetting

Although the interplay between liquid interfaces and electricity was observed by Gabriel Lippmann in 1875 [61], the ability to precisely manipulate and control small volumes of liquids without requiring mechanical parts has received important attention in the past decade [59, 60]. Optical tweezers [110], microheaters and patterned surfaces [111], acoustic [112] or electrochemical means [113], and electrowetting (EW) [59, 60], are some of the most recent techniques investigated for the manipulation of fluids without mechanically moving components. Amongst these latter, EW has been proposed as one of the most promising techniques for the manipulation of droplet interfaces for optical purposes [63, 82, 114], microfluidic applications [62], internal mixing [64], suppression of the coffee ring stain [109], droplet surgery [65] or for the harvesting of energy from mechanical sources [115].

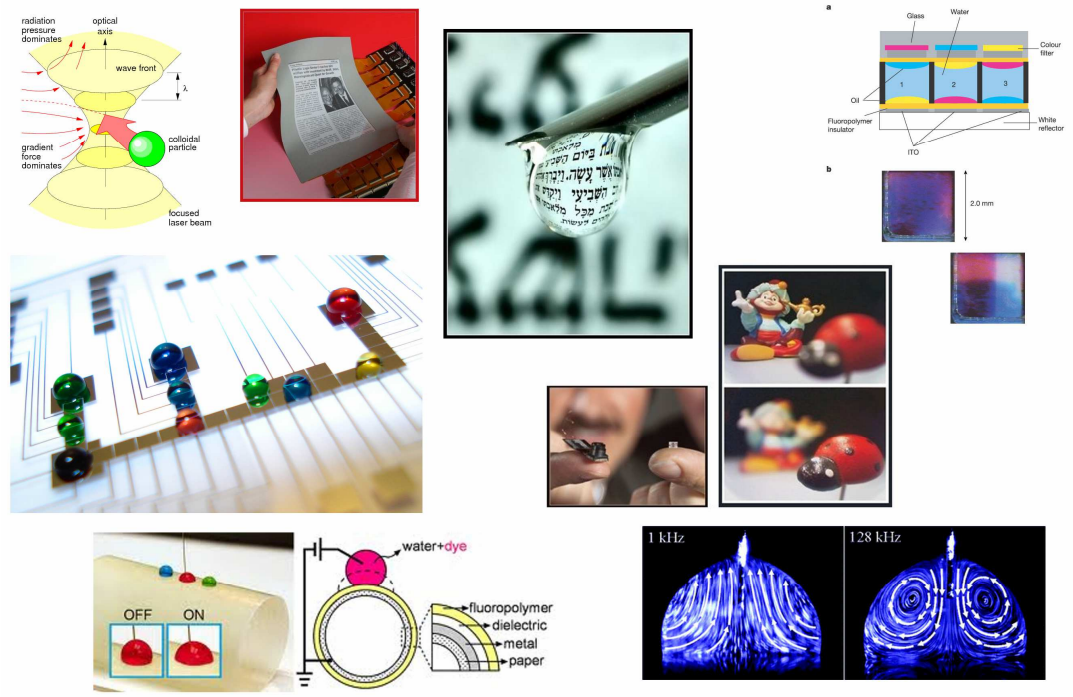

Figure 2. 8 - Optical tweezers [110], electronic paper [116], lab-on-a-chip [2009 Finalist: Art in Science Award], water droplet as a lens [photograph: Gadi Fishel], variable-focus liquid lens [117], coloured pixels [114], electrowetting on paper [118] and hydrodynamic flows [68].

The versatility and effectiveness, with which EW has been recently implemented in many research disciplines make this technique an attractive mean for the manipulation of the droplet interface and the control of the deposits following evaporation under an external force applied. Then a thorough study of the dynamics of spreading/receding of the contact line [119] as well as investigating the mechanisms present during the evaporation of nanoparticle-laden liquids under an external voltage applied [120], are expected to shed further light on the interactions particle-particle, particle-fluid, particle-substrate, and fluid-substrate, under an electric field applied .

Typically when an external voltage is applied to a droplet the thermodynamic equilibrium is further altered, the interfacial tension solid-liquid is modified and the substrate becomes more hydrophilic, i.e. contact angle decreases and contact line spreads. The interplay between electrical and capillary phenomena was firstly

observed by Gabriel Lippmann [61] in 1875, who demonstrated the accumulation of electric energy at the solid-liquid interface. This accumulation of energy or induced surface charge density, q, was proven [61] by applying Laplace equation, thermodynamics (principle of minimization of Gibbs free energy [121]) and electrochemical (Helmoholtz layer capacitance per unit of area) principles leading to $-q = \partial\gamma/\partial\varphi$, where γ is the interfacial tension and φ is the electric potential or voltage across the interface, henceforth referred to as V. Then integrating this accumulation of energy at the interface and combining it with Young-Dupré equation (Equation 2.1), the well-known Young-Lippmann equation for sessile droplets, Equation 2.5, is demonstrated:

$$\cos\theta(V) = \cos\theta_0 + \frac{1}{2}\frac{\varepsilon_r\varepsilon_0 V^2}{\gamma_{lg} d} \qquad (2.5),$$

where $\theta(V)$ is the contact angle under an applied voltage, V, θ_0 is the equilibrium contact angle, ε_r and ε_0 are the permittivities of the material and of free space respectively, and d is the thickness of the electrode.

On other hand, electrowetting problem can also be approximated following and electromechanical approach at the droplet surface while interfacial tensions remain unvaried. Mugele and Buehrle [122] demonstrated the effect of electric fringe fields at the vicinity of the contact line resulting in Maxwell stresses pulling the triple contact line outwards. At this point, a differentiation between the microscopic or *local* contact angle governed by interfacial tensions and independent of voltage, i.e. Young's angle, and the macroscopic or *apparent* one, which is well predicted by the Young-Lippmann equation was essential.

Although electrowetting phenomenon has been widely investigated during the past two decades, at the present there are still some special features that need to be elucidated. Contact angle saturation, deviation from the Young-Lippmann equation

when studying ionic fluids, suppression of contact angle saturation when using dielectrowetting, or enhancement in spreading for fluids laden with particles under an external electric field applied are some of the phenomena that need further investigation.

Regarding contact angle saturation, i.e. no further change in contact angle when increasing the voltage takes place; different works have been presented to try to explain this limitation. Quinn et al. [123] proposed a thermodynamic limit of stability related to the properties of the materials where the interfacial tension solid-liquid must always be positive. This approach was inconsistent with the electromechanical approach described by Mugele and Buehrle few years later [122]. Other authors pointed towards very strong electric fields that overcome the insulation capacity of the dielectric, like Papathanasiou and co-workers who succeeded in measuring leakage currents on the dielectric layer [124]. Aiming to understand the physics and mechanisms involved during contact angle saturation, McHale et al. [83] proposed the use of a nonuniform electric field, dielectrophoresis (DEP) to manipulate droplets of nonconductive liquids. While some authors reported contact angle saturation at 60º, McHale and co-workers managed to decrease the contact angle under electrowetting conditions down to 20º, due to the geometry of the electrodes and the type of electric field applied.

When comparing electrowetting performance between different fluids, it has been reported that ionic fluids and nanofluids behave, qualitatively, in a similar way as the pure fluid. Although in some cases, there is a quantitative deviation from the features predicted by the Young-Lippmann equation (Equation 2.5). Dash et al. [125] were the first ones to study electrowetting of Bi_2Te_3 nanoparticle suspensions observing different electrowetting behaviour when compared to ionic liquids. An enhancement in stability and the absence in contact angle saturation for these novel fluids, for the range of voltages tested, was found. Other authors like Millefiori and collaborators [69], investigated the electrowetting behaviour for different ionic liquids observing quantitative differences between these ionic liquids and the Young-Lippmann equation. Differences in electrowetting performance were explained in terms of; lower efficiency, different behaviour when comparing anionic or cationic fluids, and

asymmetry between positive and negative voltage. On other hand, Roques-Carmes et al. [126] looked into the electrowetting behaviour of quantum dots dispersed in water, observing, also, a quantitative deviation from the Young-Lippmann equation. In this particular case, an enhancement in electrowetting behaviour, i.e. greater changes in contact angle were observed for these nanosuspensions when compared to the pure fluid case.

In addition, electrowetting on dielectric (EWOD) substrates has been proven to provide a superior performance than traditional EW substrates. Initially designed to separate the planar solid electrode from the conductive liquid to block the direct exchange of electrons and thus preventing electrolysis; EWOD substrates have also been demonstrated to require very low-actuation voltages when compared to traditional EW substrates [127]. An insulating layer of an amorphous fluoropolymer (aFP) is deposited over the conductive electrode conferring the hydrophobicity and insulation properties required. This relatively new concept of EWOD substrates has driven recent interest in studying different configurations and materials, aiming to obtain substrates with high dielectric constants and good performance against dielectric breakdown [128, 129]. When studying EWOD, basic principles of electricity can be applied to account for the capacitances of the electrode and that of the insulating material [129].

Despite the interest on controlling droplet interface mainly for optical applications, uncovering the internal mechanisms present during the electrowetting of colloidal suspensions has received special attention in the past few years. Understanding the mechanism controlling evaporation of these suspensions under EW conditions definitely represents potential benefits for the manipulation and repeatability of the deposits left by drying. Ko et al. [68] reported hydrodynamics flows inside a droplet containing fluorescent polystyrene particles of 2 μm in diameter at different alternate current (AC) frequencies. Thereafter Mugele's group [64] studied the oscillating motion of the contact line, from high to low contact angle induced by different AC frequencies. The internal mixing of different fluorescent particles and proteins due to capillary waves generated from the continuous movement of the

contact line was successfully proven. Furthermore, the suppression of the coffee ring stain was effectively attained during the drying of volatile droplets containing particles in suspension for certain AC frequencies and voltages [66, 109].

In this work we are more interested in the effect of direct current (DC) voltage applied to microlitre droplets containing nanoparticles in suspension. The first observations regarding the connection between the behaviour of particles in suspensions and an external electric field applied can be dated back to two centuries ago. In 1809, Ferdinand Frederic Reuss [130] observed the migration of clay particles suspended in solution under DC voltage applied, named electrophoresis (EP). The fundamentals of this mechanism are based on the surface charge acquire by particles in suspension when suspended in a polar media. This has been proven for particles, cells and/or bacteria present in suspension, which are attracted towards the electrode with opposite charge under an applied DC electric field [131, 132]. Electrophoretic deposition (EPD) has emerged from the exploration of EP as a method for separating different particles and cells by charge or size [67, 132-134]. In this work, we propose electrokinetic transport as the main mechanism for the particle motion within a droplet rather than advective motion dragging the particles towards the contact line, Chapter 8. Thus uncovering the mechanisms present during the EW of nanofluid droplets under a DC electric field applied becomes of great importance for the control and manipulation of the deposits left during and after the complete dry-out.

2.5 Summary

It is evident that despites all the research carried out on the different topics presented within this thesis, many are still to be elucidated; the interactions and mechanisms governing the interplay particle-particle, particle-fluid, fluid-substrate and fluid-gas.

Regarding wetting phenomenon, the development of new materials, nanomaterials, fluids and substrates with novel and modified physicochemical properties has led to

propose new interactions and to reveal novel mechanisms between the different phases present. It is indubitable that wettability plays a crucial role on the static and on the dynamics of the contact line during both wetting and dewetting, which depends mainly on the hydrophilicity of the substrate and the properties of the fluid. Also wetting phenomenon has been found to be influenced by the presence of particles in suspension. Once again, singularities are found for a particular solid-liquid system, which have helped for the characterization solid substrates.

The main evaporative regimes described in this chapter depend on the forces involved during the pinning and the depinning of the contact line. Macroscopic evaporative performance of the contact line has been found to be different depending on the hydrophobicity of the substrate and also on the type of fluid. In the case of pure fluids, evaporation at CCA mode is reported on smooth and hydrophobic substrates, whereas on hydrophilic ones evaporation begins at CCR and the receding movement of the contact line can also be observed, if equilibrium contact angle is high enough. An unbalance Young force has been proposed to explain the pinning and depinning forces acting at the triple contact line on hydrophilic substrates.

On other hand, the addition of nanoparticles to a base fluid is found to modify the macroscopic droplet evaporative behaviour. The structuring and accumulation of nanoparticles at the triple contact line due to capillary flows was found to hinder the receding movement of the contact line. The effect of nanoparticle concentration and substrate hydrophobicity has been systematically studied and, the induced intrinsic energy barrier at the contact line impeding the receding movement of the latter has been seized. In addition, the structuring of nanoparticles at the triple contact line has been further revealed and a deposition theory that agrees fairly well with experimental results has been developed. Also the evaporative behaviour at sub-atmospheric pressures for pinned contact lines has been investigated for one nanofluid concentration and for the pure fluid case. Understanding *free* evaporation of these fluids offers potential applications for controlled deposition and patterning.

The second part of the present work deals with an external force applied to a nanofluid droplet. Electrowetting has been proposed as one of the most promising

techniques for the control of the droplet interface without requiring mechanical parts. It has been demonstrated that nanofluid droplets can be manipulated in a similar way as the pure fluid. Since we are also interested on the study of the complete evaporative behaviour under an external DC voltage applied, the aims pursued during this part were two-fold; on one hand understanding the manipulation and control of a nanofluid droplet interface, and on the other uncovering the mechanisms present during the complete evaporation of these fluids.

The electrowetting of different TiO_2-water nanofluid concentrations has been seized and an enhancement in the extent of spreading when compared to the pure fluid case, for a same voltage applied, is observed. Adsorption of nanoparticles triggered by voltage, has been proposed to account for the enhancement in spreading observed and a modified Yong-Lippmann equation where the surface tension solid-liquid is modified due to the addition of nanoparticles and voltage applied is presented. On the other hand, the complete evaporative behaviour of these fluids has been studied attending to both the macroscopic evaporative behaviour and the deposits found after the complete evaporation. More homogeneous deposits and the absence of stick-slip behaviour has been observed under an external voltage applied. Electrokinetic transport of the nanoparticles towards the electrode of opposite charge is reported as the main mechanism governing the motion of particles during evaporation, in contrast to the mechanisms reported under AC conditions.

The next chapter describes; the fluids studied and preparation method, electrowetting setup, procedure, and the different techniques, tools, and approaches, adopted during this experimental research. Furthermore, additional measurements and tools used for the further characterization of both fluids and substrates are included along.

Chapter 3: Experimental Techniques and Apparatus

The growing interest in the complete understanding of the interactions between solid surfaces and liquids (colloidal suspensions, ionic liquids, nanofluids) has led to the development of novel and more reliable experimental methods and techniques. Pendant drop, sessile drop and AFM are the techniques used during this research, to shed further light on the binary interactions particle-particle, particle-liquid, solid-particle, solid-liquid and liquid-gas throughout evaporation. In addition, electrowetting (EW) technique has been implemented to this experimental research to study these interactions under an external voltage applied.

With this aim in view, droplet shape has been analyzed at the macroscale and different evaporative behaviours [135] depending on the hydrophobicity of the substrate, nature of the fluid, addition of nanoparticles, nature of the particulate material or an external force applied, have been identified. The study of the different evaporative modes has helped to reveal some of the mechanisms present in the dynamics of the contact line during evaporation and to address the physics of evaporation further. Besides studying the evaporative behaviour under an external voltage applied, the electrowetting/dewetting, i.e. spreading/receding movement of the contact line under an applied voltage, has also been sized as change in contact angle versus voltage, V, for the pure fluid case and for different nanoparticle concentrations.

In order to fully characterize the fluids and nanofluids used during this experimental research, additional measurements using different techniques and apparatus have been also adopted and included in this chapter.

3.1 Experimental Techniques

3.1.1 Droplet Shape Evolution

DSA100 (droplet shape analyser) from Krüss (GmbH, Hamburgh, Germany) was the apparatus used to dispense droplets of controlled volume and to capture the droplet

profile evolution over time until the complete vanishing. DSA100 is equipped with: an adjustable sample table, a back light, a computer controlled dosing system and a CCD camera with a video-digitalized board capable of transferring a sequence of images (up to 25 fps) to the PC. On other hand, DSA1 v1.9 was the software used for the control of the dosing system, droplet deposition, and to capture and analyze the droplet profile based on sessile droplet technique. First, a previously cleaned substrate was placed on the adjustable sample table, and a 3 µl droplet was gently deposited on the chosen substrate using the DSA100 dosing system and syringe position. Second, the recording was started and up to 400 frames per droplet evaporated were acquired and analyzed. Last, contact angle, θ, base radius, R, and droplet height, h, were extracted over time, t, and plotted using Origin.

All experiments were carried out in a controlled atmosphere at 20 ºC and relativity humidity ca. 30%, unless stated otherwise. Figure 3.1 includes the setup used during this experimental research, besides a snapshot of DSA1 v1.9 software to illustrate the optimum contrast and sharpness required between droplet and surroundings. Base line and droplet fitting are included for comparison.

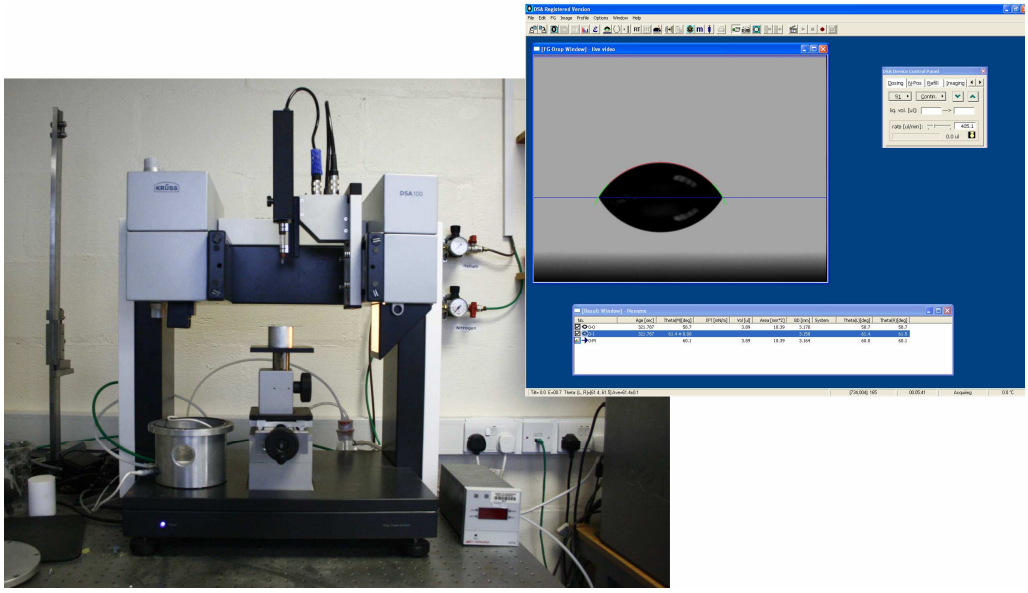

Figure 3. 1 – DSA100 from Krüss consists of: a moveable sample table, a back light, a CCD camera and dosing system and DSA1 v1.9 software snapshot.

Concerning the analysis of the droplet profile, DSA1 v1.9 software includes five different methods for the fitting of the droplet shape, although only Tangent Method 1 and Circle Fitting were the methods adopted for this analysis. Typically, Tangent Method 1 was chosen for the fitting on hydrophilic substrates whereas Circle Fitting was used for droplets on hydrophobic ones.

3.1.2 Electrowetting of Volatile Droplets

Aiming to uncover the interactions solid-particle, solid-liquid, particle-liquid and particle-particle under an external electric field applied, a self-made electrowetting (EW) setup was implemented to the DSA100. This setup consisted on a DC power supply (D100 1), a copper electrode (91 μm in diameter) and a substrate holder for the EWOD substrates described in Section 3.2.2.2. Figure 3. 2 includes the complete setup used during the experimental research carried out in Chapter 8:

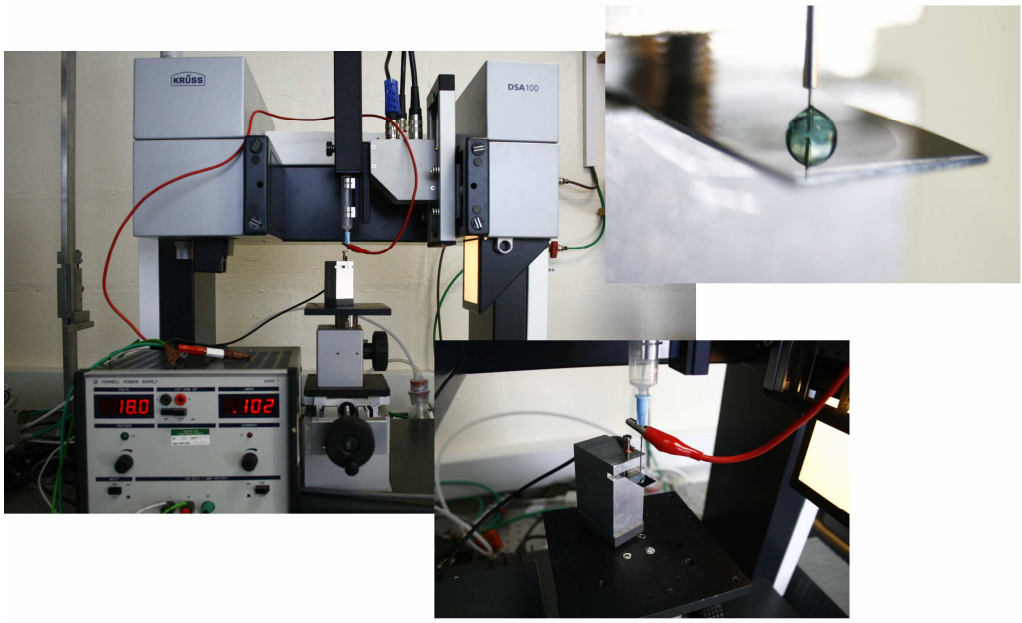

Figure 3. 2 – Electrowetting setup and DSA100. DC power supply, positive (red wire) and negative (black wire) electrodes, substrate holder and EWOD substrate are included.

The procedure followed was analogous to the one described in Section 3.1.1 although few intermediate steps were necessary before and after the deposition of the droplet. Firstly, EWOD substrate was fixed to the substrate holder using a screw, with the latter in turn connected to the positive electrode of the power supply. Right after the deposition of a droplet onto the EWOD substrate, the negative electrode was gently immersed into the droplet using the syringe position control. Video recording of the droplet profile was initiated and voltage was turned On using a manual switch. Finally, analysis of the droplet profile was carried out.

3.1.3 High Speed Camera

The dynamics of spreading/receding of the contact line under EW and non-EW conditions were also investigated. In order to capture the instantaneous movement of the droplet interface when an external voltage is switched On/Off repeatedly, a high speed camera (Mikrotron MC1310 GmbH, Germany) and the software MotionBLITZ® (Director version 3.2.0 from Mikrotron), were required for the acquisition of up to 200 frames per second. A backlight to achieve the optimum contrast for the processing of the images was also implemented. The same self-made electrowetting setup described in Section 3.1.2 was used. A sketch of the apparatus and a cross-sectional view of the EWOD substrate used during the research carried out in Chapter 7 can be seen in Figure 3. 3:

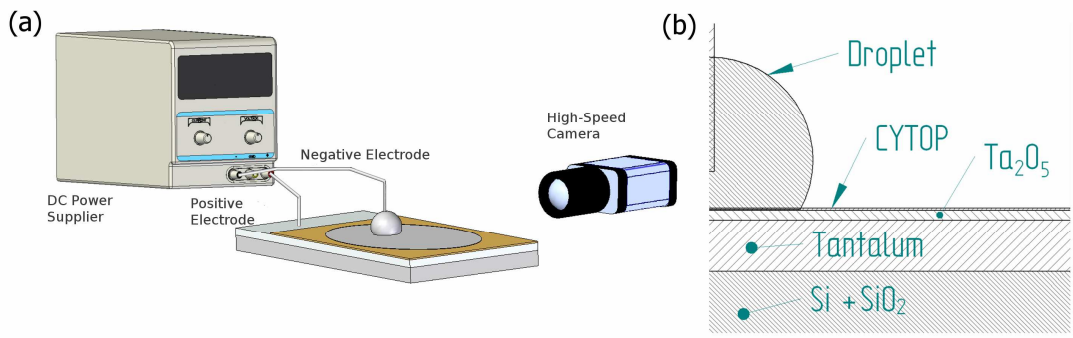

Figure 3. 3 – (a) 3D view of typical experimental EWOD setup used to capture the instantaneous movement of the contact line when switching voltage On/Off. EWOD substrate, high-speed camera, and positive and negative electrodes connected to the substrate are included. (b) Cross-sectional view of the EWOD substrate and droplet is included.

After the deposition of a droplet and the immersion of the negative electrode into this latter, up to 15 On/Off cycles were applied using a manual switch (DC step voltage test). Concentration, voltage, and thickness of the insulating layer were the variables studied. To analyze the quick electrowetting/dewetting movement of the contact line, images were captured using the software MotionBLITZ® and processed with ImageJ to create a video. This video was subsequently analyzed with DSA1 v1.9 software. Experiments were repeated up to three times for the same concentration, identical substrate and unvaried voltage. To exemplify the reproducibility and consistency of the electrowetting/dewetting movement of the contact line Figure 3. 4 is included:

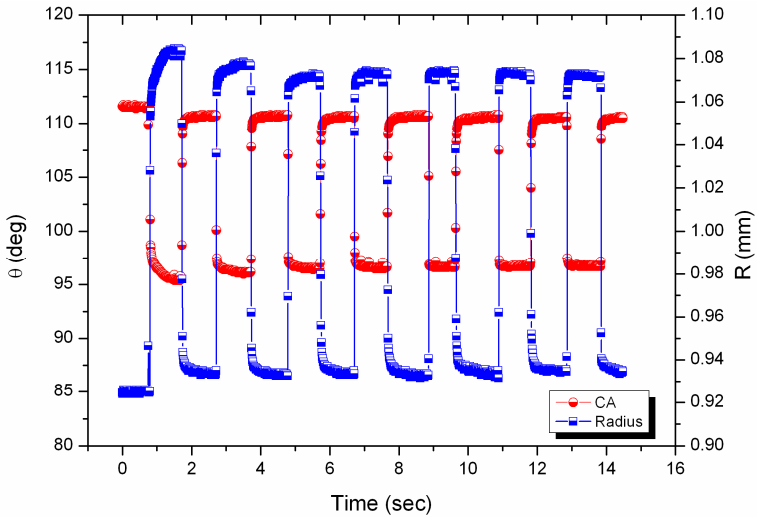

Figure 3. 4 – Contact angle and base radius versus time for deionized water at 30 volts during 7 cycles On/Off on $Cytop_{300}$.

3.1.4 Additional Measurements

To further characterize the fluids and substrates used during this experimental research, additional experimental techniques adopted and instruments and apparatus employed are included next.

3.1.4.1 Pendant Drop Technique

In order to rule out any change in surface tension liquid-gas, γ_{lg}, due to the addition of nanoparticles to a base fluid, for the low range of concentrations tested, additional pendant drop experiments were carried out. These measurements are based on a balance between interfacial forces keeping the droplet attached to the needle and gravitational ones pulling the droplet down.

FTA100 from First Ten Angstroms (Portsmouth, VA) was the equipment used for the measurements of the interfacial tensions liquid-gas for the different fluids tested

during this experimental research. Up to 3 different experiments were carried out in a controlled atmosphere at 15 ºC for each concentration and for the pure fluid case:

Table 3. 1 - Average surface tension liquid-gas and standard deviation for water and for the following TiO_2-water concentrations by weight: 0.001%, 0.01% and 0.1% at 15 ºC.

Concentration	**Water**	**0.001%**	**0.01%**	**0.1%**
γ_{lg} (mN/m)	73.7	73.2	73.6	73.5
Sandard Deviation	± 0.5	± 0.5	± 0.5	± 0.5

Table 3. 1 shows no appreciable variation on surface tension for the low range of concentrations tested.

3.1.4.2 Atomic Force Microscopy

Atomic Force Microscopy (AFM) technique was adopted to characterize some of the substrates used during the experimental research carried out in Chapter 4 and, to image the features of the deposits left after the complete evaporation of a nanofluid droplet included in Chapter 5. The motivation for using AFM to obtain information of substrates and deposits, was due to the great resolution down to the atomic scale in both horizontal and vertical planes offered by this novel technique. The equipment used was a Burker Multimode/Nanoscope IIa AFM (Bruker, Santa Barbara, CA), with 8 nm radius LTESP Bruker cantilevers with a nominal spring constant of 48 N/m and resonance frequency of 190 kHz under tapping mode (intermediate contact of the tip with the substrate) in air and at room temperature. Thereafter images were processed using SPIP™ (Image Metrology, Hørsholm, Denmark). AFM experiments were carried out by Alexandros Askounis current PhD student at the Institute for Materials and Processes at the University of Edinburgh.

3.1.4.3 Electrophoretic Mobility (EPM)

In order to explain the more homogeneous deposits found after the complete evaporation of a nanofluid droplet under DC voltage applied, additional electrophoretic mobility (μ_{ep} or EPM) measurements of the titanium dioxide (TiO_2) nanoparticles dispersed into water at different concentrations were carried out. These EPM measurements aim to experimentally seize the behaviour and interactions of charged particles/cells/bacteria/proteins in suspension, when subjected to an external uniform electric voltage. ZetaPALS or Zeta Potential Analyzer from Brookhaven Instrument Corporation (BIC) and the software ZetaPALS from the same manufacturer were the means used to obtain these μ_{ep}.

Approximately 1.5 millilitres of the nanofluid were placed in a cuvette, followed by the immersion of two parallel electrodes in this latter. Electrodes were connected to the equipment using a wire and both cuvette and electrodes were placed inside the ZetaPALS. Thereafter an AC (alternate current) electric field, E, between 6 and 9 V/cm, was applied to the suspension inducing the oscillating back and forth movement of the charged particles. This motion of the nanoparticles was tracked and measured by Phase Analysis Light Scattering (PALS) that offers greater sensitivities than the typical laser Doppler methods [136]. Subsequently ZetaPALS software calculates the zeta potential, ζ, of the particles in suspension using either Hückel or Smoluchowski limits from the experimentally measured mobilities. For each concentration a total of 20 different measurements were averaged. Standard deviation was also calculated and included in Table 3. 2:

Table 3. 2 – Electrophoretic mobility and zeta potential for 0.01%, 0.05% and 0.1% of TiO_2 nanoparticle concentration by weight in deionized water.

Concentration	0.01%	0.05%	0.1%
μ_{ep} ((μm/s)(V/cm)$^{-1}$)	-2.20 ± 0.07	-1.65 ± 0.11	-1.6 ± 0.15
ζ (mV)	-43.7 ± 1.6	-39.0 ± 2.5	-37.7 ± 3.6

3.2 Fluids and Substrates

3.2.1 Fluids

3.2.1.1 Pure Fluids

Deionized water was obtained from a Barnstead NANOpure® Diamond™ Analytical ultrapure water system with a conductivity of $18.2 \times 10^{-6}\ \Omega/cm$. On other hand, ethanol, as low surface tension fluid, was purchased from Sigma Aldrich.

3.2.1.2 Nanofluids

Nanofluids used in this experimental study were prepared following the two-steps method, where particles in the nanometre range are dispersed into a base fluid. Titanium dioxide (TiO_2) and aluminium oxide (Al_2O_3) nanoparticles with a typical particle size of <25 nm and <50 nm respectively were purchased from Sigma-Aldrich. Different concentrations by weight were prepared using a microbalance GR-202 with an accuracy of 0.00005 grams. Thereafter nanofluids were placed in an ultrasonic bath from Fisher Scientific (FB15047) for several hours until no agglomeration was observed. All nanofluids were ultrasonicated for a further hour prior to the deposition of a nanofluid droplet on a substrate. No salts, ions or surfactants were added to the system.

3.2.2 Substrates

3.2.2.1 Normal Substrates

In order to minimize contact angle hysteresis the following properties are required; ideal, flat, smooth, rigid solid without chemical heterogeneities or surface defects. Substrates were prepared at the Scottish Microelectronic Centre (SMC) as follows: approximately 1 μm polymer layer was deposited by spin coating over an oxidized silicon wafer. After spin coating, annealing was performed in a semiconductor industry standard furnace at 330 ºC filled with nitrogen to remove any contaminant. The polymers deposited were; Teflon and Cytop (perfluorinated polymer consisting of C-C, C-F, and C-O bonds) considered as hydrophobic, and C_4F_8 (octafluorocyclobutane) and parylene (poly(p-xylylene) polymer)) which show an intermediate behaviour.

On other hand, to be able to cover wide range of wettabilities, different hydrophilic substrates were also investigated: glass, bare silicon and glass cover slip (thickness of 0.1 mm from TAAB) henceforth referred as glass*.

To illustrate the degree of hydrophobicity, the equilibrium contact angle for both water and ethanol measured on the different substrates tested are given in Table 3. 3:

Table 3. 3 - Equilibrium contact angle, θ_0, measured right after the deposition of the drop on the substrate ($t = 0$) for both water and ethanol on different substrates.

Fluid/Substrate	**Glass**	**Silicon**	**Glass***	**Parylene**	**C_4F_8**	**Cytop**	**Teflon**
Water (º)	28	57	71	89	104	110	114
Ethanol (º)	-	-	10	10	26	41	45

For the sake of completeness, silicon and Teflon substrates have been further characterized by AFM technique and results are included in Figure 3. 5:

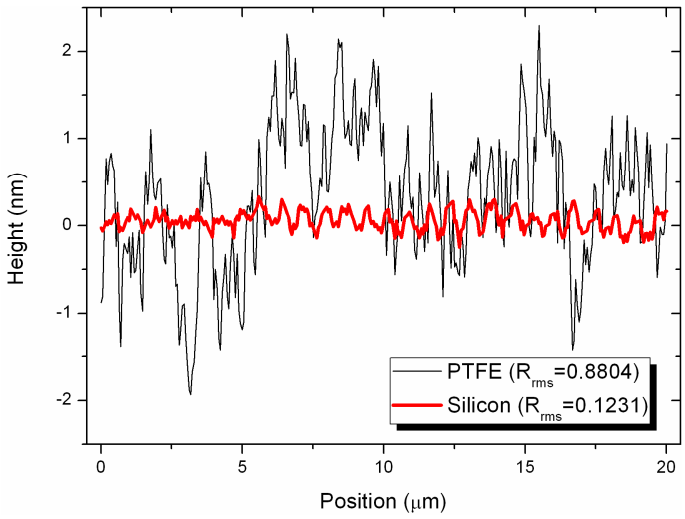

Figure 3. 5 - Height profiles of "smooth" silicon (thick solid red line) and "rough" Teflon (thin solid black line) showing the roughness in nanometres. Root mean square of both substrates has been calculated and included along.

Figure 3. 5 includes the height profiles of "smooth" silicon and "rough" Teflon obtained by atomic force microscopy. Roughness root mean square values are shown along. It is worth to mention that silicon roughness (hydrophilic substrate) is 10 times smaller than that of Teflon (hydrophobic one).

3.2.2.2 EWOD Substrates

EWOD substrates were created by introducing an insulating layer between the electrode and the conductive liquid solving the electrolysis problem and leading to a new range of low actuation voltage substrates [127]. The relevant properties required by these substrates are; high dielectric strength and high dielectric constant of the conductive electrode, besides a smooth and hydrophobic insulating layer coating the

electrode that minimizes hysteresis effects, offers good reversibility and about all avoids electrolysis.

The fabrication of these substrates was also carried out at the Scottish Microelectronic Centre (SMC) [129] and it can be summarized as follows. Firstly, a silicon (Si) wafer was exposed at 950 ºC water vapour in a high temperature furnace to create a 500 nm silicon oxide (SiO_2) layer. Secondly, 500 nm of tantalum (Ta) were sputtered onto the SiO_2 and thereafter the tantalum was anodized to grow a controlled layer of 95 nm of tantalum pentoxide (Ta_2O_5), acting as one of the dielectrics, i.e. positive electrode. The last part of the fabrication process involves the spin coating of the electrode using an amorphous fluoropolymer (aFP), in this case Cytop, to confer good reversibility and the hydrophobicity required. Three different aFP thicknesses were deposited onto the Ta_2O_5 to obtain a 22, 300 and 500 nm Cytop layer, henceforth referred as $Cytop_{22}$, $Cytop_{300}$ and $Cytop_{500}$.

3.2.3 Chamber

A cylindrical chamber made of stainless steel was used to conduct experiments in a controlled nitrogen atmosphere at different sub-atmospheric pressures, besides impeding the contamination from the surroundings. Two borosilicate small viewing windows allow for the recording of the droplet profile inside the chamber. A vacuum pump, nitrogen and helium supply, besides electric connections were also included in the construction features of the chamber.

3.2.4 Cleaning Procedure

Prior to the deposition of a droplet, substrates were cleaned by immersion of these latter in an ultrasonic bath from Fisher Scientific (FB15047) containing isopropanol and for ca. 15 minutes. Subsequently substrates were rinsed using abundant deionized water and thereafter dried with a stream of nitrogen to remove any dust or

contaminants. Syringes and needles were also washed vigorously with deionized water and dried with a nitrogen stream.

3.3 Summary

The various approaches and the combination of the different techniques and tools at the macro-, micro-, and nanoscale that have made possible to seize the different physic and chemical interactions during wetting, evaporation and electrowetting have been included here. In the following chapters, results, discussion and conclusions regarding the most important findings gathered during this experimental research are presented next.

Chapter 4: Effect of Substrate Hydrophobicity and Nanoparticle Concentration

Wetting and droplet evaporation are a phenomena present in everyday life and despites the intensive research carried out in this topic, many unknowns are still to be elucidated. It has already been reported that droplet evaporation rate is directly linked to the contact line dynamics; either evaporation at CCR (pinning) [9], at CCA (smooth receding) [10, 13] or a mixed evaporation behaviour can be found, mainly depending on the hydrophobicity of the substrate [11, 89]. In this part of the thesis we take a close look at the dynamics of the contact line during droplet evaporation for different fluids and on substrates varying in hydrophobicity, which can help to uncover the different mechanisms present during dry-out.

During evaporation, there is a competition between pinning forces preventing the movement of the contact line in one hand and depinning forces arising from the loss of mass modifying the droplet shape equilibrium on the other. A simple but effective theoretical approach based on an unbalanced Young force is adopted to explain the minimum force for the contact line to depin on substrates varying in hydrophobicity [1]. The second part of the chapter involves the addition of nanoparticles to a base fluid and the study of both effect of concentration and substrate hydrophobicity during the evaporation of these novel fluid when compared to the pure fluid case

4.1 Evaporation of Pure Fluids on Different Substrates

Results concerning the evaporative behaviour of pure fluids on very smooth substrates ranging from hydrophilic to hydrophobic, i.e. from wetting to non-wetting substrates are presented next. Substrates and fluids as well as the experimental procedure followed were described in the previous chapter.

4.1.1 Water

Figure 4. 1 shows the experimental behaviour of droplet profile portrayed as contact radius, R, and contact angle, θ, versus time, t, [135] for deionized water on substrates varying in hydrophobicity:

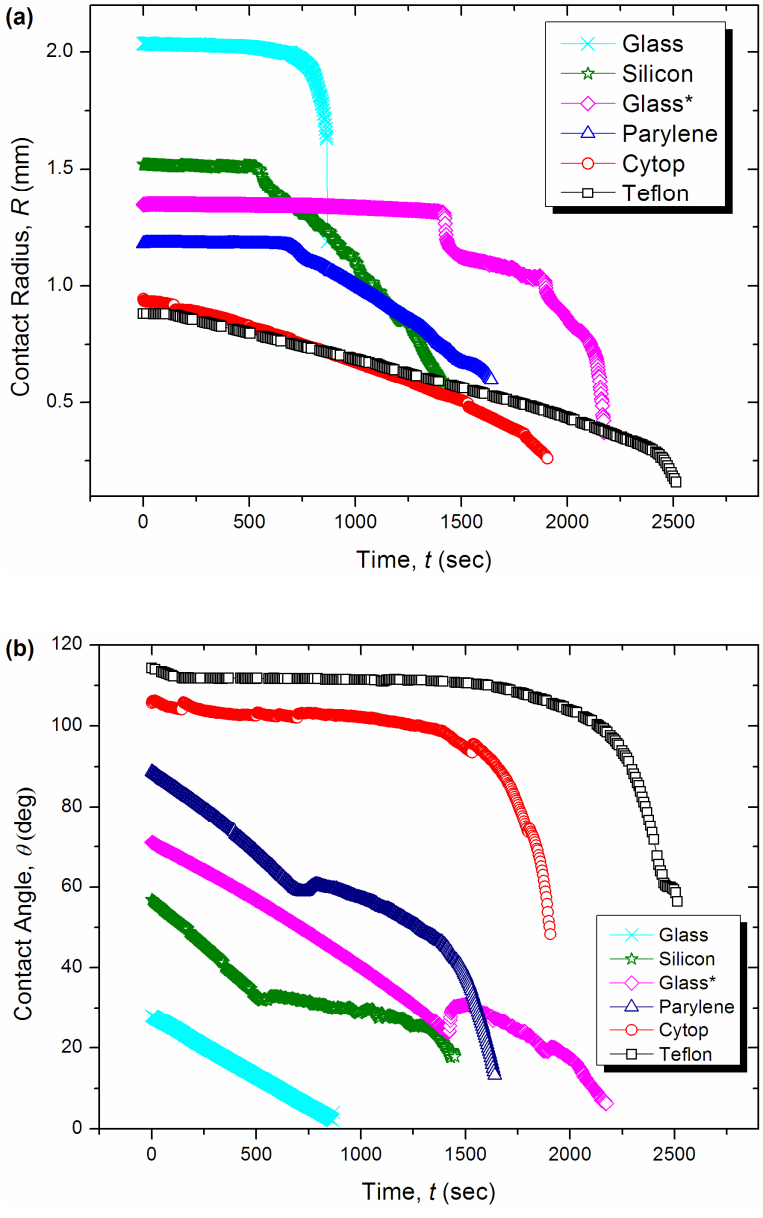

Figure 4. 1 – (a) Evolution of the contact radius, R (mm), and (b) evolution of the contact angle, θ (deg), for water on substrates ranging from the most hydrophilic to the most hydrophobic.

From the experimental results presented in Figure 4. 1, two different modes of evaporation can be identified for water droplets depending on the hydrophobicity of the substrate. On hydrophobic substrates, i.e. Cytop and Teflon, base radius decreases monotonically during most of the evaporation with a sudden decrease towards the end as shown in Figure 4. 1 (a). On the other hand, on hydrophilic substrates an initial pinning of the contact line, at least during the first 40% of the droplet lifetime, is reported. Thereafter the pinning stage, either a continuous or an interrupted receding of the base radius until the complete dry-out is observed. On glass, there is no depinning of the contact line during most of the droplet lifetime.

Looking at the contact angle, Figure 4. 1 (b), a plateau behaviour at least during 80% of the evaporation followed by a sharp decrease at the very end is reported on hydrophobic substrates. In contrast, on hydrophilic ones, the initial pinning of the contact line leads to a steady decrease in the contact angle until the contact line depins.

Regarding the evaporative behaviour, on the most hydrophilic of the substrates, i.e. on glass, since there is no depinning of the contact line, a constant rate of evaporation until the complete vanishing of the droplet is reported [11]. In the intermediate case where there is pinning (first) and thereafter depinning of the contact line, rate of evaporation deviates from linearity decreasing in time due to a continuous reduction on the contact radius with time.. On the other hand, on hydrophobic substrates, the continuous receding of the contact line points out to a nonlinear evolution of either mass or volume in time [88, 137]. It is worth noting that a smooth receding of the contact line is reported for the same fluid on Teflon even though this latter is almost 10 times rougher than the Silicon used during this experimental research (see Figure 3. 5). Pinning is *not* uniquely dependent on substrate roughness.

4.1.2 Ethanol

To support the findings observed for pure water, experiments using pure ethanol were carried out on 4 different substrates. The limitation on the number of substrates

is due to the low surface tension of this fluid spreading in medium- and high-energy substrates. Evolution of the contact radius, R, and contact angle, θ, versus time, t, on: glass*, C_4F_8, Cytop and Teflon are presented in Figure 4. 2:

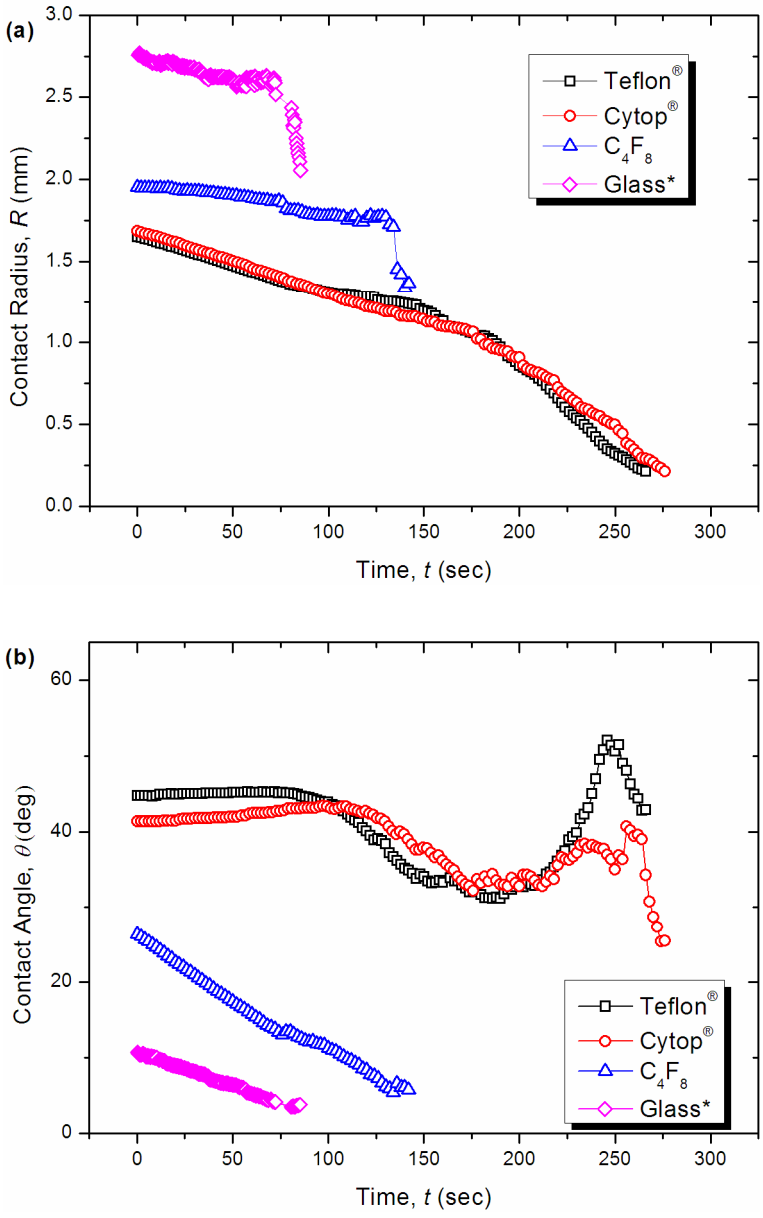

Figure 4. 2 – (a) Evolution of the contact radius, R (mm), and (b) evolution of the contact angle, θ (deg), vs. time, t (seconds), on different substrates.

Smilingly to the evaporative behaviour reported for pure water (Section 4.1.1), the evaporation of ethanol also presents two different evaporative behaviours depending on the hydrophobicity of the substrate, Figure 4. 2. On hydrophobic substrates, i.e. Teflon and Cytop, there is a continuous receding of the contact line, almost steady, at constant contact angle during evaporation, followed by a slight decrease and then increase of the contact angle towards the end of the evaporative process. This latter is congruent with the findings reported for pure water on ideal surfaces [138]. However, on the other two substrates: glass* and C_4F_8, there is a slight drift of the contact line whereas the contact angle decreases linearly. The slight drift of the contact line during most of the droplet lifetime leads to a fairly constant evaporation rate [89].

4.2 Evaporation of TiO_2-water based Nanofluids

It has been widely accepted that the addition of nanoparticles to a base fluid modifies the properties of this latter. Enhancement in heat transfer, better conductivity [46], besides different evaporative behaviour when compared to the pure fluid are some of the features reported in the last decade where nanofluids excel [139]. One of the most important features of these colloidal suspensions is the difference in deposits and patterns left during and after the drying of a droplet. Typically during evaporation particles tend to accumulate at the vicinity of the contact line, causing pinning, thus modifying the evaporative behaviour when compared to the base fluid [102].

In what follows the effect of both nanoparticle concentration and substrate hydrophobicity on the evaporative behaviour is tackled. Contact radius and contact angle are represented versus time for 0.0005, 0.001, 0.005 and 0.01% TiO_2-water nanofluids on silicon as shown in Figure 4. 3.

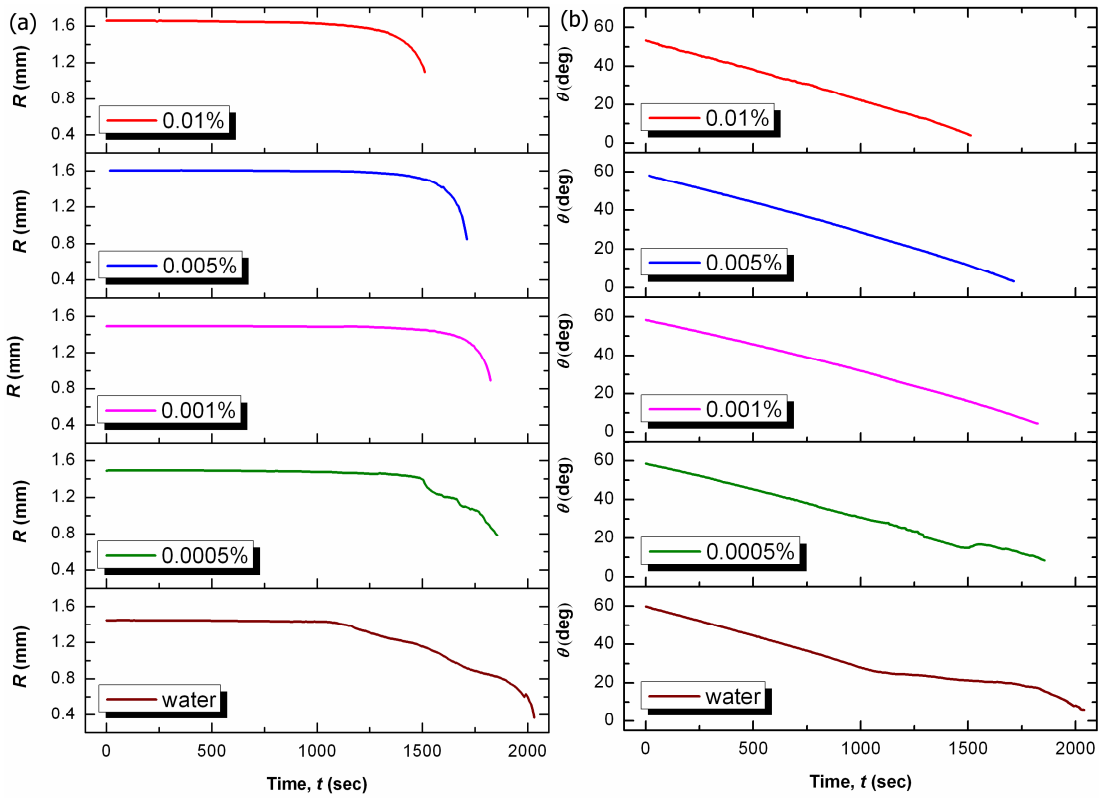

Figure 4. 3 – (a) Evolution of contact radius, R (mm), and (b) contact angle, θ (deg), versus time, t (s), for 0.0005, 0.001, 0.005, and 0.01% of TiO_2-water concentration by weight besides the pure fluid case on silicon ($\theta_0 \approx 60°$).

Looking at Figure 4. 3, a longer pinning of the contact line when adding small quantities of nanoparticles to the base fluid is observed. On hydrophilic substrates, the initial pinning of the contact line, reported in Section 4.1 favours the accumulation of particles at the triple contact line, thus the complete pinning of this latter observed for concentrations equal or greater than 0.001%. Since evaporation takes place mainly at the triple contact line, during the pinning stage, nanoparticles deposit at the edge of the contact line acting as defects or pillars hindering the receding movement of this latter, as it will be addressed in depth in the Chapter 5. When decreasing nanoparticle concentration down to 0.0005%, the receding of the contact line is observed, after 70% of the droplet lifetime, meaning that the amount of nanoparticles present is not high enough to ensure the complete pinning of the triple contact line during the dry-out on hydrophilic silicon substrates.

On the other hand, on hydrophobic substrates, i.e. Cytop and Teflon, a completely different evaporative behaviour to that reported on silicon was observed for all the concentrations tested. Figure 4. 4 and Figure 4. 5 show the evaporative behaviour for 0.1, 0.05, 0.025, 0.01 and 0.001% by weight, besides the pure fluid case on Cytop and Teflon respectively.

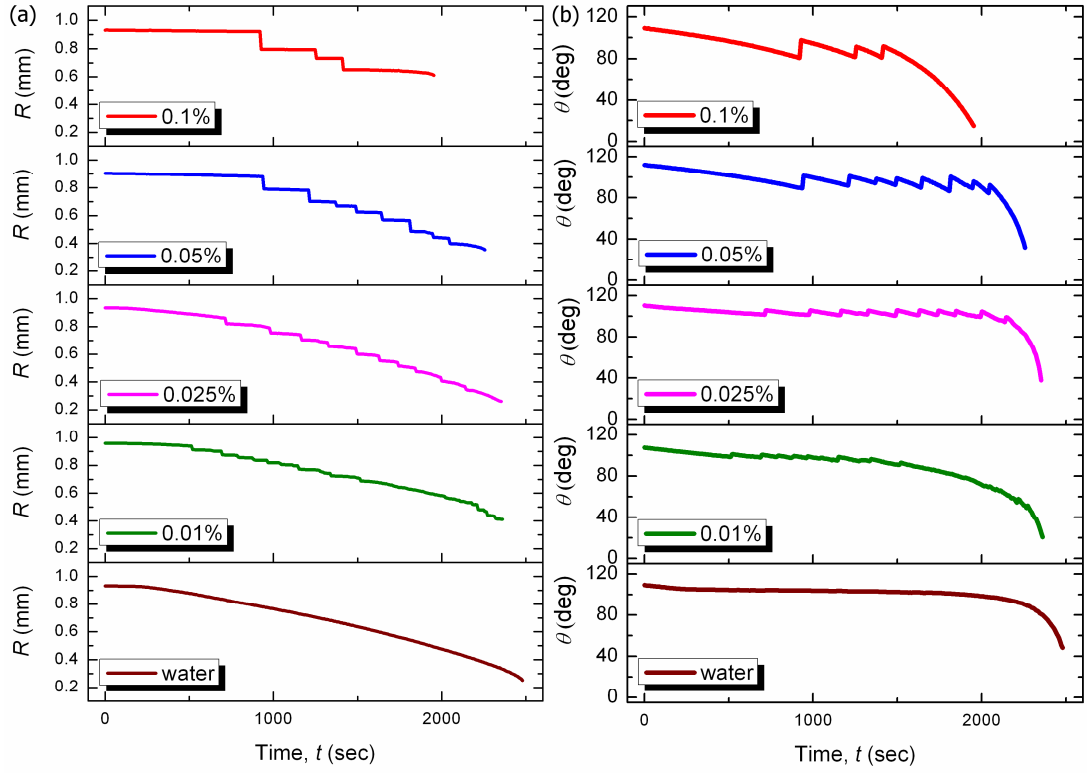

Figure 4. 4 – (a) Evolution of contact radius, R (mm), and (b) contact angle, θ (deg), versus time, t (s), for 0.01, 0.025, 0.05, and 0.1% of TiO_2-water concentration by weight besides the pure fluid case on Cytop ($\theta_0 \approx 110°$).

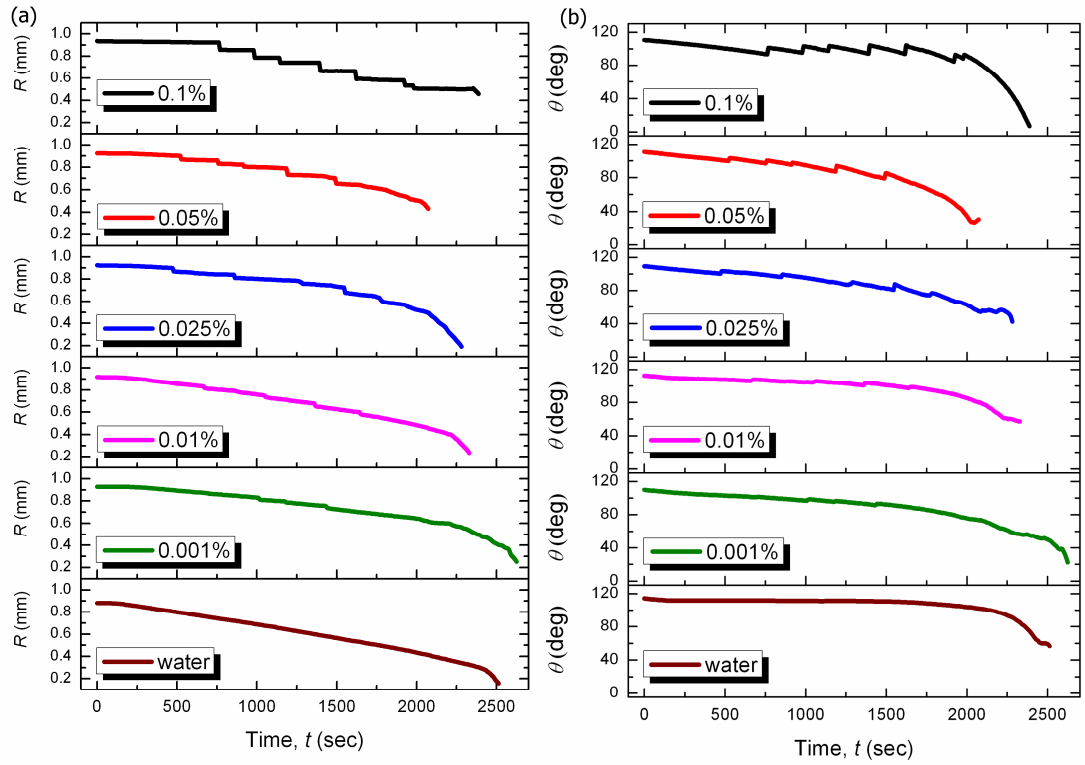

Figure 4. 5 – (a) Evolution of contact radius, R (mm), and (b) contact angle, θ (deg), versus time, t (s), for 0.01, 0.025, 0.05, and 0.1% of TiO_2-water concentration by weight besides the pure fluid case on Teflon ($\theta_0 \approx 115°$).

From both Figure 4. 4 and Figure 4. 5, differences in the evaporative behaviour for TiO_2 –water nanofluids vanishing on hydrophobic substrates are evident when compared to the base fluid. The addition of nanoparticles induces a noticeable "stick-slip" behaviour, where jumps of the contact line and changes in contact angle, accordingly, are observed for the range of concentrations tested. This is in contrast with the smooth receding of the contact line observed for deionized water.

During evaporation, due to capillary flows, nanoparticles suspended in the droplet accumulate at the triple contact line hindering the receding movement of the latter "stick" and contact angle decreases to account for the fluid evaporated. Thereafter the "slip" or jump of the contact line, and the consequent change in contact angle, is noticed. This behaviour is continued until the complete vanishing of a droplet containing TiO_2 nanoparticles.

"Stick-slip" behaviour was already reported in literature for the system TiO_2-ethanol although the effect of nanoparticle concentration was not taken into account [106]. Looking closely at Figure 4. 4 and Figure 4. 5, regular steps and terraces of the base radius together with discrete jumps of the contact angle are found to be more pronounced with increasing concentration as it was theoretically predicted [140]. The transition from the evaporative behaviour of a water droplet on an ideal, smooth and hydrophobic surface at constant contact angle to the gradual increase in the magnitude of the "stick-slip" steps when increasing concentration is certainly noticeable.

Figure 4. 6 and Figure 4. 7 show a comparison between the different distance jumped by the contact line, δR, and the associated changes in contact angle, $\delta\theta$, for the different TiO_2-water nanofluid concentrations on Teflon. The results presented were consistent for five independent observation carried out for each of the concentrations.

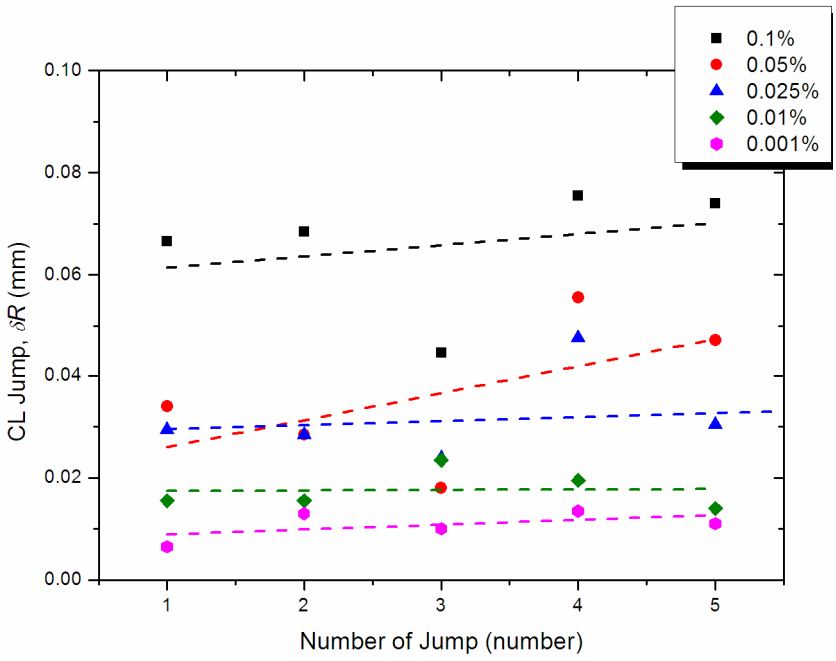

Figure 4. 6 – Magnitudes of the jumps, δR (mm), of the contact line for the different TiO_2-water concentrations: 0.1%, 0.05%, 0.025, 0.01 and 0.001% on Teflon. Linear trends for each concentration are also included.

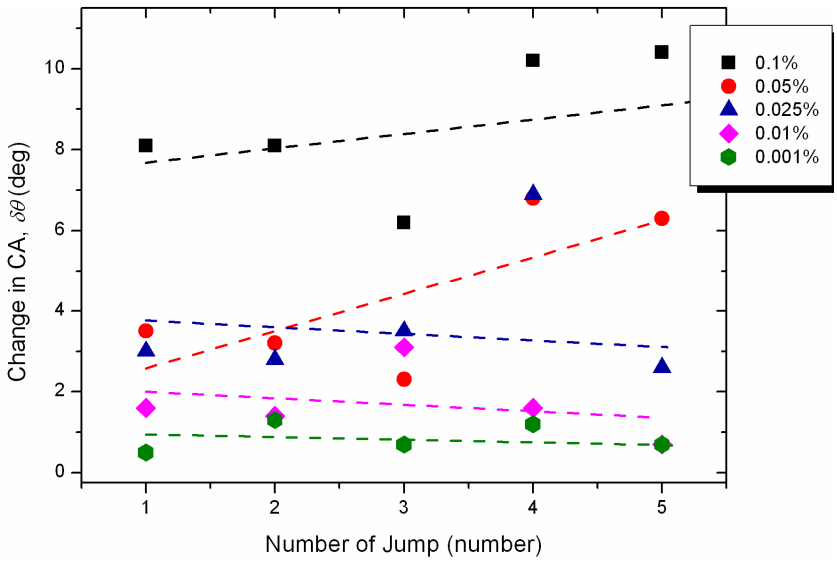

Figure 4. 7 - Change in contact angle, $\delta\theta$ (deg) for the different TiO_2-water concentrations: 0.1%, 0.05%, 0.025%, 0.01% and 0.001% on Teflon. Linear trends for each concentration are also included.

It is clearer now that "stick-slip" performance absolutely depends on TiO_2 nanoparticle concentration being more marked when increasing concentration. At the present, no theoretical explanation to account for the magnitudes of these steps is available. Shanahan suggested that δR must scale with $R^{1/2}$ for a constant energy barrier [3, 141], although in the present case the energy barrier may evolve since there is a locally increase in nanoparticle concentration due to the evaporation of the fluid. Clearly, both the amount of nanoparticles and the hydrophobicity of the surface play an important role in the dynamics of the contact line. The larger the concentration of particles the greater the accumulation of these latter at the edge due to evaporation and therefore larger jumps of the contact line are observed [102].

The behaviour is consistent since it was found that the build-up of TiO_2 nanoparticles at the contact line is proportional to nanoparticle concentration [97] . Nanoparticles present at the triple contact line act as irregularities or defects and the more nanoparticles the more marked is the pinning of the contact line. As evaporation takes place, Figure 4. 4 and Figure 4. 5, contact angle evolves driving the droplet out of its thermodynamic equilibrium until the internal free energy of the droplet is high

enough to overcome the energy barrier exerted by the nanoparticles and the jump ensues, as it will be addressed in the next subsection.

4.3 Evaporation of Al_2O_3-water based Nanofluids

For comparison, the evaporative behaviour of Al_2O_3-water nanofluids was also studied on Cytop substrates. In the case of Al_2O_3 nanoparticles, the concentration required to attain the complete pinning of the contact line is at least ten fold smaller than for TiO_2 nanoparticles. Thus to observe similar "stick-slip" behaviour as presented in both Figure 4. 4 and Figure 4. 5, smaller concentrations of these nanofluids were required: 0.01%, 0.005%, 0.001% by weight. Figure 4. 8, includes the evolution of both contact angle and contact radius versus time for different Al_2O_3-water nanofluid concentrations and for the pure fluid.

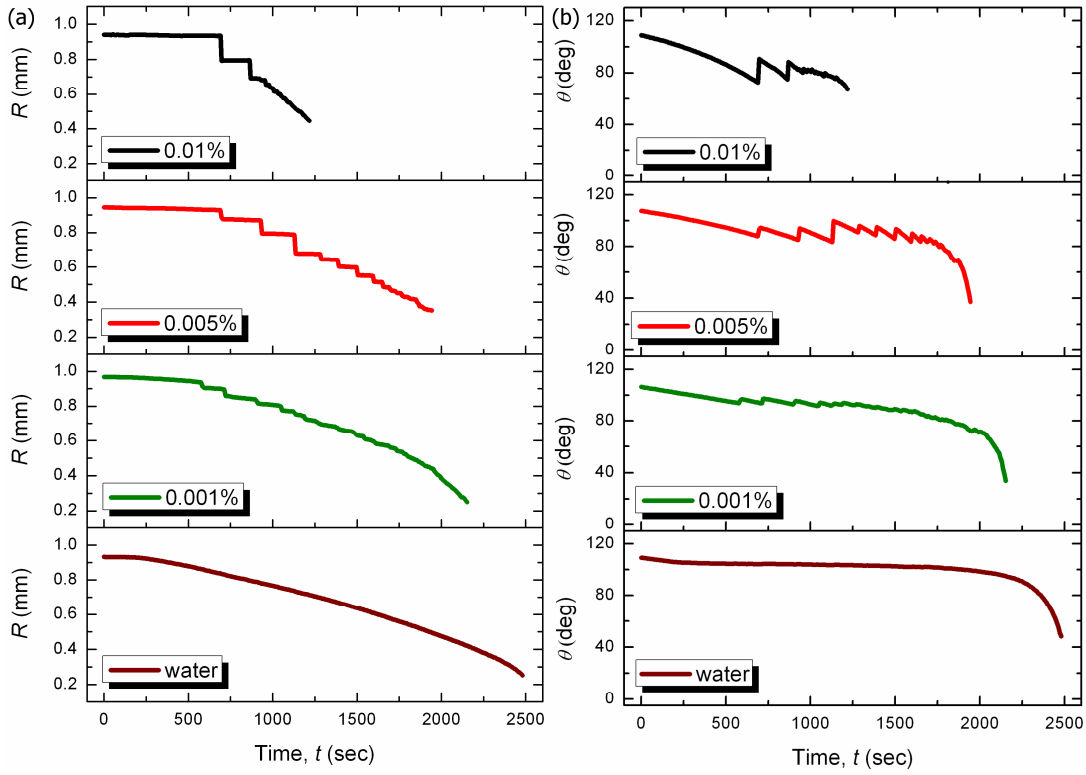

Figure 4. 8 - (a) Evolution of contact radius, R (mm), and (b) contact angle, θ (deg), versus time, t (s), for 0.001, 0.005, and 0.01% of Al_2O_3-water concentration by weight besides the pure fluid case on Cytop ($\theta_0 \approx 110°$).

"Stick-slip" behaviour at lower concentrations is reported for Al_2O_3-water nanofluids when compared to TiO_2-water nanofluids. An longer pinning of the contact line is observed for the highest of the concentrations and, as previously pointed out; shorter jumps of the contact radius and smaller changes in contact angle are noticed when decreasing nanofluid concentration.

4.4 Interpretation and Discussion

The mechanisms underpinning the behaviour of the triple contact line during evaporation for different fluids and on substrates varying in hydrophobicity using the results gathered in the previous section are addressed next.

4.4.1 Pure Fluids

To elucidate the effect of substrate hydrophobicity on the pinning-depinning of the contact line, a force balance or an energy minimization approach is proposed. Since contact line remains pinned, at least during the first period of the evaporation, it is the change in contact angle, to account for the loss of volume, what drives the droplet out of its thermodynamic equilibrium. Thus, we try to address this force looking closely at the changes in contact angle.

Figure 4. 9 shows the region at the vicinity of the triple contact line both at equilibrium, θ_0, and after some evaporation, $(\theta_0 - \delta\theta)$, at constant base radius:

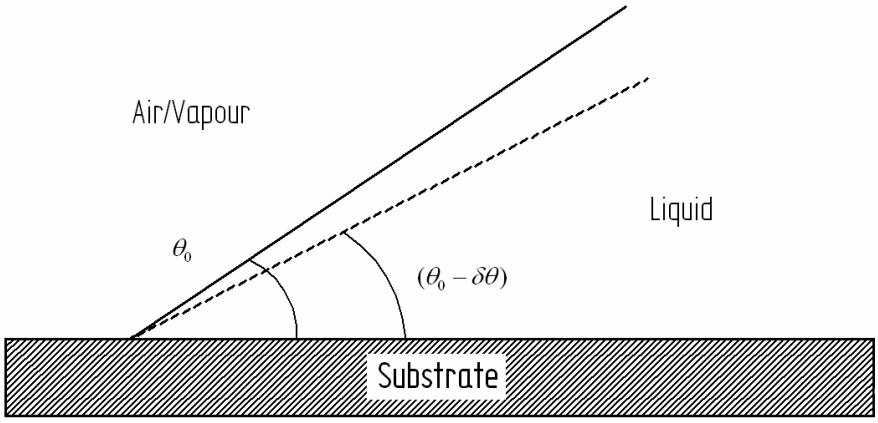

Figure 4. 9 – Schematic representation at the vicinity of the triple contact line region with the liquid interface at the equilibrium contact angle, θ_0, and at a slightly smaller angle, $(\theta_0 - \delta\theta)$.

Right after the deposition of a droplet on a substrate, at equilibrium, there is a null force at the triple contact line given by Young's equation (Equation 2.1) and expressed as Equation 4.1:

$$\delta\vec{F}_{t=0} = \gamma_{sl} - \gamma_{sg} + \gamma_{\mathrm{lg}} \cos\theta_0 \sim 0 \qquad (4.1).$$

After the deposition of a droplet, contact angle decreases following evaporation and a net force balance at the triple contact line can be carried out. At this point, a horizontal force towards the centre of the droplet can be quantified as a force per length, $\delta\vec{F}$; and using $\gamma_{sl} - \gamma_{sg} \sim \gamma_{\mathrm{lg}} \cos\theta_0$, Equation 4.2 can be demonstrated:

$$\delta\vec{F} = \gamma_{\mathrm{lg}} \cos(\theta_0 - \delta\theta) - \gamma_{\mathrm{lg}} \cos\theta_0 \approx \gamma_{\mathrm{lg}} \sin\theta_0 \delta\theta \qquad (4.2).$$

Opposing to the force favouring the movement of the contact line, there is an intrinsic energy barrier, U, that hinders the receding movement of this latter as reported elsewhere [89, 106]. Taking a differential of mentioned energy barrier, $\partial U/\partial r$, the force opposing the depinning of the contact line can be written as:

$$\frac{\partial U}{\partial r} = \delta\vec{F} = \gamma_{\mathrm{lg}} \sin\theta_0 \delta\theta \qquad (4.3).$$

The depinning of the contact line will occur *only* when the Young unbalanced force at the contact line will be large enough to overcome the intrinsic energy barrier preventing the receding of the triple line. This rigorously will happen when $\partial U/\partial r < \delta\vec{F}$, i.e. for large changes in contact angle arising from high initial contact angles. Thus, the more hydrophobic the substrate the easier for the contact line to depin like in the case of Cytop and Teflon, where θ_0 is high enough so the required $\delta\theta$ becomes very small for a given $\partial U/\partial r$. Although a continuous receding motion of the contact line until the complete vanishing of the droplet for both water and ethanol is observed at the macroscale, microscopic jumps might be noticed [141]. On the contrary, for small θ_0, i.e. water on glass and ethanol on both C_4F_8 and glass*, the unbalanced Young's force appears to be insufficient to allow for the depinning of the contact line. The intermediate case is observed for water on silicon, glass* and

parylene with a $\theta_0 > 1$ rad where an initial pinning of the contact line is reported followed by the depinning of this latter. Depinning force is definitely function of the θ_0 [141]. An analysis of the unbalance forces at the triple contact line before the depinning of this latter on hydrophilic substrates using Equation 4.3 is presented in Figure 4. 10:

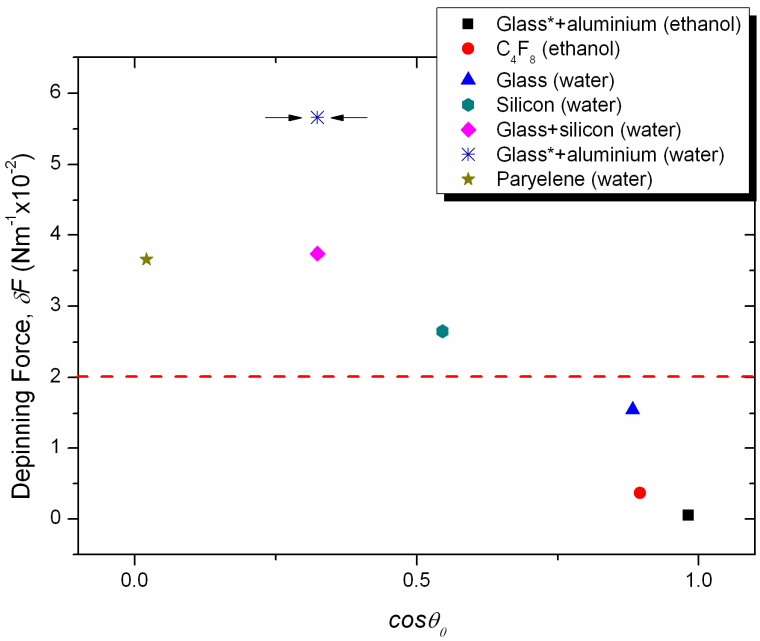

Figure 4. 10 - The unbalance force right before the depinning of the contact line, $\delta\vec{F}$, calculated using Equation 4.3 on the following systems: glass*+aluminium-ethanol, C_4F_8-ethanol, glass-water, silicon-water, glass*+silicon-water, glass*+aluminium-water and parylene-water versus $\cos\theta_0$. Dotted line represents the minimum energy required for the depinning to ensue.

After the quantitative analysis presented in Figure 4. 10, a threshold value for the depinning force to surmount the energy barrier may be established as $\delta\vec{F} \sim 0.02$ N/m. Depinning force is favoured by high equilibrium contact angles, the greater the equilibrium contact angle the smaller the change in contact angle required for the contact line to recede. It is worth noting the differences in the depinning force for a similar θ_0 when the material inserted underneath a glass cover slip (glass*) changes,

i.e. glass*+silicon and glass*+aluminium, as shown in Figure 4. 10 and discussed more in detail by Orejon et al. [58].

4.4.2 TiO_2-water Nanofluid

The study of the dynamics of the contact line under the addition of different quantities of TiO_2 nanoparticles to a base fluid on silicon, Cytop and Teflon is included below.

On hydrophilic silicon substrate, as included in Figure 4. 3, the small addition of nanoparticles to water, i.e. 0.001% by weight, induces the complete pinning of the contact line during the dry-out. The combination of an increased energy barrier at the triple contact line due to nanoparticle addition besides the low initial contact angle reported on this substrate, makes $\partial U/\partial r$ high enough for no depinning of the contact line to occur. It is of great importance to mention that decreasing the concentration of nanoparticles below 0.001%, the number of nanoparticles is not high enough to surpass the energy threshold required for the contact line to be completely pinned throughout evaporation. The effect of nanoparticle concentration on the pinning-depinning of the contact line on hydrophobic substrates is also addressed.

On the completely opposite case, on hydrophobic substrates, Cytop and Teflon (Figure 4. 4 and Figure 4. 5), several pinning-depinning cycles, known as “stick-slip” behaviour of the contact line are noticed for concentrations equal or above 0.001%. “Stick-slip” behaviour is more pronounced when increasing concentration as greater amount of nanoparticles reach the vicinity of the contact line increasing the local energy barrier further. An extra term can be added to Equation 4.3 to account for the effect of nanoparticles: $\partial\vec{F} \sim \partial\vec{G} > \partial U/\partial r)_{Substrate} + \partial U/\partial r)_{Nanoparticles}$. Then, it is clearer then that the change in contact angle required for the jump of the contact line to ensue will be larger with increasing concentration, i.e. the excess of droplet free energy must be high enough to overcome the energy barrier exerted by the nanoparticles and the substrate.

Based on the evaporative behaviour of these nanofluids, an approximation of the internal free energy required by these droplets for the jump to ensue on Teflon can be estimated from the evolution of both base radius and contact angle presented in Figure 4. 5 (a) and Figure 4. 5 (b). Two equivalent expressions of the energy barrier per unit length of the triple contact line, $\delta\vec{G}$, have been previously derived, Equation 4.5 and Equation 4.6, to evaluate the free energy gained by the droplet before the jump. This energy arises from the unbalanced Young's force, i.e. free energy is proportional to the energy barrier U [141, 142]:

$$\delta\vec{G} = \frac{\gamma_{lg} \sin^2 \theta_0 (2 + \cos\theta_0)(\delta R)^2}{2R} \quad (4.5),$$

$$\delta\vec{G} = \frac{\gamma_{lg} R(\delta\theta)^2}{2(2 + \cos\theta_0)} \quad (4.6).$$

The choice of using either Equation 4.5 or Equation 4.6 depends on the data available from the characterization of the droplet profile. Since both jumps of the base radius and changes in contact angle for the different nanoparticle concentrations are given in Figure 4. 6 and Figure 4. 7 respectively, the intrinsic energy barriers at the triple line can be calculated using either equation. To rule out any change in the interfacial tension liquid-gas due to the addition of nanoparticles, pendant drop experiments were carried out as explained during Chapter 3. A constant value of the surface tension liquid-gas for the low range of concentrations prepared was found at ca. 72.8 mN/m (Table 3. 1). Typical contact radius for a 3 µl water droplet on Teflon, $\theta_0 \sim 114°$, is ca. 0.9 mm before the first slip of the contact line. Then substituting these data and the values obtained from Figure 4. 6 and Figure 4. 7, an estimation of the energy barrier versus concentration is presented in Figure 4. 11:

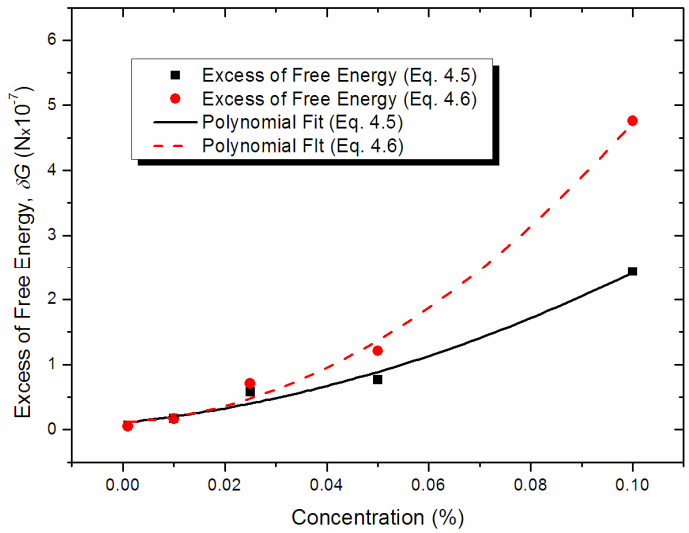

Figure 4. 11 – Excess of free energy, $\delta\vec{G}$, for the first jump ($N \cdot 10^{-7}$) calculated for the different TiO_2-water nanofluid concentrations tested on Teflon using Equation 4.5 (squares) and Equation 4.6 (circles). Polynomial fits are included to illustrate trends.

Figure 4. 11 allows for an easier comparison of the excess of free energy versus concentration before a jump. It was found that the internal free energy required for the droplet to move towards a more favourable thermodynamic position is an increasing function of nanoparticle concentration. Larger quantities of nanoparticles building up at the contact line hinder further the receding movement of this latter [97]. As mentioned previousl, greater changes in contact angle are necessary for the jump of the contact line to ensue when increasing concentration, as well as greater jumps of the contact line are observed for higher concentrations. Deposits act as heterogeneities or defects on the substrate being greater when increasing concentration (Chapter 5).

4.4.3 Al_2O_3-water Nanofluid

The results presented in Figure 4. 8 for different Al_2O_3-water nanofluid concentrations on Cytop supports further, the “stick-slip” behaviour reported for the evaporation of certain colloidal suspensions. Furthermore, the magnitude of contact

line jumps and changes in contact angle are proportional to the amount of nanoparticles present. The higher the concentration the greater the jumps observed, which is consistent with the discussion presented for TiO_2-water nanofluids. When comparing Figure 4. 4 and Figure 4. 8, the amount of Al_2O_3 nanoparticles required to attain similar "stick-slip" behaviour of the contact line to that reported for TiO_2– water is at least one order of magnitude smaller. Even if the concentration of Al_2O_3 nanoparticles is ten-fold compared to that of TiO_2, energy barriers in the same order of magnitude are reported. The next figure includes the excess of free energy presented in Figure 4. 11 for TiO_2-water nanofluids besides the excess of free energy calculated using both Equation 4.5 and Equation 4.6 for Al_2O_3-water nanofluids at different concentrations.

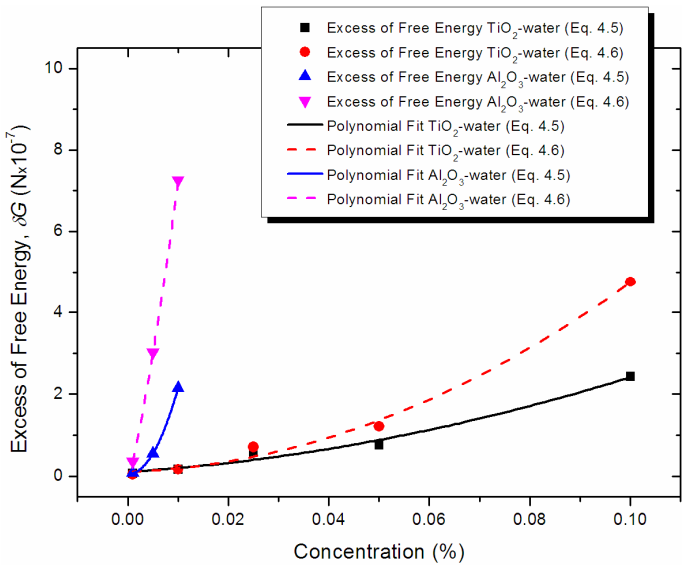

Figure 4. 12 - Excess of free energy, $\delta\vec{G}$, for the first jump ($N \cdot 10^{-7}$) calculated for the different Al_2O_3-water nanofluid concentrations on Cytop and for the different TiO_2-water nanofluid concentrations on Teflon using Equation 4.5 and Equation 4.6. Polynomial fits are also included.

From Figure 4. 12 it is obvious that the addition of Al_2O_3 nanoparticles to deionized water points out towards stronger interactions between Al_2O_3 nanoparticles and the substrate at the triple contact line than on the case of TiO_2-water nanofluids.

4.5 Summary

The dynamics of the triple contact line of volatile droplets for pure fluids (water and ethanol) and for TiO_2-water nanofluid at different concentrations has been studied on substrates varying from hydrophilic to hydrophobic.

In the case of pure fluids, a monotonic continuous receding movement of the contact line was observed on hydrophobic substrates whereas initial pinning of the contact line at least during 40% of the droplet lifetime was reported on hydrophilic ones. A force balance at the triple contact line has been proposed to explain the forces present during the depinning of the contact line favoured on hydrophobic substrates.

Experimental results of TiO_2-water nanofluids on both hydrophilic and hydrophobic substrates showed different evaporative behaviours when compared to the base fluid. Furthermore, a clearer dependence on the evaporative behaviour, "stick-slip" behaviour, with concentration was reported. Using the droplet profile and an unbalance Young equation, droplet internal free energy was calculated and found to be proportional to nanoparticle concentration. Jumps of the contact line and changes in contact angle are greater when increasing concentration. The latter has also been proven for the case of Al_2O_3-water nanofluids, although in this case similar energy barriers were observed for lower concentrations, when compared to TiO_2-water nanofluids, presumably due to stronger interactions of the Al_2O_3 nanoparticles with the substrate.

Since the macroscopic "stick-slip" behaviour observed on hydrophobic substrates is linked to the eccentric rings observed following evaporation; in what follows, an analysis into the detail of the deposits using atomic force microscopy has been carried out and a deposition theory is presented next.

Chapter 5: Structuring of Nanoparticles during *Free* Evaporation

The evaporative behaviour of colloidal suspensions and more specifically nanofluids, has been under intensive research in the past decades. Understanding *free* evaporation of these novel suspensions: internal flows, evaporative mode, effect of substrate hydrophobicity, besides the interactions solid-liquid, solid-particle or particle-particle, can help to shed light on the mechanisms that control the deposition of nanoparticles during the complete dry-out of a nanofluid droplet. This latter becomes of great importance for patterning or particle deposition amongst others. Typically, TiO_2-ethanol nanofluid droplets evaporate following "stick-slip" behaviour where jumps of the triple contact line (TCL) and changes in contact angle are associated with a set of eccentric rings reported after the complete evaporation [106]. Since most of the research carried out in this topic has focused its efforts on the study of the evaporative behaviour of colloidal suspensions at the macroscale, in this chapter information of the fine structuring of the deposits at the nanoscale has been obtained by atomic force microscope (AFM). The profile of the deposits is then coupled with the analysis of the evaporative behaviour at the macroscale and a deposition theory has been developed.

5.1 Evaporative Behaviour

In order to understand the deposits formed during the evaporation of a nanofluid droplet on a flat, hydrophobic and very smooth surface, information of the evaporative behaviour at the macroscale is important to identify some of the underlying mechanisms that govern the structuring of nanoparticles following *free* evaporation. A 3 µl droplet of TiO_2-ethanol, prepared following the two-steps method as explained in Section 3.2.1.2, was gently deposited on a Teflon substrate. Thereafter the complete evolution of the droplet profile was recorded and analyzed using a drop shape analyzer (DSA100, see Section 3.1.1). Figure 5. 1 shows (a) the complete evolution of the contact angle, θ (deg), and contact radius, R (mm), vs. time, t (seconds) and (b) inverted photograph of the solid surface and deposits after

the complete evaporation using a Zeiss Stemi 2000-C stereo miscroscope for both 0.1% and 0.2% TiO_2-water nanofluids.

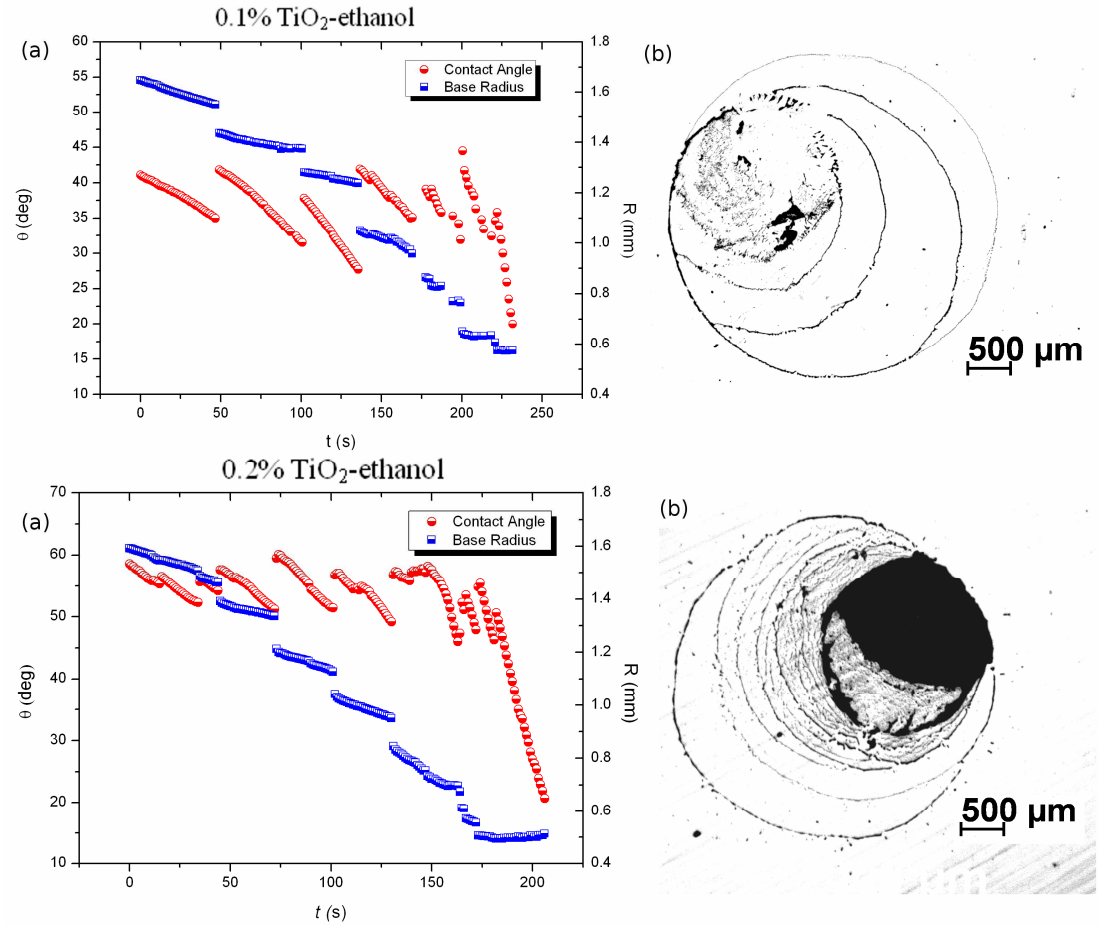

Figure 5. 1 – (a) Evolution of contact angle, θ (deg), and contact radius, R (mm), vs. time, t (seconds), for 0.1% TiO_2-ethanol and 0.2% TiO_2-ethanol and (b) inverted picture of solid substrate and deposits after complete evaporation.

The evaporative behaviours presented in Figure 5. 1 (a) show typical "stick-slip" behaviour reported recently in literature [106], and which was predicted long time ago [141]. Three to four steps, jumps or "slips" of the TCL and the associated changes in contact angle, can be clearly identified in Figure 5. 1 (a), which are supported by the different rings-like stain shown in Figure 5. 1 (b). For the system TiO_2-ethanol evaporating on hydrophobic substrates, nanoparticles are also dragged

towards the contact line, due to capillary flows within the droplet to replenish the liquid evaporated, impeding the receding movement of the latter. Contact angle decreases and droplets gains internal energy the jump ensues. “Stick-slip” behaviour is consistent throughout evaporation. Looking at the evaporative behaviour presented in Figure 5. 1 (a), it can also be observed that the pinning of the TCL is not complete; there is a slight drift of the TCL or “pseudo-pinning” together with a reduction in the contact angle following evaporation. It is worth noting the thickness of the outermost ring being greater for the higher of the concentrations tested, and that pinning of the TCL occurs preferentially/initially in one of the droplet side presumably due to irregularities on the surface.

Evaporation of droplets takes place mainly at the TCL inducing a capillary flow from the bulk of the droplet towards the TCL in order to replenish the liquid evaporated [28] . In the case of colloidal suspensions, capillary flows drive both liquid and particles in suspension towards the triple TCL prompting the pinning of this latter due to the accumulation of solute [27, 102]. This accumulation of solute leads to the build-up of particles at the TCL that might modify substrate properties, acting as artificial defects, hindering the receding movement of the TCL [143]. At this point, contact angle decreases and the thermodynamic equilibrium of the droplet is altered. The droplet’s free energy is increased due to an unbalance Young equation (Equation 4.3) until this energy is high enough to overcome the potential energy barrier for the jump to ensue towards a more thermodynamic-favourable position as discussed in literature [141] and already addressed in Chapter 4.

5.2 Deposition at the Nanoscale

Information on the structuring and features of the deposits at the nanoscale following evaporation becomes of paramount importance to fully understand the mechanisms controlling these particles [107] . AFM offers great resolution, down to the atomic scale, in both horizontal and vertical planes, ideal to visualize the built-up of nanoparticles. After the complete dry-out of the 0.1% TiO_2-water nanofluid droplet,

substrate and deposits were further dried at 100 ºC for 3 hours to remove any liquid. Thereafter the imaging of different areas of the outermost ring was carried out using AFM. For more information about the experimental procedure followed, see Section 3.1.4.2. AFM analysis was carried out in collaboration with Alexandros Askounis during his MSc at the Institute for Materials and Processes at the University of Edinburgh.

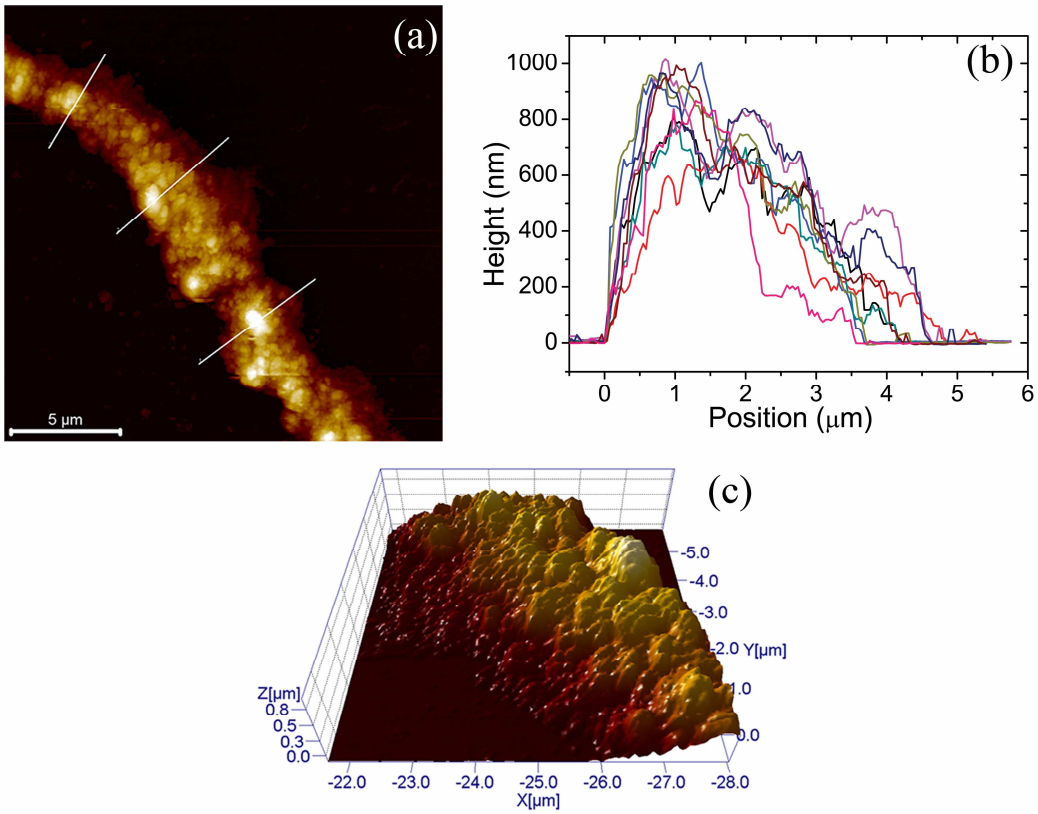

Figure 5. 2 - (a) 20 x 20 μm^2 topography image part of the outermost ring and (b) height (nm) and width (μm) of the profiles extracted from (a). (c) Three dimensional AFM image rotated 180º with respect to (a).

Figure 5. 2 includes information extracted using AFM and after processing the images in SPIP™. Figure 5. 2 (a) includes a 20 x 20 μm^2 AFM image representing the topography of the outermost ring depicted in Figure 5. 1 for 0.1% TiO_2-water

nanofluid. In Figure 5. 2 (b) different deposit profiles perpendicular to the ring presented in Figure 5. 2 (a), white lines, are included. It is worth noting that the steeper part in Figure 5. 2 (b) represents the inner part of the ring whereas there is a *gentle* slope together with terraces when moving outwards [140]. Figure 5. 2 (c) represents a 3D image of the same deposit shown in Figure 5. 2 (a) rotated 180º to be able to observe more clearly the ring-stain deposition.

5.3 Deposition Theory

In what follows the organization of nanoparticles and the shape of the deposits found after the complete dry-out of a pinned volatile droplet is addressed. This theory was developed in association with Professor Martin E. R. Shanahan from the Institut du Mécanique et d'Ingénierie de Bordeaux, University of Bordeaux, France.

Considering the evolution with time of contact radius, R, and contact angle, θ, during a typical 'stick' period, Figure 5. 1 (a), we note that the former remains essentially constant, as expected, although there is slight, linear drift, whereas the latter decreases quite markedly, also approximately linearly. We may rewrite:

$$R(t) \approx R_i - \dot{R}t \qquad (5.1),$$

$$\theta(t) \approx \theta_i - \dot{\theta}t \qquad (5.2),$$

Where $\dot{R}$ and $\dot{\theta}$ are respectively recession rates of the two parameter $R(t)$ and $\theta(t)$, suffix i corresponds to the initial value at the start of a 'stick' period, and time, t, is measured from this same starting point (after 'slip'). Distance x represents relative movement of the triple line *during 'stick'*, given by $x = \dot{R}t$.

Because of the very nature of the 'stick' phenomenon, $\dot{R}/\dot{\theta} << R_i/\theta_i$, although we may not ignore $\dot{R}$ in the following.

A schematic representation of the wetting front during the *'stick' period* is included next.

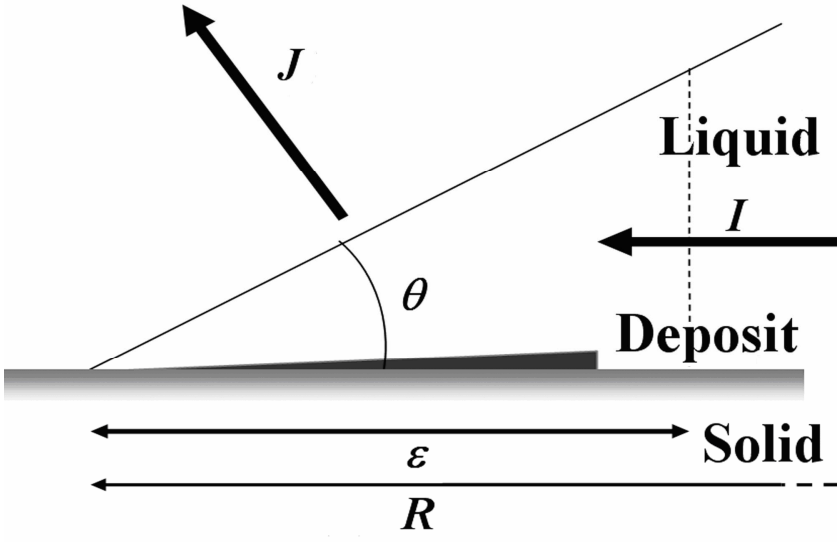

Figure 5. 3 – Schematic representation of the wetting front during a 'stick' period.

The local evaporative current near the triple line, $J(r)$, given as a mass flux, will induce an outward advective current in the liquid, $I(r)$, parallel to the solid surface [102]. These will be related by $I(r) = J(r)/\sin\theta$. We shall assume that this simplification is valid over an effective, small, characteristic length, of ε, or height, $\varepsilon \tan\theta$ (Figure 5. 3). We can, at present only surmise that ε is of the order of 100 nm, or possibly less. This flow will lead to a build-up of particles within the liquid near the triple line, since liquid evaporating is replaced by liquid flowing in, but the nanoparticles remain in suspension. Neglecting any motion of the triple line for the present, over height $\varepsilon \tan\theta$ and per unit length of triple line, there is an advective input of $\bar{I}\varepsilon \tan\theta$, where $\bar{I}$ is average current, or allowing for an initial (bulk) mass

fraction of nanoparticles of f_i, an accumulation rate of suspended solid of $f_i \bar{I} \varepsilon \tan \theta$.

Assuming that the triangular region of the liquid front, denoted by ε , may be treated as of constant dimensions and taking ρ_L as liquid density, it is readily found that the mass fraction of nanoparticles as a function of time, $f(t)$, is given by:

$$f(t) = f_i \left(1 + \frac{2 \bar{J} t}{\rho_L \varepsilon \sin \theta} \right) \tag{5.3}.$$

Local average evaporation current, $\bar{I} \varepsilon \tan \theta$, may be estimated from the expression given by Deegan et al. [102]:

$$J(r) = J_0 \left(1 - \frac{r^2}{R^2} \right)^{-\lambda} \tag{5.4},$$

in which r is the radial distance from the drop central axis and the exponent is represented by $\lambda = 0.5 - (\theta / \pi)$, using the apparently superior form for the exponent given by Hu and Larson [103] . J_0 is the reference flux at the drop centre, essentially constant. Allowing for the fact that the evaporation current here being considered is near the triple line, in the vicinity of $r = (R - x)$ where $x << R$, expression 5.4 may be simplified and integration over the region of extent ε gives the local average current:

$$\bar{J} \approx \frac{J_0}{(1 - \lambda)} \left(\frac{R}{2\varepsilon} \right)^{\lambda} \tag{5.5}.$$

Now, if evaporation is occurring (principally) over region ε, in unit time the *volume* build-up of particles (per unit length of triple line) will be approximately $f(t)\bar{J}\varepsilon/\rho_S$, where ρ_S represents the effective density of the nanoparticles in the configuration adopted in the deposit. Also in unit time, the triple line recedes by $x \approx \dot{R}$. Thus, the local height of the deposit, $h(t)$, will be given by:

$$h(t) \approx \frac{f(t)\bar{J}\varepsilon}{\rho_S \dot{R}} \tag{5.6}.$$

Since our experimental observation are spatial, rather than temporal, it is convenient to eliminate time in the above, and replace it by distance, since $t \approx x/\dot{R}$. Combining Equations 5.3 and 5.6, we obtain

$$h(x) = \frac{f_i \bar{J}\varepsilon}{\rho_S \dot{R}}\left(1 + \frac{2\bar{J}x}{\dot{R}\rho_L \varepsilon \sin\theta}\right) \tag{5.7}.$$

Equation 5.7 contains various quantities that are difficult to quantify, but the essential feature to explain our results is present. The height of the deposit, $h(x)$, can be seen to grow (approximately) linearly with distance along the solid during the 'stick' phase. Examination of Figure 5. 2 (b) suggests that often, if not always, the deposit is slightly concave towards the liquid side. It is possible that this could be related to the form of $\bar{J}$. As may be seen from Equation 5.5, there is a λ power dependence to the $(R/(2\varepsilon))$ term. Since λ increases as θ decreases, characteristics of the 'stick' phase then $\bar{J}$ will increase, although rapid perusal shows the effect to be slight. This effect may be complicated by 'layering' of the deposited particles: the deposits is in fact 'grainy' [144].

5.4 Quantitative Comparison and Discussion

In what follows, experimental results obtained at the nanoscale are demonstrated using the deposition theory developed above. To allow for the comparison between the theoretical profile of the deposits (Equation 5.7) and the different profiles obtained experimentally by AFM (Figure 5. 2 (b)), we shall attempt to quantify the different variables involved in the theory. From data obtained at the macroscale (DSA) R and θ are known and the average velocity of the TCL, $\dot{R}$, during the "pseudo-pinning" of the TCL is ca. $2.1 \cdot 10^{-6} m/s$. Additional experiments on free evaporation of ethanol yielded an average value for the reference flux at the droplet centre equal to $J_0 = 1.5 \cdot 10^{-3} kg/m^2/s$. Substituting R, θ, J_0 calculated experimentally and different values for the characteristic length ε in Equation 5.5, the local average current $\bar{J}$ can be calculated. In order to obtain the theoretical height of the deposits versus width $h(x)$ for the first ring, $\bar{J}$, $\dot{R}$, different angles and radial position (x) changing in time during the *'stick' period* were substituted in Equation 5.7 and represented in Figure 5. 4. It is worth mentioning that the build-up of particles, for the first ring, 1 μm tall after 4 μm of deposits took place during the first *'stick' period* ca. 50 seconds.

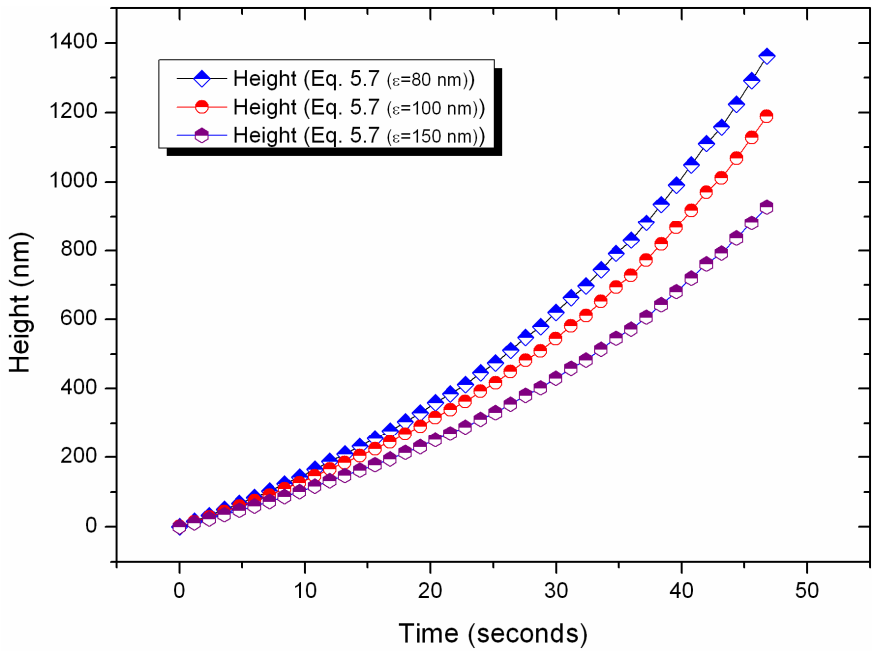

Figure 5. 4 – Shows height of the deposits, h (nm) versus time, t (seconds), calculated for the following characteristic lengths; $\varepsilon = 80nm$, $\varepsilon = 100nm$ and $\varepsilon = 150nm$ using Equation 5.7.

To compare the theory presented in Figure 5. 4, nine experimental height profiles were averaged and plotted in Figure 5. 5 along with the calculated curves shown in Figure 5. 4. Calculated trends and experimental profiles allow us to estimate the unknown characteristic length ε, of paramount importance for modelling the deposition of these nanofluids during free evaporation.

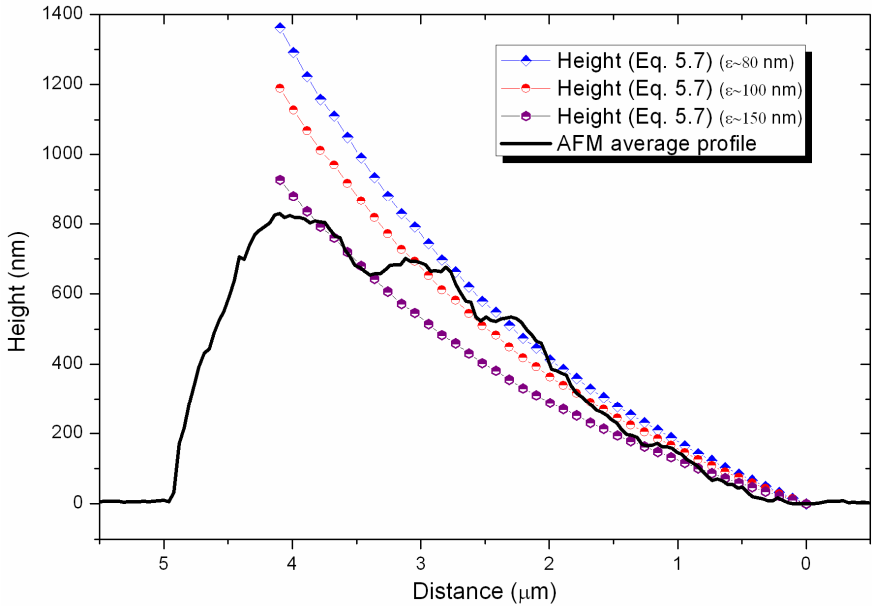

Figure 5. 5 – Comparison between experimental and theoretical results. The curvature of the predictions stems from a variation of $\bar{J}$ as a function of $\lambda(\theta)$.

From Figure 5. 5, characteristic length values proposed between 80 nm and 150 nm agree quantitatively quite well with the final averaged experimental height of the deposits. A crude comparison of the experimental and theoretical slopes can be carried out. Theoretical trend, deriving $h(x)$ with respect to x, $slope \sim \frac{dh}{dx} \sim \frac{2 f_i \bar{J}^2}{\rho_L \rho_S \dot{R}^2 \sin\theta} = 0.24$, is in very good agreement with experimental results, $slope \sim \frac{dh}{dx} \sim \frac{1}{4} = 0.25$, and we can certainly assure that the theory developed is able to predict the right profile of the deposit.

A plausible explanation for the increase in deposit height for pinned volatile droplets containing nanoparticles has been proposed although no information about what causes the jump of the TCL after a 'stick' period was obtained. At this point, we can only hypothesize that due to the relatively high elevation of the deposit, it might interfere substantially with the advective flow, $\bar{I}$, either deviating or increasing the turbulence of the flow affecting the continuity of liquid towards the TCL, $\bar{J}$.

5.5 Summary

AFM has been successfully used to identify the structuring of ring-stain deposits from *free* evaporation of nanofluid droplets at the nanoscale. We, also, report the formation of steps and/or terraces, which is a first suggestion towards the structuring of ring-stains at the nanoscale and provide the first plausible description of the mechanism that lead to these resulting structures. There is a good agreement if not perfect between theory developed and experimental profile presented. Moreover, we provide a complete description, both qualitatively and theoretically, of the the deposition process. Further work to identify the underlying mechanisms for the abrupt cut off of the advective flow to replenish the liquid evaporated at the TCL during *free* evaporation is required.

As included in Chapter 2, heterogeneities on the substrate also might modify the evaporative behaviour of both nanofluid and pure fluid. In the next chapter, the evaporative behaviour of nanofluid and pure fluid droplets on rough Aluminium vanishing at CCR is investigated. In addition, the evaporative performance under different kinetics of evaporation, i.e. different sub-atmospheric pressures, has been examined.

Chapter 6: Evaporation of Nanofluid Droplets at Sub-Atmospheric Pressure

Continuing with the efforts to expand the understanding of the mechanisms present during evaporation of nanofluid droplets, in this chapter a systematic study on the evaporation behaviour of these novel fluids for completely pinned contact lines in a nitrogen atmosphere at different sub-atmospheric pressures is carried out. Evaporation at pressures below atmospheric is a topic of great importance, playing a critical role in many applications such as separation processes, like flash distillation [145]; to maintain low temperatures on the surface during two-phase heat transfer [146-148]; or to modify the kinetics of evaporation for the structuring of particles [149, 150]. At atmospheric conditions and if the atmosphere is not saturated, a droplet deposited on a substrate will experience evaporation until the complete vanishing of the liquid. On other hand, if the thermodynamic equilibrium of a system is further altered, for example by reducing pressure, the evaporation rate is enhanced since pressure of the surroundings, i.e. boiling point, is lowered enhancing the kinetics of evaporation. In this chapter, an experimental investigation on the evaporative behaviour of Al_2O_3-water nanofluid at different sub-atmospheric pressures is carried out and a comparison with the base fluid is included along. Rough Aluminium was the substrate chosen since surface heterogeneities on the latter ensure the complete pinning of the contact line for both fluids, i.e. same evaporation behaviour reported.

6.1 Evaporation Behaviour of Al_2O_3-water Nanofluid on Rough Aluminium

The experimental evaporative behaviour of Al_2O_3-water nanofluid on rough substrates is presented next. Different nanofluid volumes, ensuring that droplet radius was below the capillary length, have been studied throughout complete evaporation. Figure 6. 1, shows the evaporation behaviour of 0.1% Al_2O_3-water nanofluid on rough Aluminium in nitrogen atmosphere and at 80 kPa. Linear regression of volume versus time is included to illustrate the constant mass loss during evaporation.

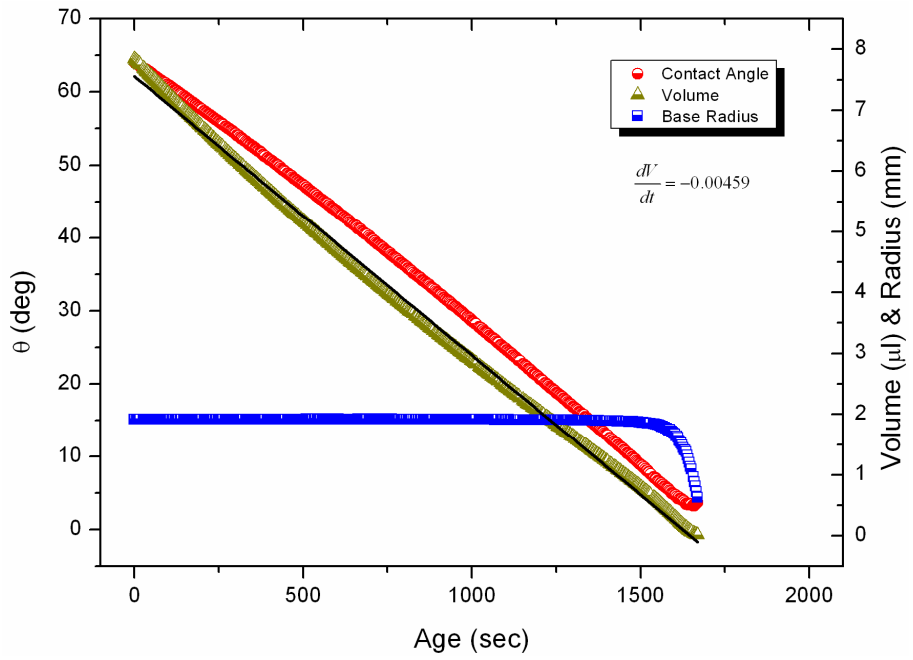

Figure 6. 1 – Evolution of contact angle, θ (deg), base radius, R (mm), and volume, V (µl), versus time, t (sec) of 0.1% Al_2O_3-water nanofluid on rough Aluminium in nitrogen atmosphere at 80 kPa.

Looking at Figure 6. 1 it is clear that both nanoparticle concentration and substrate roughness ensure the complete suppression of the dynamics of the contact line at least during 90% of the droplet lifetime. With regards the other two droplet features represented in Figure 6. 1, both contact angle and droplet volume decrease linear over time as expected [9, 11]. The latter is consistent for all volumes tested with base radii below the capillary length. It is worth noting that linearity observed for the decrease in contact angle depends on the initial contact angle [16].

Additional experiments showed that the concentration of Al_2O_3 nanoparticles chosen was high enough to attain the complete pinning of the contact line on smooth and hydrophobic substrates such as Teflon. This means that the constant contact radius (CCR) mode reported for pure fluids on high-surface energy substrates (Chapter 4) can also be observed on low-energy ones if the concentration of nanoparticles is high enough. In the particular case of a droplet evaporating on a hydrophobic substrate at CCR, a different evolution of contact angle and therefore a different evaporative rate

rather than linear has been reported. A more detailed analysis of this latter is included in the work of Gelderblom et al. [91].

Since rate of evaporation certainly depends on droplet base radius, rate of evaporation, dV/dt (µl/s), versus base radius, for different nanofluid droplet volumes at different sub-atmospheric pressures is represented:

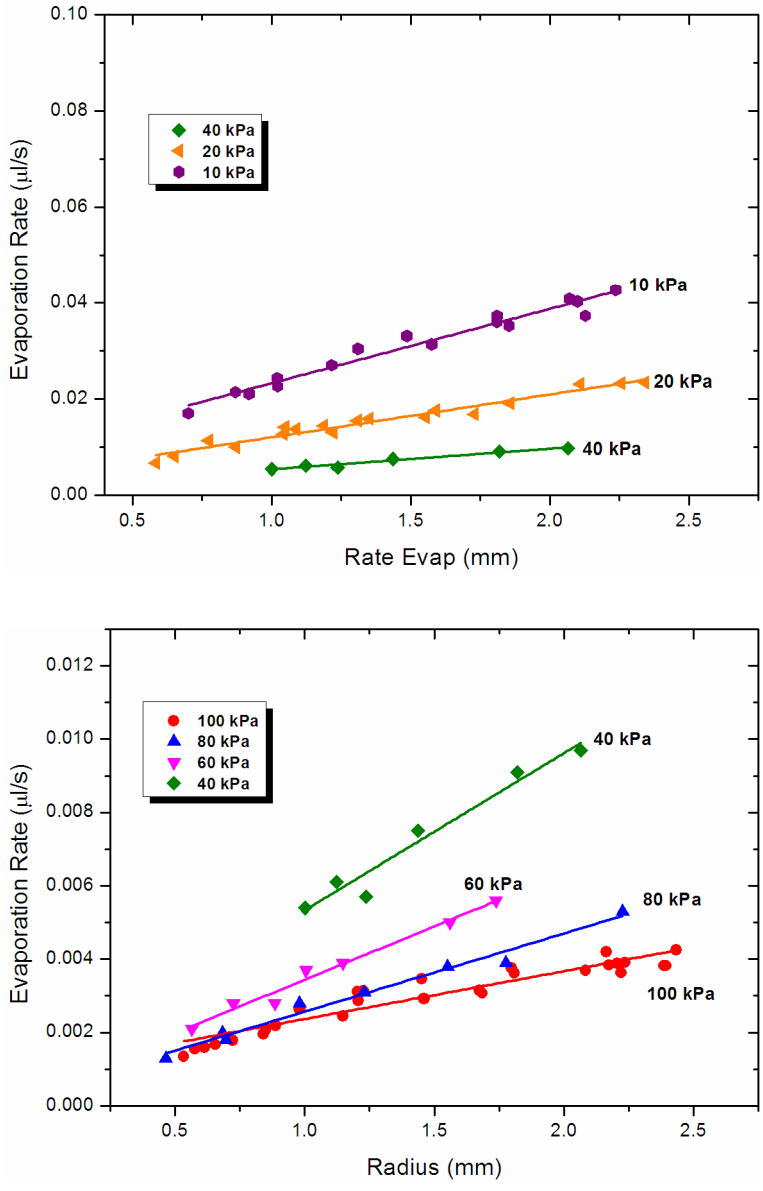

Figure 6. 2 - Rate of evaporation, dV/dt (µl/s), versus contact radius, R (mm), for 0.1% Al_2O_3-water in nitrogen atmosphere at 100, 80, 60, 40, 20, and 10 kPa.

Experimental results show that evaporation rate increases linearly with base radius, and this relationship is consistent for all sub-atmospheric pressure tested and with the literature [9, 14]. Evaporation rate is also enhanced when working at sub-atmospheric pressures since pressure inside the chamber gets closer to the vapour pressure of the fluid, thus greater driving force for evaporation to occur. From these results, linear relationships between evaporation rate and base radius for Al_2O_3-water nanofluid at different sub-atmospheric pressures are drawn.

6.2 Evaporation Behaviour of Pure Water

Pinning observed in Section 6.1 was due to both irregularities on the substrate and addition of nanoparticles. On the case of deionised water, the complete pinning of the contact line is also reported, in this case, *only* due to substrate irregularities. CCR is reported for the pure fluid case throughout evaporation allowing for an easier comparison between nanofluid and the base fluid. Figure 6. 3, shows typical evaporation behaviour of a water droplet on rough Aluminium as base radius, contact angle and volume versus time. Linear regression to show the evaporation rate behaviour is included along with experimental data.

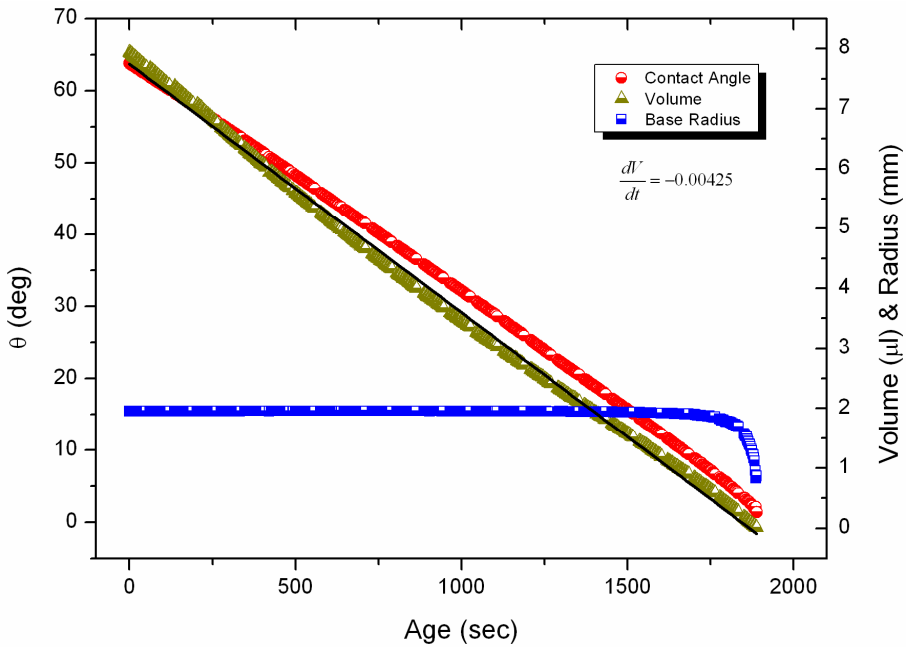

Figure 6. 3 – Evolution of contact angle, θ (deg), base radius, R (mm), and volume, V (µl), versus time, t (sec) of pure water on rough Aluminium in nitrogen atmosphere at 80 kPa.

Evaporation at constant contact radius is also reported for the pure water case on rough Aluminium. Contact line remains pinned throughout evaporation and both contact angle and droplet volume decrease linearly over time to account for the loss of volume due to evaporation. Evaporation at constant rate is evident. Figure 6. 3 also resembles the evaporative behaviour reported for pure water on very hydrophilic substrates, i.e. glass as shown in Figure 4. 1.

Since pinning contact lines lead to constant rates of evaporation, representation of the evaporation behaviour for pure water droplets at different volumes and at different sub-atmospheric pressures can be carried out. Figure 6. 4 shows rate of evaporation, dV/dt (µl/s), versus radius for deionized water in nitrogen atmosphere at different sub-atmospheric pressures:

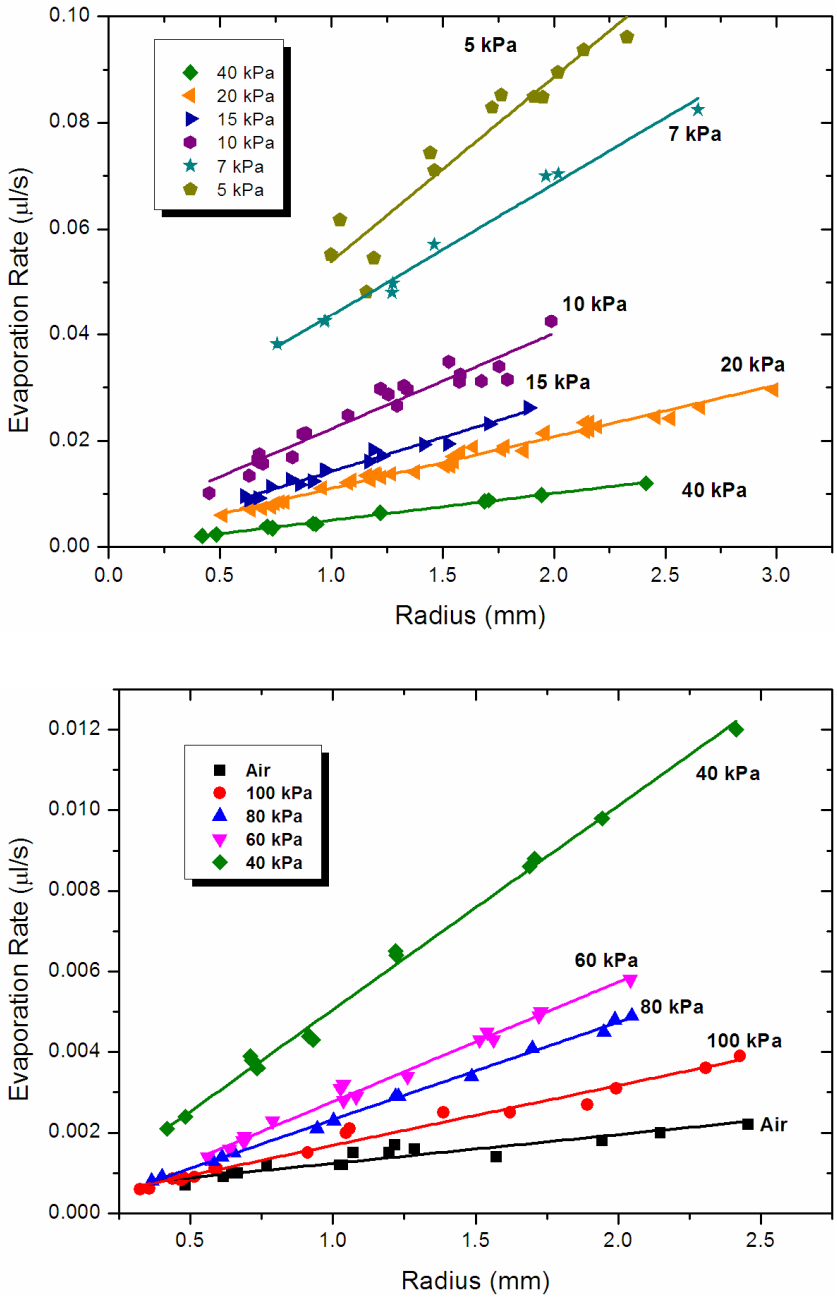

Figure 6. 4 - Rate of evaporation, dV/dt (µl/s), versus contact radius, R (mm), for water at in nitrogen atmosphere at 100, 80, 60, 40, 20, 15, 10, 7 and 5 kPa. Rate of evaporation in air atmosphere is included for comparison.

From Figure 6. 4 it is clear that rate of evaporation increases fairly linearly with droplet radius, which is in agreement with the literature reviewed [9, 14]. As observed in the previous section, greater evaporation rates are found when

decreasing the pressure of the system, which is consistent for all pressures tested: 100, 80, 60, 40, 20, 15, 10, 7 and 5 kPa, as included in Figure 6. 4. When comparing different environments, smaller rates of evaporation are found for evaporation in air since the presence of water vapour in the environment leads to lower driving force when compared to pure nitrogen atmosphere as already reported by Sefiane et al. [151]. It is worth mentioning the scatter observed when decreasing pressure, below 10 kPa, due to evaporation occurring ten to twenty fold quicker than at atmospheric pressure.

Once presented the results regarding the evaporation rate for both Al_2O_3-water nanofluid and the pure water case on rough Aluminium at different sub-atmospheric pressures, a discussion of these latter is carried out.

6.3 Discussion

6.3.1 Al_2O_3-water Nanofluid

Rate of evaporation divided by the base radius has been calculated and represented versus base radius for each individual Al_2O_3–water nanofluid droplet. Trend lines have been included for each sub-atmospheric pressure.

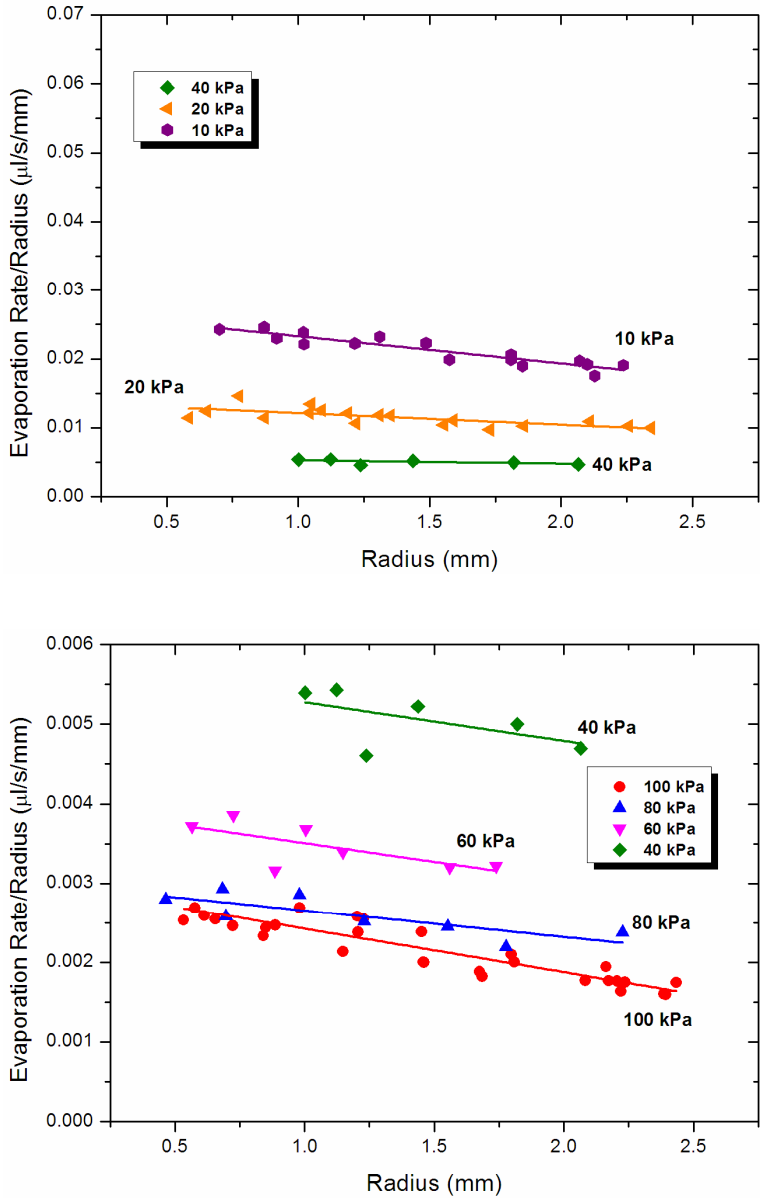

Figure 6. 5 – Rate of evaporation per base radius (μl/s/mm) represented versus radius, R (mm), for 0.1% Al_2O_3-water nanofluid in nitrogen atmosphere at different sub-atmospheric pressures (kPa).

The analysis above suggests that rate of evaporation on hydrophilic substrates and pinned contact line is closely linked to the perimeter of the contact line since fairly constant values of the rate of evaporation per base radius are found. Then for bigger droplets, greater rates of evaporation are expected and these in turn exhibit quicker evaporation rates per base radius when decreasing pressure.

6.3.2 Water

The same analysis was carried out for the results obtained during evaporation of deionized water. A constant evaporation rate per base radius was found for pressures above 10 kPa as it can be extracted from the next figures:

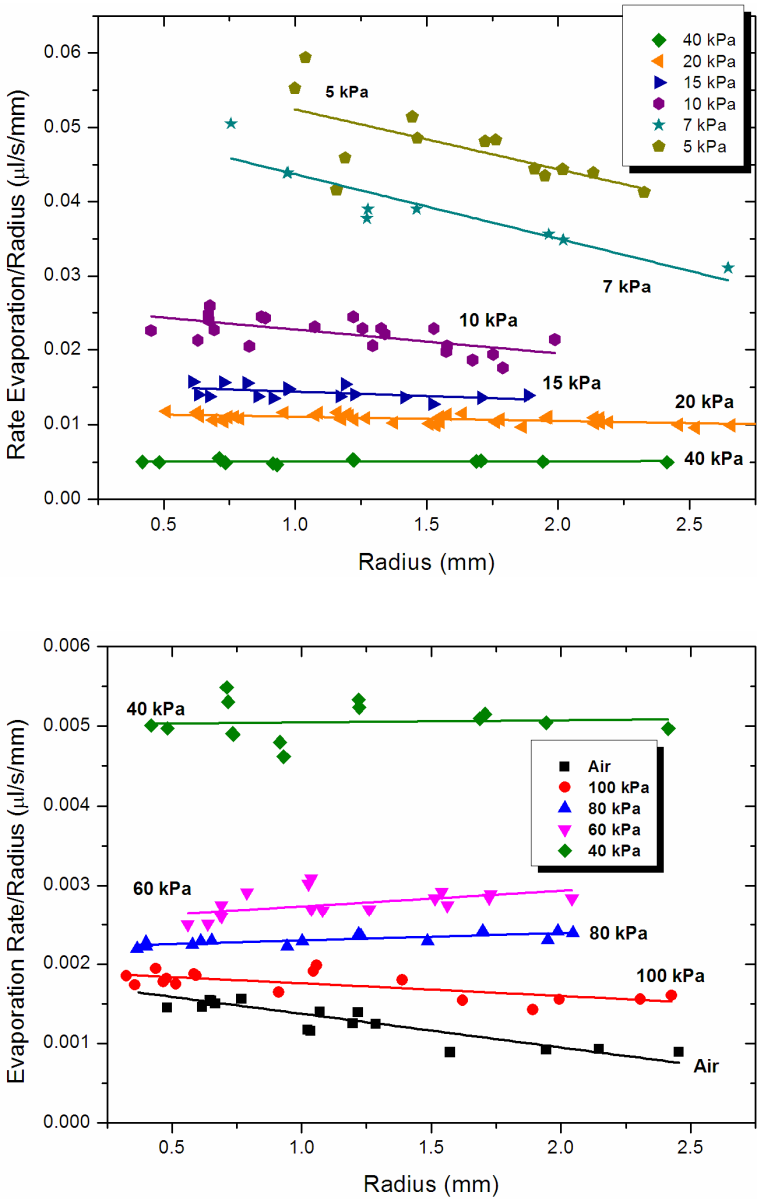

Figure 6. 6 –Evaporation rate per radius versus radius (µl/s/mm) for pure water case in nitrogen at different sub-atmospheric pressures (kPa). Results in atmospheric air are included for comparison.

Similar findings to those observed for the nanofluid case are also reported in this subsection. Looking at Figure 6. 6, a fairly constant rate of evaporation per base radius is found for the range of volumes tested and pressures above 10 kPa. Mentioned rate of evaporation per base radius also increases when decreasing the pressure of the system.

6.3.3 Comparisson

At this point, a comparison between the evaporation rate per base radius of both fluids in nitrogen at different sub-atmospheric pressures is presented in Figure 6. 7:

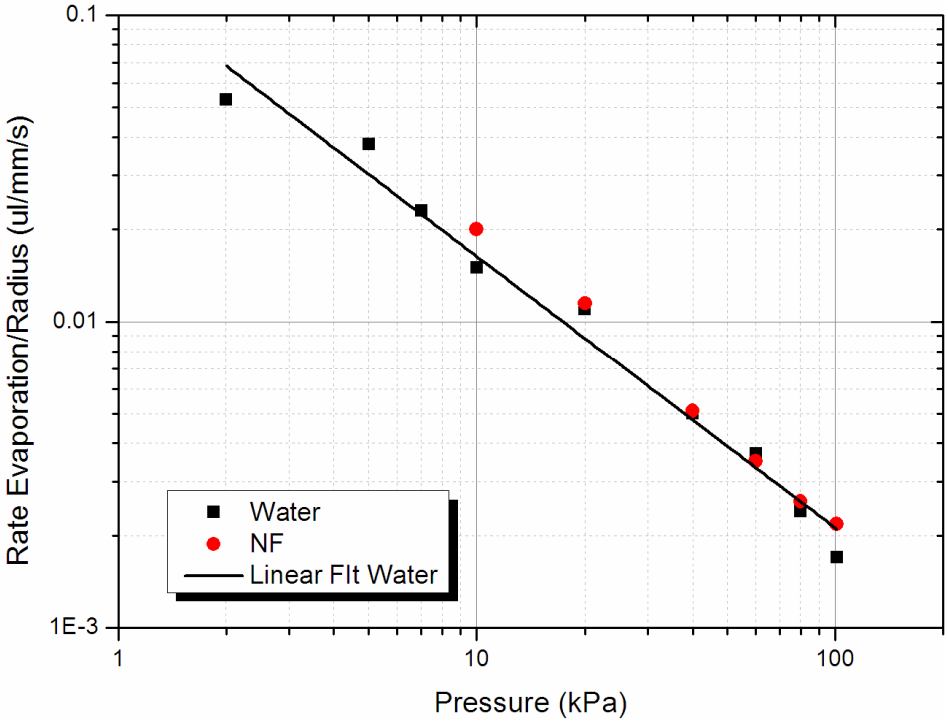

Figure 6. 7 – Log-log plot of rate of evaporation per unit of radius (µl/s/mm) versus pressure (kPa) for 0.1% Al_2O_3-water nanofluid and the pure water case in nitrogen atmosphere. Power law correlation included for the pure water case to illustrate trend.

A power law correlation adjusts fairly well to the rate of evaporation per base radius versus pressure for the pure water case. This model can help to predict the time required for a droplet to undergo evaporation until complete disappearance for pinned contact lines and pressures ranging from 2 kPa to atmospheric one. Nanofluid case has been included in Figure 6. 7, for an easier comparison, and no appreciable change in evaporation rate when compared to the pure fluid case is observed.

At this point, it can be stated that evaporation rate for pinned contact lines increases proportionally with base radius and with decreasing the pressure of the system. On other hand, mentioned rate of evaporation is independent of nanoparticle concentration since the same droplet evolution is ensured due to the features of the substrate, i.e. roughness. Complete pinning of the contact line on both cases (nanofluid and pure fluid) leads to a practically similar evaporative behaviour as it can be observed from the next figure:

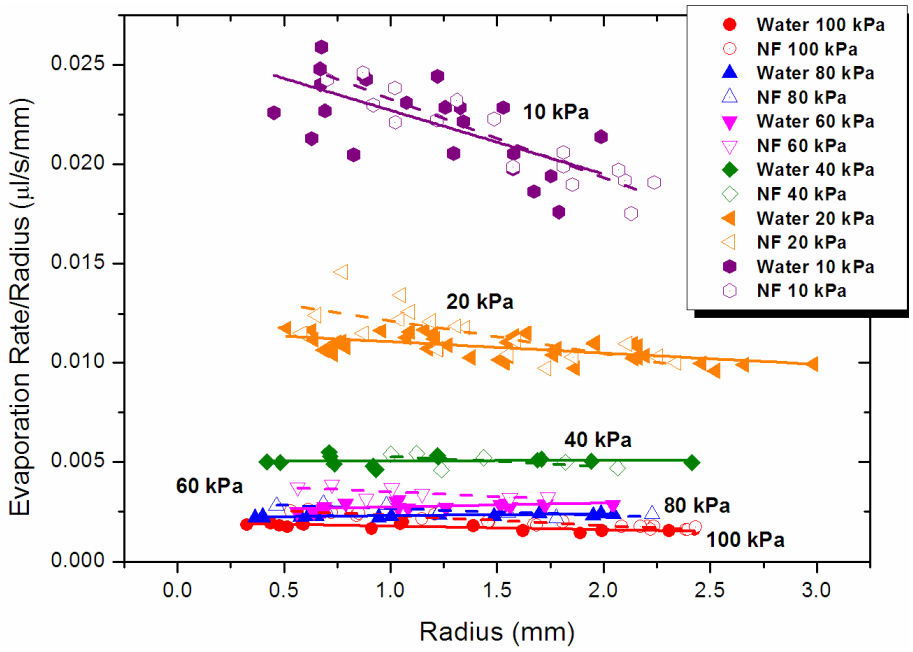

Figure 6. 8 – Rate of evaporation per base radius (µl/s/mm) vs. base radius, R (mm), for water (solid symbols) and 0.1% Al_2O_3-water nanofluid (open symbols) in nitrogen atmosphere at different sub-atmospheric pressures.

6.3.4 Additional Considerations, Pinning of the Contact Line

The evaporative behaviour of pure water on rough Aluminium, Figure 6. 3, resembles the same evaporative mode reported for deionized water on smooth glass, i.e. Figure 4. 1. As it was pointed out the high surface energy of the glass substrate leads to low equilibrium contact angles and to an insufficient depinning force for the contact line to detach. On the other hand, equilibrium contact angle of pure water on rough Aluminium being ca. 60º (Figure 6. 1) suggests that the free energy gained by the droplet throughout evaporation will be high enough for the contact line to depin before the complete dry-out as demonstrated in Section 4.4.1. Although, in this case there is an extra energy barrier due to the presence of irregularities on the substrate impeding the receding of the contact line even for high initial contact angles or big changes of this latter, i.e. $\partial U/\partial r)_{rough\_Al} > \partial \vec{F}$. Then roughness of the surface is an important parameter ruling droplet evaporation since the heterogeneities can be great enough to attain the complete pinning of the contact line, evaporation at CCR, even for really high initial contact angles, ca. $\theta_0 \sim 140°$ [91].

In the case of Al_2O_3-water nanofluids, the concentration of nanoparticles chosen prompts the complete pinning of the contact line when comparing to the base fluid, although on the case of rough Aluminium the complete pinning was already reported without further particle addition. This means that no further pinning of the contact line is attained due to the addition of nanoparticles, i.e. evaporative behaviour is undistinguished. It is predictable that if a droplet of pure water evaporates at constant contact radius on rough Aluminium, a water droplet containing particles will be pinned as well during the whole period of evaporation.

Either way, on rough Aluminium, contact line remains pinned during most of the droplet lifetime leading to constant rate of evaporation in time, Figure 6. 1 and Figure 6. 3 [14, 152].

6.4 Summary

In this chapter, a comparison between the evaporative behaviour of Al_2O_3-water nanofluid and the pure fluid case throughout evaporation on rough substrates and at different sub-atmospheric pressures has been carried out, to try to uncover the differences between the evaporative behaviour of pure fluids and fluids containing nanoparticles, on both cases for pinned contact lines. The complete pinning of the contact line reported for the pure fluid case on rough Aluminium suggests that nanofluids will evaporate also at CCR. Linear evaporation rate is reported for the vanishing of both nanofluid and deionized water droplets at the different sub-atmospheric pressures due to evaporation taking place at constant contact radius.

When representing evaporation rate per unit of base radius versus radius, a fairly constant value is obtained for each of the sub-atmospheric pressures studied. Representing this value versus pressure, a good agreement if not perfect following a power law is reported. Moreover, since either droplet evaporative behaviour or dynamics of the contact line are not modified during evaporation by the addition of nanoparticles, no appreciable enhancement in droplet lifetime in this type of substrates is observed. On the other hand, on hydrophilic and smooth substrates the addition of nanoparticles led to faster evaporation times, which can be beneficial for cooling applications [89].

The following two chapters of the thesis include the experimental research carried on electrowetting of nanofluid droplets. Chapter 7 includes the effect of nanoparticle concentration, dielectric thickness and voltage on the electrowetting-dewetting movement of the contact line. In Chapter 8 a different evaporative behaviour was observed for nanofluids evaporating under an external electric field applied when compared to *free* evaporation.

Chapter 7: Electrowetting of Nanofluids, an Amended Young-Lippmann Equation

Electrowetting has attracted attention of the scientific community during the last decade due to the ability of manipulating liquid interfaces without requiring mechanical parts [59]. An applied voltage to a droplet may modify the interfacial tension of this latter prompting spreading [61], droplet movement [62], droplet surgery [65], internal mixing [64] or optics [153] amongst others . Despite the intensive research carried out in the topic many factors are still incompletely understood, i.e. the electrowetting of fluids different from water or ionic fluids, the choice of electrodes, type of current, electrolysis, etc. Motivated by the potential applications of this technique for the control of colloidal suspensions, in this chapter the dynamics of the contact line under DC applied voltage for TiO_2-water nanofluids and for pure the water case are addressed. Moreover electrowetting-on-dielectric (EWOD) principle has been proposed for the fabrication of a new generation of low voltage electrowetting substrates [128]. Therefore, a set of experiments on different EWOD substrates varying in thickness of the insulating layer were undertaken to investigate the effect of an applied voltage on the electrowetting-dewetting movement of the contact line for different nanoparticle concentrations. An enhancement in wettability when adding nanoparticles to the base fluid coupled with voltage was observed and explained in terms of additional interactions between the particles present and the dielectric substrate under an external voltage applied.

7.1 Effect of Dielectric Thickness for Pure Water

The effect of different dielectric materials and thicknesses on EWOD performance has already been addressed in literature [129, 154], although little research has been carried out on the EW of nanofluids. In order to emphasise the main differences between the electrowetting of nanofluids and the pure fluid case, the analysis of the behaviour of deionized water on these specific substrates under EW conditions becomes essential. Firstly $Cytop_{22}$ was the substrate studied and thereafter another two different substrates varying only in amorphous fluoropolymer (aFP) thickness as

explained in Section 3.2.2.2, i.e. $Cytop_{300}$ and $Cytop_{500}$, were investigated in order to wide this experimental part.

It is well known that the overall capacitance of an EWOD substrate depends on the material properties and the thickness of the dielectrics that constitute the substrate. Then using basic electrical principles where both Cytop and Ta_2O_5 act as capacitor in series and assuming no evaporation, the Young-Lippmann equation (Equation 2.5) can be rewritten as [129]:

$$\cos\theta(V) = \cos\theta_0 + \frac{1}{2}\frac{\varepsilon_{r1}\varepsilon_{r2}\varepsilon_0}{\gamma_{\mathrm{lg}}(d_1\varepsilon_{r2} + d_2\varepsilon_{r1})}V^2 \qquad (7.1),$$

where ε_{ri} are the different permittivities, d_i are the dielectric thicknesses, γ_{lg} is the surface tension water-gas and θ_0 the equilibrium contact angle. All variables are known allowing for the calculation of theoretical trends for $\theta(V)$. The experimental electrowetting contact angles, $\theta(V)$, versus voltage, V, on the three dielectric substrates are shown in Figure 7. 1, along with theoretical trends calculated using Equation 7.1:

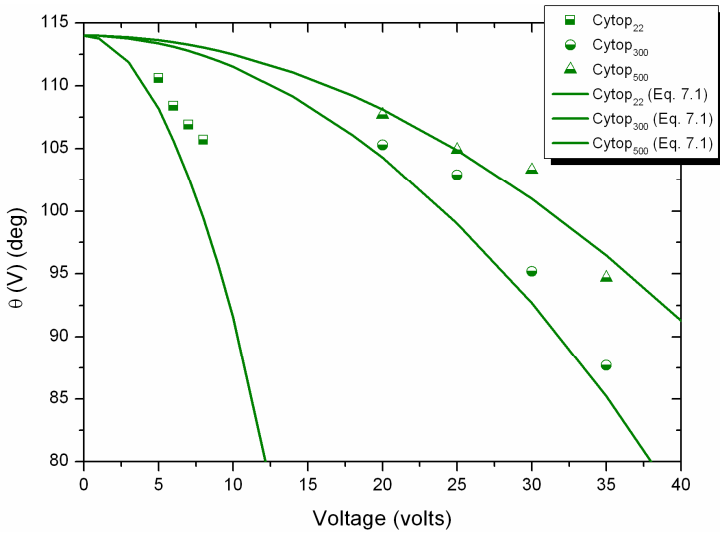

Figure 7. 1 – Electrowetting contact angle, $\theta(V)$ (deg), versus voltage, V (volts), for deionzied water on: $Cytop_{22}$ (squares), $Cytop_{300}$ (circles) and $Cytop_{500}$ (up triangles). Theoretical trends calculated using Equation 7.1 are shown to allow comparison (solid lines).

Figure 7. 1 shows that the electrowetting contact angle under an applied voltage is consistent with the features predicted by the Young-Lippmann equation long time ago on all three substrates [61]. From Figure 7. 1, it can also be inferred that greater voltages are necessary for a same observable change in contact angle when increasing the thickness of the aFP, which is consistent with electrowetting equation presented in Equation 7.1. Similar trends have been previously reported by Li et al. [129] for the same dielectric materials but different thicknesses.

These low voltage EWOD substrates require smaller voltages for the manipulation of the droplet interface in a similar way than traditional electrowetting substrates, with resulting in energy savings. On the other hand, the manipulation of the interfacial tension becomes less precise since the actuation voltage range decreases.

7.2 Effect of Nanoparticle Concentration

The addition of nanoparticles coupled with electrowetting is introduced in this subsection. Different TiO_2-water nanofluid concentrations were prepared and the final contact angle under an applied voltage, $\theta(V)$ (deg), was measured on all three dielectric substrates; $Cytop_{22}$, $Cytop_{300}$ and $Cytop_{500}$. Figure 7. 2 (a), (b) and (c) include nanofluid and deionized water experimental values of $\theta(V)$ plotted versus voltage, besides theoretical trends for the pure water case already presented on Figure 7. 1. For each concentration and voltage; 3 independent experiments were carried out, $\theta(V)$ was averaged, and standard deviations calculated and represented as error bars.

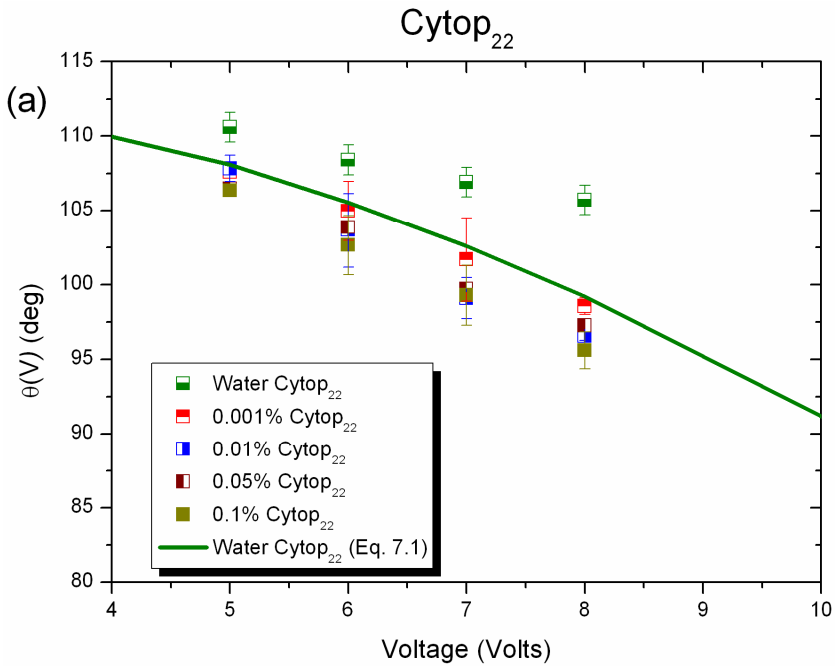

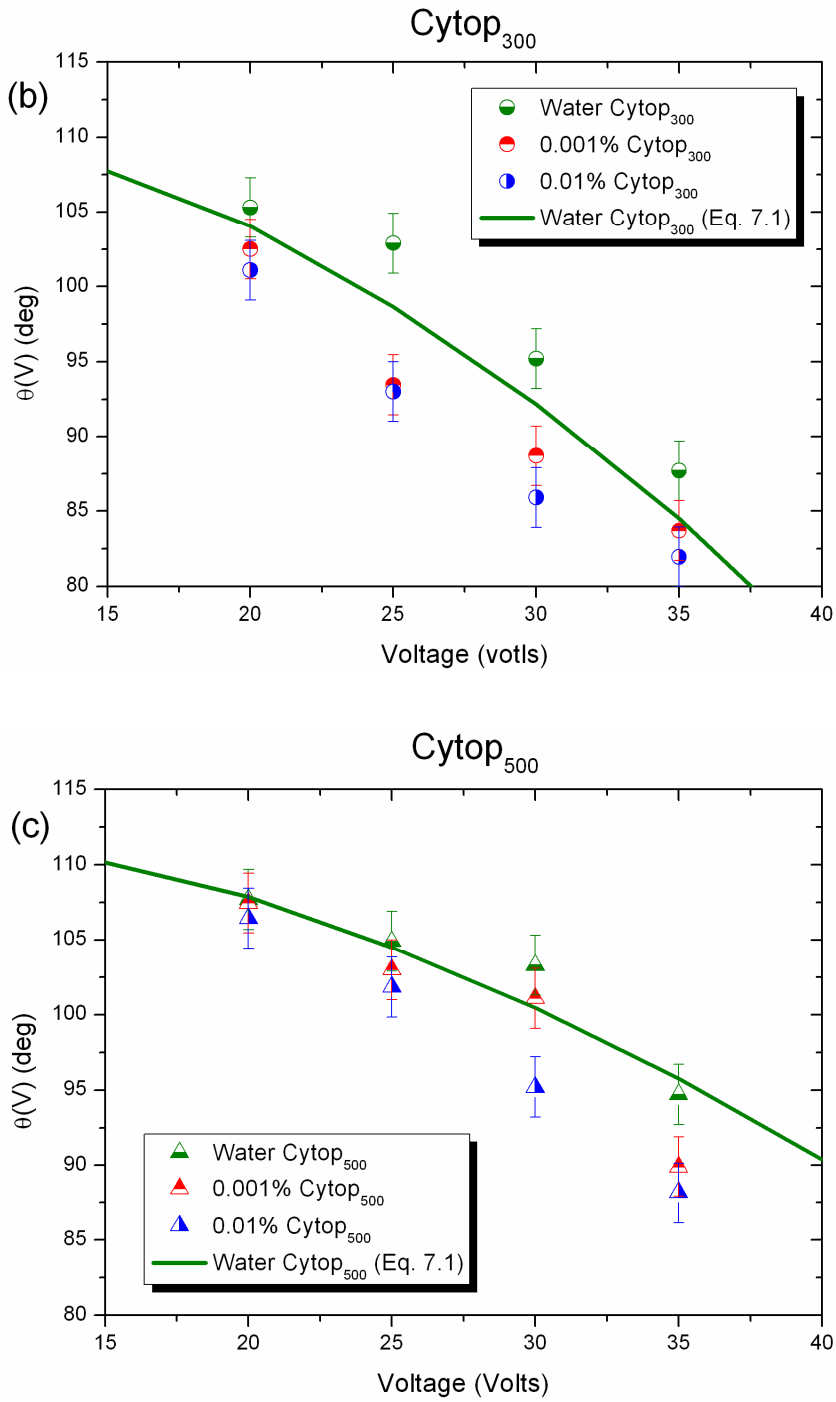

Figure 7. 2 – Electrowetting contact angle, $\theta(V)$ (deg), versus voltage, V (volts), on (a) $Cytop_{22}$ (squares), (b) $Cytop_{300}$ (circles) and (c) $Cytop_{500}$ (up-triangles) for; 0.1% (filled, dark yellow), 0.05% (filled-left, wine), 0.01% (filled-right, blue) and 0.001% (filled-up, red) TiO_2-water concentrations. Experimental (filled-down, green) and theoretical (straight solid line) values for deionized water, are included along for comparison .

Figure 7. 2 suggests that nanofluid droplets can be manipulated in a similar way as deionized water droplets under an applied voltage, i.e. lower $\theta(V)$ when increasing voltage following Young-Lippmann equation (Equation 2.5). The qualitative and quantitative agreement between Equation 7.1 and $\theta(V)$ experimental values for the *pure* fluid case results quite accurate, if not perfect. Regarding the electrowetting of nanofluids, an improved electrowettability is noticed for nanoparticle-laden liquids when compared to the *pure* fluid case, Figure 7. 2. It is clear then that theoretical trends presented for deionized water, Equation 7.1, do not account for the addition of nanoparticles.

Comparing the different nanoparticle concentrations, an improved wettability is reported when increasing concentration from 0.001% to 0.01% and up to 0.1%. It is worth noting that the improvement in electrowettability for concentrations greater than 0.01% is not as marked as for lower concentrations. The former suggests that there might be a critical concentration value above which no further enhancement in electrowetting behaviour is observed as nanoparticle concentration is increased. Results presented in Figure 7. 2 are consistent on all three substrates tested and for all voltages chosen.

7.3 Dynamics of the Contact Line

The dynamics of the contact line during both wetting and dewetting of the contact line, voltage switched On/Off, on the three different substrates are presented in this section. A high-speed camera, described in Section 3.1.3, was required to capture the very rapid movement of the contact line, up to 200 frames per second. Figure 7. 3 portrays the spreading-receding behaviour of the contact radius, R (mm), in time, t (seconds), for 0.001% and 0.01% TiO_2-water nanofluids when switching voltage On/Off. Figure 7. 3 (c) allows for the comparison of the dynamics of the contact line for a similar displacement of this latter, i.e. identical electrowetting contact angle caused by different voltages applied due to the different aFP thicknesses.

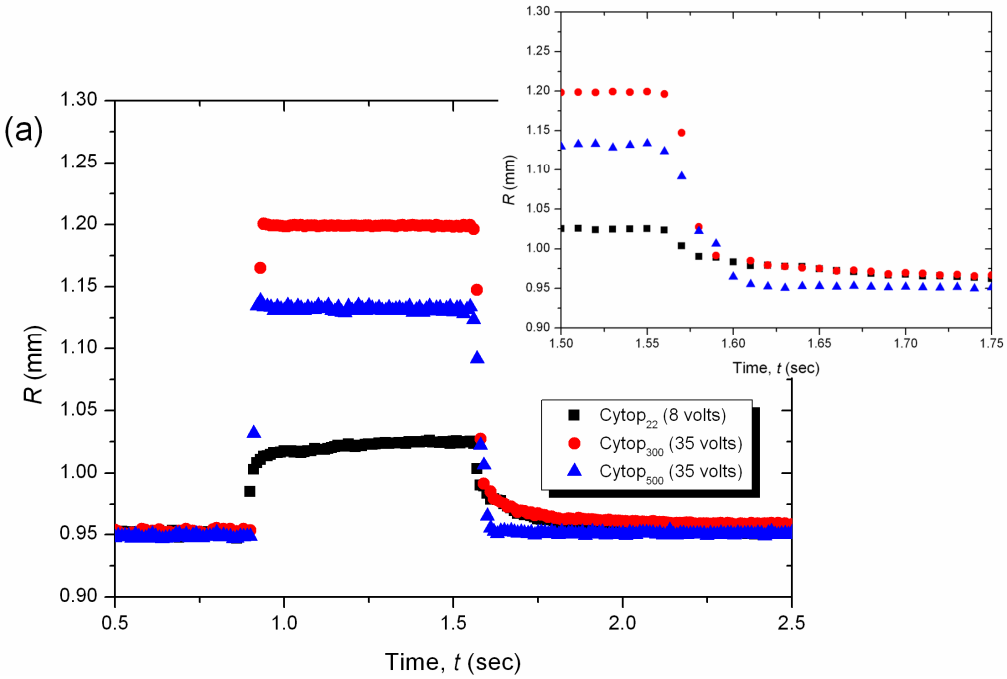
(a)
R (mm)
Time, t (sec)
Cytop22 (8 volts)
Cytop300 (35 volts)
Cytop500 (35 volts)

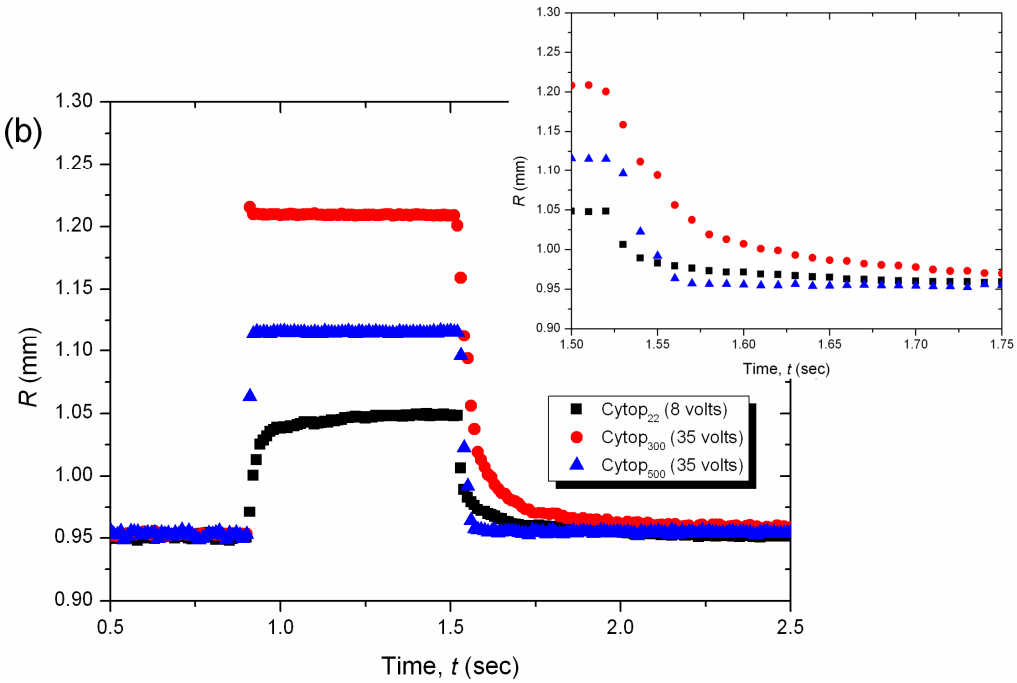
(b)
R (mm)
Time, t (sec)
Cytop22 (8 volts)
Cytop300 (35 volts)
Cytop500 (35 volts)

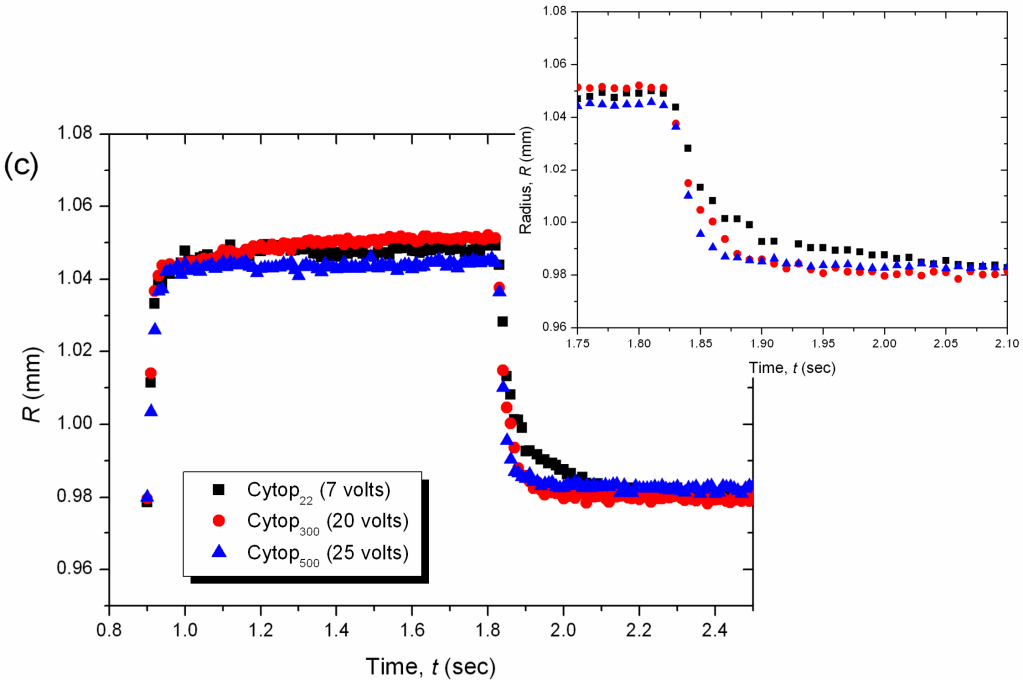

Figure 7. 3 – Contact radius evolution, R (mm), versus time, t (seconds), for (a) 0.001%, (b) 0.01% TiO_2-water and (c) for the same change in R for 0.01% TiO_2-water nanofluid. All R profiles were averaged from the first 7 experimental On/Off switching cycles on $Cytop_{22}$ (squares), $Cytop_{300}$ (circles) and $Cytop_{500}$ (up-triangles).

Looking at Figure 7. 3, it is clear that the thickness of the aFP has a marked influence on the dynamics of the contact line. The spreading movement of the contact line is very rapid ca. 0.02 seconds for voltages above 30 volts on $Cytop_{300}$ and $Cytop_{500}$, as it can be extracted from Figure 7. 3 and which is consistent with the work of Shapiro et al. [155] and that of Paneru et al. [156]. On the other hand, for the thinnest of the aFP the contact line takes ca. 0.1 seconds to reach the final electrowetting contact angle. When switching voltage Off, droplet shape returns approximately to the initial equilibrium contact angle, being faster for the thicker of the substrates, i.e. $Cytop_{500}$. It is demonstrated then that the smaller the capacitance the faster the advancing-receding movement of the contact line for these dielectric substrates when switching voltage On/Off. This latter is in agreement with capacitor theory where the greater the capacitance the longer it takes to discharge, Figure 7. 3.

When comparing the same change in contact angle, i.e. same displacement of the contact line, the thicker the dielectric the faster the relaxation, ca 0.05 seconds on $Cytop_{500}$ as shown in Figure 7. 3 (c). On the contrary, a relaxation time in the order of few tenths of a second was measured on the thinnest of the substrates, $Cytop_{22}$. Intermediate behaviour is observed on $Cytop_{300}$.

7.4 Discussion

In this subsection, a closer look at the dynamics of the contact line will help to address the effect aFP thickness and nanoparticle concentration.

The agreement between experimental results for deionized water on all three substrates and the predicted behaviour by Equation 7.1, where both the effect of aFP thickness and voltage applied were already taking into account, is quasi-perfect, Figure 7. 2. However, Equation 7.1 does not explicitly take into account the addition of nanoparticles yet, requiring additional interpretation of the phenomena governing the enhancement of spreading for nanofluids coupled with electrowetting, henceforth referred as $\theta(V,\%)$. Then we might rewrite:

$$K(\gamma_{\mathrm{lg}},\varepsilon_{ri},d_i)=\frac{C_{tot}}{2\gamma_{\mathrm{lg}}}=\frac{1}{2}\frac{\varepsilon_{r1}\varepsilon_{r2}\varepsilon_0}{\gamma_{\mathrm{lg}}(d_1\varepsilon_{r2}+d_1\varepsilon_{r2})} \qquad (7.2.1),$$

$$\cos\theta(V,\%)=\cos\theta_0+K(\gamma_{\mathrm{lg}},\varepsilon_{ri},d_i) \qquad (7.2.2),$$

where $K(\gamma_{\mathrm{lg}},\varepsilon_{ri},d_i)$ is *only* function of substrate properties; ε_{ri} and d_i, and surface tension of the fluid, γ_{lg}. Additional experiments of pendant drop included in the Table 3.1 showed no appreciable change on surface tension for the low range of TiO_2-water nanofluid concentrations tested. A consistent surface tension of 73.5 ±

0.5 mN/m for both water and TiO_2-water nanofluid between 0% and 0.1% by weight at 15 ºC was found. Moreover, no appreciable change in the surface tension liquid-gas or accumulation of nanoparticles was observed under an applied voltage. Since $K(\gamma_{lg}, \varepsilon_{ri}, d_i)$ does not depend either on nanoparticle concentration or voltage, fixed values of $K(\gamma_{lg}, \varepsilon_{ri}, d_i)$ are calculated and presented in Table 7. 1:

Table 7. 1 - K (1/volt^2) values for the different dielectric substrates varying in aFP thicknesses.

Substrate	**Cytop$_{22}$**	**Cytop$_{300}$**	**Cytop$_{500}$**
$K \cdot 10^{-3}$ (1/volt^2)	3.8	0.4	0.24

The addition of nanoparticles to the base fluid does not modify γ_{sg}. There is no accumulation or deposits left behind at the solid-gas interface since evaporation can be neglected due to the short duration of the experiments and there is the continuous advancing and receding movement of the contact line that keeps the particles in suspension. The continuous movement of the contact line under AC electrowetting at high frequencies, in the kHz range, has been reported as a method for preventing the coffee ring stain [66].

At this point, all variables present in Equation 7.2.2 with the exception of the surface tension at the solid-liquid, γ_{sl}, have been ruled out. Then, at the present the accumulation of particles at the triple contact line under an applied voltage cannot be neglected, in fact, any accumulation of particles at the liquid-solid interface will modify this latter. This strongly suggests that the application of a voltage may modify γ_{sl}, thus modifying Young-Lippmann balance and therefore $\theta(V,\%)$. A similar behaviour was found for tricresyl phosphate, which final equilibrium contact angle is modified during the spreading of the contact line due to the dynamic molecular orientation of the tricresyl phosphate molecules present [157].

Then, trying to solve the thermodynamic equilibrium using Equation 7.2.2, when a voltage is applied to a fluid containing nanoparticles, an excess of the internal energy at the solid-liquid interface is noticced. This excess of energy modifies further the $\theta(V,\%)$ and the Young-Lippmann equation, which must be taken into account when working with nanoparticles in suspensions under an applied voltage. Joshian Gibbs [121] proposed, more than a century ago, that a change in the internal energy of a system modifies the surface energy of mentioned system. In other words, if the thermodynamic equilibrium of a droplet is further altered either by a gradient of concentration or pressure the adsorption of molecules at the solid-liquid interface will take place [121, 158].

At this point of the discussion, adsorption of nanoparticles onto the solid-liquid interface when coupled with electrowetting is proposed as the mechanism modifying locally the properties of the substrate, i.e. lowering its surface tension. This reduction in surface tension due to the presence of nanoparticles and an electric voltage applied offers a plausible explanation of the mechanism governing the enhancement on spreading of these nanofluids when compared to the base fluid. The addition of nanoparticles under an applied voltage will modify further γ_{sl}, henceforth referred as $\gamma_{sl}(V,\%)$ and $\theta(V,\%)$ is modified as:

$$\cos\theta(V,\%) = \frac{\gamma_{sg} - \gamma_{sl}(V,\%)}{\gamma_{\mathrm{lg}}} = \cos\theta_0 + \frac{\Delta\gamma_{sl}(V,\%)}{\gamma_{\mathrm{lg}}} \qquad (7.3).$$

Revising Gibbs principles and the latest work related to adsorption of molecules on solid-liquid interfaces, Equation 7.3 is proposed as the additional electrostatic term reducing the interfacial tension solid-liquid and therefore the final $\theta(V,\%)$; in our case driven by both voltage and the presence of nanoparticles. An analogous expression initially proposed by Gibbs [121] and modified in the work of Ward et al. [158] to express the change in surface tension, $\Delta\gamma_{sl}(V,\%)$ at the solid-liquid interface is presented:

$$\Delta\gamma_{sl}(V,\%) = \gamma_{\mathrm{lg}} A\chi^{1/3}\Delta V \qquad (7.4).$$

This is a Gibbs-type adsorption term at the solid-liquid interface, in this case, triggered by a difference of voltage, ΔV, instead of a gradient of pressure or concentration. Further analysis of the data gathered during this experimental part showed an reduction in surface tension when increasing nanoparticle concentration proportional to $\chi^{1/3}$ where χ is nanoparticle concentration. Since the spreading of the contact line was observed in only one dimension, it is self-evident that the influence of concentration/volume will affect the cubic root of the volume, i.e. $\sqrt[3]{V} \sim \sqrt[3]{\chi} \sim \chi^{1/3}$. The coefficient A is an empirical value obtained using Maple software and equal to 0.0045. This empirical value was firstly obtained from the experiments carried out on $Cytop_{22}$ and then extended to the other two substrates, i.e. $Cytop_{300}$ and $Cytop_{500}$, with the consequently good agreement.

Then combining Equation 7.1, Equation 7.3 and Equation 7.4, a revisited Young-Lippmann expression, Equation 7.5, brings together the effect of an applied voltage for fluids containing nanoparticles:

$$\cos\theta(V,\%) = \cos\theta_0 + \frac{1}{2}\frac{\varepsilon_{r1}\varepsilon_{r2}\varepsilon_0}{\gamma_{\mathrm{lg}}(\varepsilon_{r1}d_2 + \varepsilon_{r2}d_1)}V^2 + 0.0045\chi^{1/3}V \qquad (7.5).$$

It is possible now to calculate theoretical trends for the different nanofluid concentrations and thicknesses of the aFP, $\theta(V,\%)$ using Equation 7.5. Figure 7. 4, shows theoretical trends portrayed as $\theta(V,\%)$ versus voltage:

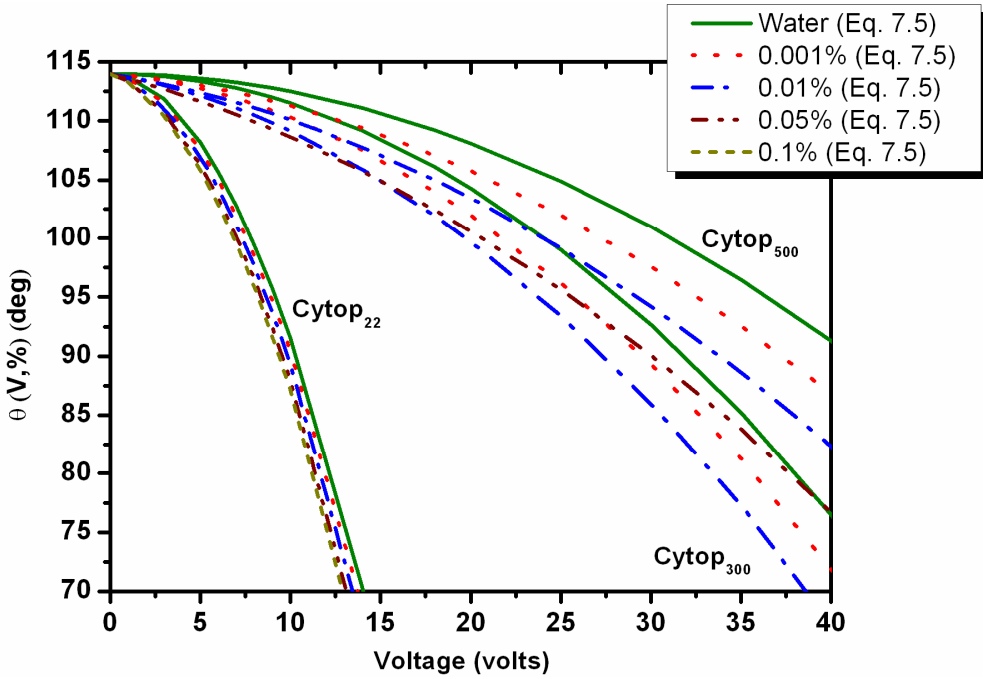

Figure 7. 4 – Theoretical trends for $\theta(V,\%)$ calculated using the proposed Equation 7.5 are presented for all three substrates and for the different TiO_2-water concentrations tested; 0.1% (dashed line), 0.05% (dot-dot-dashed line), 0.01% (dot-dashed line), 0.001% (dotted line) and for the pure water case (solid line) on $Cytop_{22}$, $Cytop_{300}$ and $Cytop_{500}$.

Figure 7. 4 shows that theoretical trends certainly follow the features predicted by the Young-Lippmann equation when including an additional term to account for the addition of nanoparticles coupled with electrowetting. To confirm the agreement between Equation 7.5 and experimental results, theoretical trends are included next along with experimental results for all three substrates.

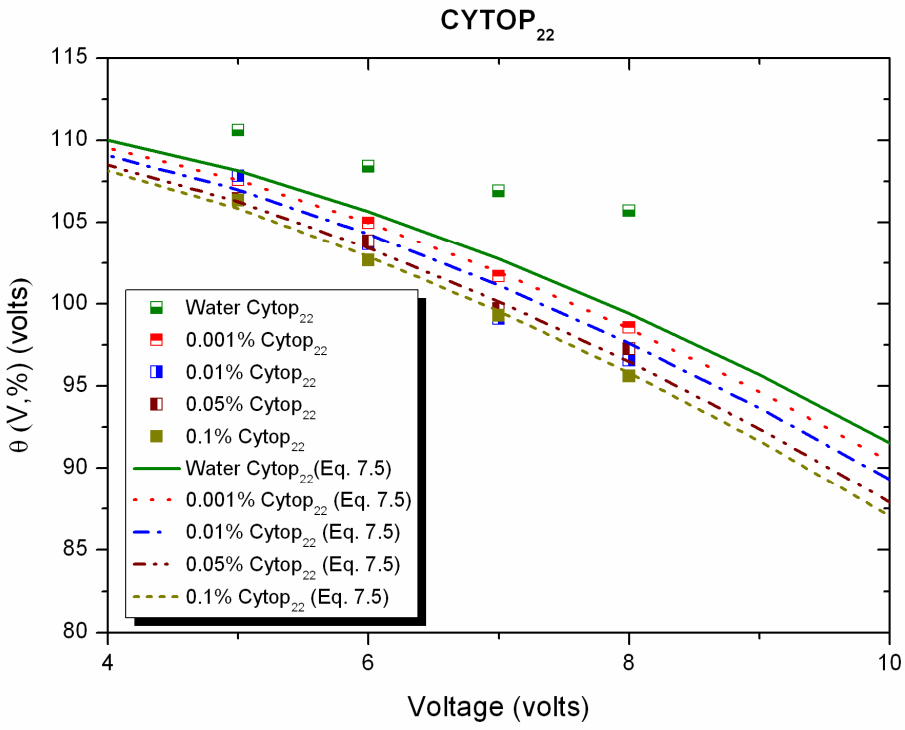
CYTOP22
θ (V,%) (volts)
Voltage (volts)
Water Cytop22
0.001% Cytop22
0.01% Cytop22
0.05% Cytop22
0.1% Cytop22
Water Cytop22(Eq. 7.5)
0.001% Cytop22 (Eq. 7.5)
0.01% Cytop22 (Eq. 7.5)
0.05% Cytop22 (Eq. 7.5)
0.1% Cytop22 (Eq. 7.5)

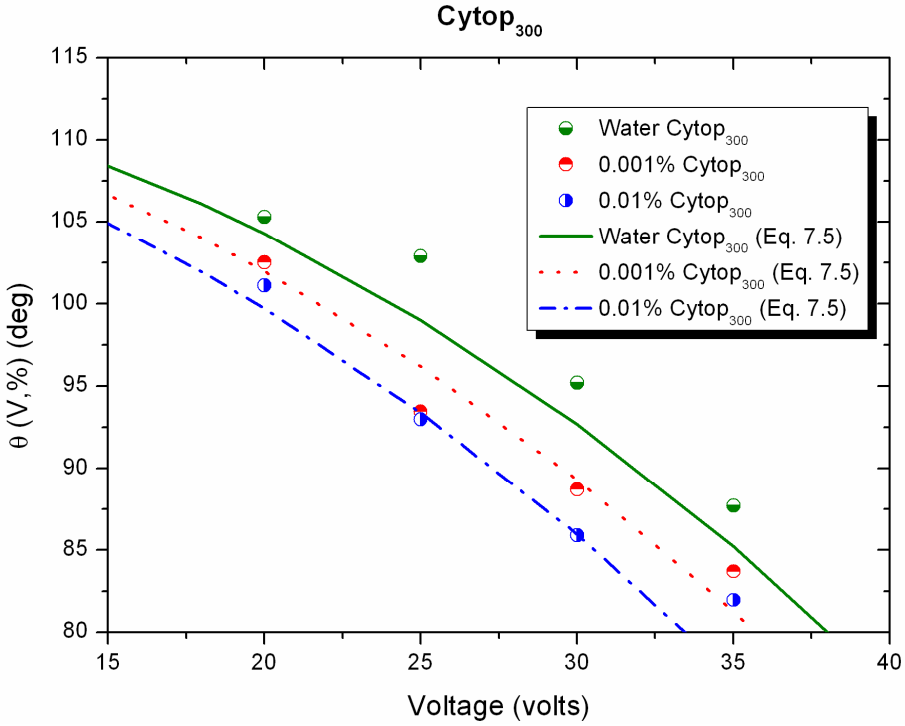
Cytop300
θ (V,%) (deg)
Voltage (volts)
Water Cytop300
0.001% Cytop300
0.01% Cytop300
Water Cytop300 (Eq. 7.5)
0.001% Cytop300 (Eq. 7.5)
0.01% Cytop300 (Eq. 7.5)

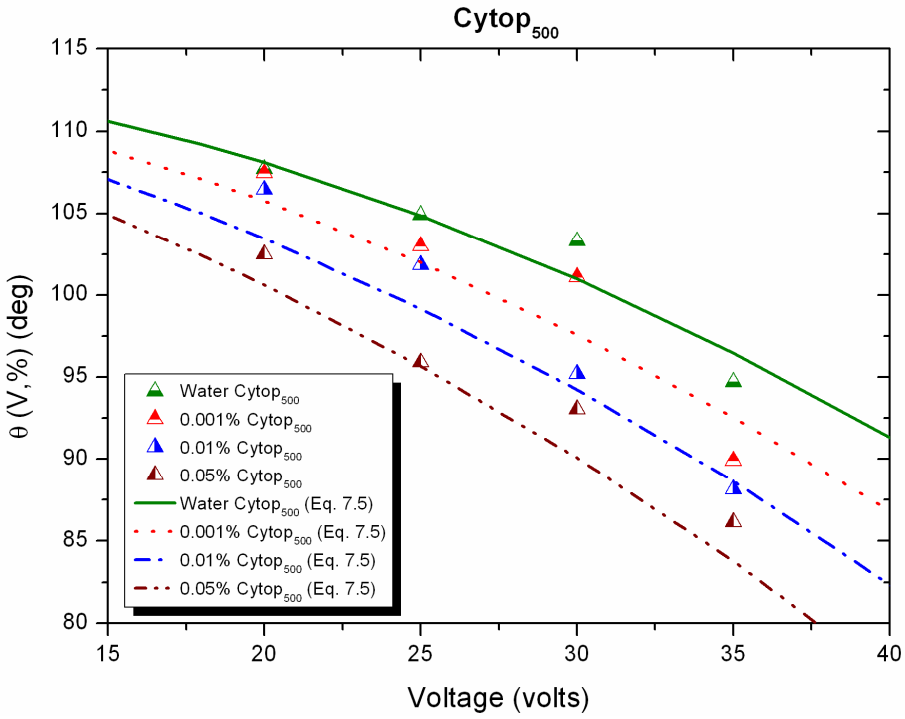

Figure 7. 5 – Electrowetting contact angle, $\theta(V,\%)$ (degs), versus voltage, V (volts), for 0.1% (filled), 0.05% (filled-left), 0.01% (filled-right), 0.001% (filled-up) TiO_2-water nanofluid and for the pure water case (filled-down) on $Cytop_{22}$ (squares), $Cytop_{300}$ (circles) and $Cytop_{500}$ (triangles).

The agreement between theory, Equation 7.5, and experimental results on all three substrates is satisfactory. The results presented for the three different aFP dielectric thicknesses reinforce our conjectures and definitely offers a plausible explanation to how the presence of nanoparticles coupled with electrowetting modify further the thermodynamic equilibrium and therefore the electrowetting behaviour. Nanoparticles under an external electric field applied will modify further the interface solid-liquid due to the additional interaction between this particles and the dielectric substrate. The analogy between adsorption of molecules at the solid-liquid interface due to pressure gradients presented by Gibbs and Ward et al., and the adsorption of nanoparticles at the solid-liquid interface triggered by voltage agrees adequately. This latter opens a new understanding of electrowetting performance of colloidal suspensions or ionic liquids.

Additionally, when studying the dynamics of the electrowetting/dewetting of the contact line into detail, Figure 7. 3, a relationship between both spreading and relaxation movement of the TCL in time can be established depending on the aFP thickness. The electrowetting set up described during Section 3.1.2 allows for the discharge of the dielectric layer, when switching Off voltage, since one of the electrodes is grounded. From basic principles of electricity, the build-up of charge, or the discharge of a capacitor (the dielectric substrate) will depend on both permittivities and thicknesses of the dielectric layers. The fundamentals of capacitor discharge relay on how quick the charges will leave the system meaning how strong the interactions between electric charges and the molecules present at the solid-liquid interface will be after switching Off the voltage.

According to Figure 7. 3, the thicker the dielectric the faster the capacitor charges and discharges, thus the faster the advancing and receding movement of the contact line since molecules and charges present in the dielectric layer do not interact as vigorously as it happens when they are closer, i.e. thin aFP. From the same figure, an exponential receding of the contact radius is observed when switching voltage Off, then applying basic electrical principles, the receding movement of the contact line approximates fairly well to the behaviour of exponential decay of voltage in a capacitor, Equation 7.6:

$$V(t) = V_0 \cdot e^{\frac{-t}{R'C}} \qquad (7.6),$$

where $V(t)$ is the voltage discharge versus time that depends on the initial voltage, V_0, and on the properties of the dielectric layers: resistance, R', and capacitance, C. It is well know that the capacitance of a substrate increases when decreasing the thickness of this latter whereas resistance decreases proportionally when thickness does. Due to this contrary effect of the product $R'C$ when decreasing thickness of the aFP, we might consider $R'C$ as the relaxation time named τ.

Since EWOD substrates behave as capacitors, it is foreseen that the interactions between charges at the dielectric and the liquid molecules, at the liquid-solid interface, will depend on how long the capacitor takes to charge and this charge. This suggests that contact line radius will behave in a similar fashion as the discharge of a capacitor, then, based on Equation 7.6, the dynamics of receding of the contact radius can be rewritten as:

$$R(t) = R_0 + (R_{EW} - R_0) \cdot e^{\frac{-t}{\tau}} \qquad (7.7).$$

Where $R(t)$ is the contact line radius receding in time, t, R_0 is the initial contact radius and R_{EW} is the contact radius under an applied voltage. Then from the experimental values presented in Figure 7. 3 (c) and the fitting of Equation 7.7, an empirical value of τ can be calculated and used to represent theoretical trends on all three substrates as shown in Figure 7. 6:

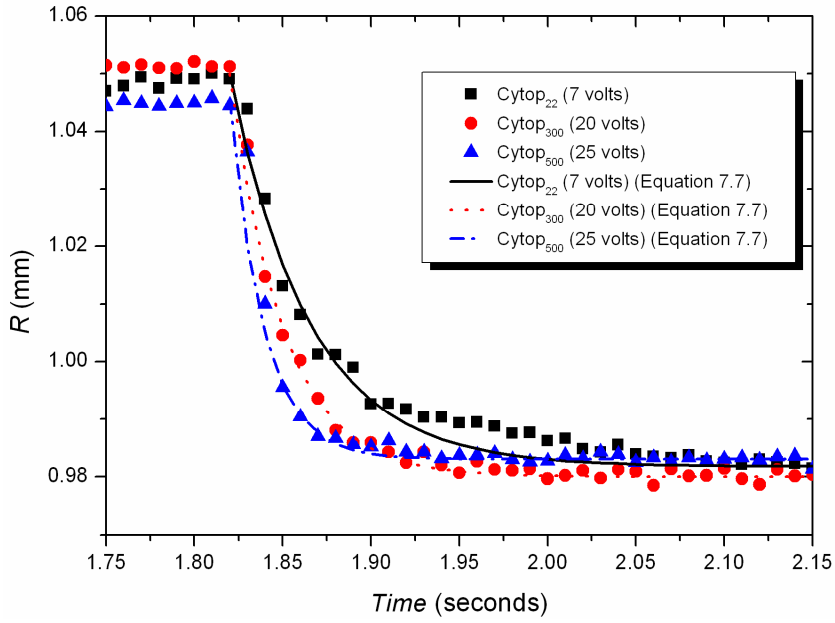

Figure 7. 6 - Average of 7 profiles of the contact radius, R (mm), versus time, t (seconds), for 0.01% TiO_2-water during the receding movement of the contact line at different voltages, (volts), on $Cytop_{22}$ (squares), $Cytop_{300}$ (circles) and $Cytop_{500}$ (up-triangles) besides theoretical trends calculated using Equation 7.7.

Looking at Figure 7. 6, theoretical trends calculated using Equation 7.7 match fairly well with experimental results on $Cytop_{300}$ and $Cytop_{500}$, whereas on $Cytop_{22}$ theoretical trend slightly deviates from experimental behaviour. The relaxation of the contact line is definitely quicker for the thickest of the aFP dielectrics and slower for the thinnest one. From the atypical behaviour observed on $Cytop_{22}$, Figure 7. 6, it seems that the thinner the aFP, the stronger the interactions between fluid molecules and charges present in the conductive dielectric layer. This offers a plausible explanation of the differences in behaviour found for the different dielectrics. Then the study of the contact line dynamics on thin dielectrics requires further research and can help to reveal further the interactions between fluid molecules and charges present in the conductive dielectric.

Of equal importance is the electrowetting movement of the contact line when a voltage is applied. From the findings stated above, it is clear that aFP thickness plays an important role on the dynamics of the contact line, Figure 7. 3. On both $Cytop_{300}$

and $Cytop_{500}$ the advancing movement of the contact line, i.e. charge of a capacitor, is almost instantaneously taking ca. 0.02 seconds to reach the final electrowetting contact radius. Saphiro et al. [155] estimated the charging time of a capacitor for a slightly resistive liquid and a high resistive solid as:

$$\tau = \frac{\varepsilon_s R^2 / t}{R^2 / \rho_s h + R / \rho_l} \qquad (7.8),$$

where ε_s is the permittivity of the solid, R the radius of the droplet, h the thickness of the dielectric, and ρ_s and ρ_l are the resitivities of substrate and liquid respectively. Substituting typical values for our specific system, an approximate charging time of ca. 0.001 seconds is proposed, one order of magnitude smaller than the electrowetting time obtained in this experimental research. Although experimental analysis may lead to experimental errors, it is worth noting the good agreement of Equation 7.8, which reports smaller relaxation times when increasing the thickness of the aFP. This latter is consistent with experimental results presented in Figure 7. 6.

7.5 Summary

The behaviour of TiO_2-water nanofluids under electrowetting conditions has been studied. It was found that nanofluids can be manipulated in a similar fashion as deionized water following the Young-Lippmann equation. Moreover an enhancement in electrowettability is observed when adding nanoparticles to the base fluid and this latter is dependent on concentration. This enhancement in spreading of the contact line is interpreted in terms of adsorption of nanoparticles at the solid-liquid interface coupled with voltage. There is a local decrease in the solid-liquid interface when a difference of voltage is applied to these nanofluids. An additional term has been

added to the Young-Lippmann equation to account for the excess of energy due to the addition of nanoparticles coupled with electrowetting. A correlation based on experimental results has been proposed to predict the change in droplet shape.

On other hand, the dynamics of spreading/receding of the contact line under an applied voltage have been addressed too. This latter is of great importance for the development of quick and reliable switching between electrowetting and no electrowetting conditions for optical and microfluidic applications. An instantaneous response of the contact line was observed for the thickest of aFP, reaching the electrowetting contact angle in approximately 0.02 seconds, whereas a smoother movement of the contact line was reported for the thinnest of the aFP coatings: $Cytop_{22}$, which is consistent on both spreading and receding of the contact radius. It is worth noting that an exhaustive study of aFP thickness versus relaxation time must be addressed since smaller thicknesses lead to important energy savings but delays both advancing and receding movement of the contact line with the consequent anomalous behaviour. A balance between relaxation time and voltage applied must be carried out.

The last chapter includes the differences between the evaporative behaviour for different TiO_2-water nanofluid concentrations under DC external voltage applied and under *free* evaporation. A thorough analysis of the most plausible mechanism for the absence of “stick-slip” behaviour and for the more homogeneous deposits observed, is included.

Chapter 8: Nanofluid Evaporation under Applied DC Electric Field

Colloidal suspensions have been under an intensive research in the past decades specially since the work of Deegan et al. and the well-known coffee ring stain [28]. Typically, the evaporative behaviour of these suspensions are different from the base fluid since particles are carried from the bulk of the fluid towards the edge, and deposits are left behind after the complete dry-out. Particularly, on the case of nanofluids, stick-slip behaviour and rings stain deposits are reported as explained in Section 2.3 [58, 106, 141]. Therefore, revealing the interactions particle-particle, particle-fluid and particle-substrate can help to shed light on the manipulation and control of the deposits left from colloidal suspensions for biological [22], industrial, analytical [95] or patterning purposes [159, 160]. It has been demonstrated that the self-assembly of nanoparticles can be controlled by changing the pH of the evaporating solution [38] or changing the shape of the particles suspended leading to the suppression of the coffee ring effect [56]. More recently the suppression of the coffee ring stain has been successfully reported under an applied AC electric field, due to the internal flows generated within the droplet attributed to the continuous movement of the contact line keeping particles in suspension [109]. It may be predictable that the internal particle flows emerging in the bulk of a droplet when applying a DC electric field will differ from those proposed for AC [68, 161]. In what follows the different evaporative behaviour and patterns found after the complete dry-out of different TiO_2-water nanofluid concentrations when DC is applied to a droplet are compared to those during free evaporation and to the pure fluid case. A smooth and continuous receding of the contact line compared to "stick-slip" behaviour reported for nanofluids under free evaporation besides the more regular and homogeneous patterns in contrast to rings stains are presented and discussed next.

8.1 Evaporative Behaviour and Deposits

Results concerning the evaporative behaviour of TiO_2-water nanofluids subjected to an electric voltage during the complete dry-out are presented in Figure 8. 1. The

observed droplet profile with an electrode immersed for both EW (Figure 8. 1 (a)) and no EW (Figure 8. 1 (b)) conditions at different drying times: $t = 0$, $t = 1/4\,t_{evap}$, $t = 2/4\,t_{evap}$ and $t = 3/4\,t_{evap}$ are represented. Base line and Circle Fitting Fit are included.

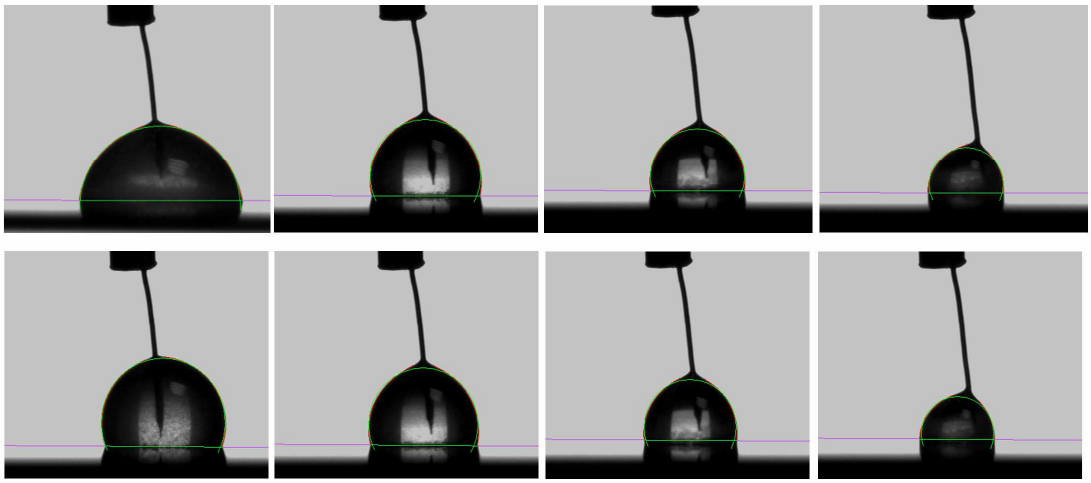

Figure 8. 1 – Substrate, droplet and electrode immersed into a 0.05% TiO_2-water nanofluid droplet under (a) EW conditions and (b) no EW for $t = 0$, $t = 1/4\,t_{evap}$, $t = 2/4\,t_{evap}$ and $t = 3/4\,t_{evap}$. Base line and Circle Fitting Fit are included.

Both evaporative behaviours of TiO_2-water nanofluid at different concentrations under EW and no EW conditions were analyzed and are presented below. In the case of no applied voltage, the electrode was immersed into the droplet in order to ensure similar experimental geometric conditions throughout evaporation. Base radius, R (mm), height of the droplet, h_0 (mm), and contact angle, θ (deg), versus time, t (seconds), besides images of the corresponding deposits after the complete dry-out for 0.1%, 0.05%, 0.025% and 0.01% of TiO_2-water are included in: Figure 8. 2, Figure 8. 3, Figure 8. 4 and Figure 8. 5. To allow comparison with the pure fluid case, the evolution of the base radius for deionized water under EW and no EW conditions is also included.

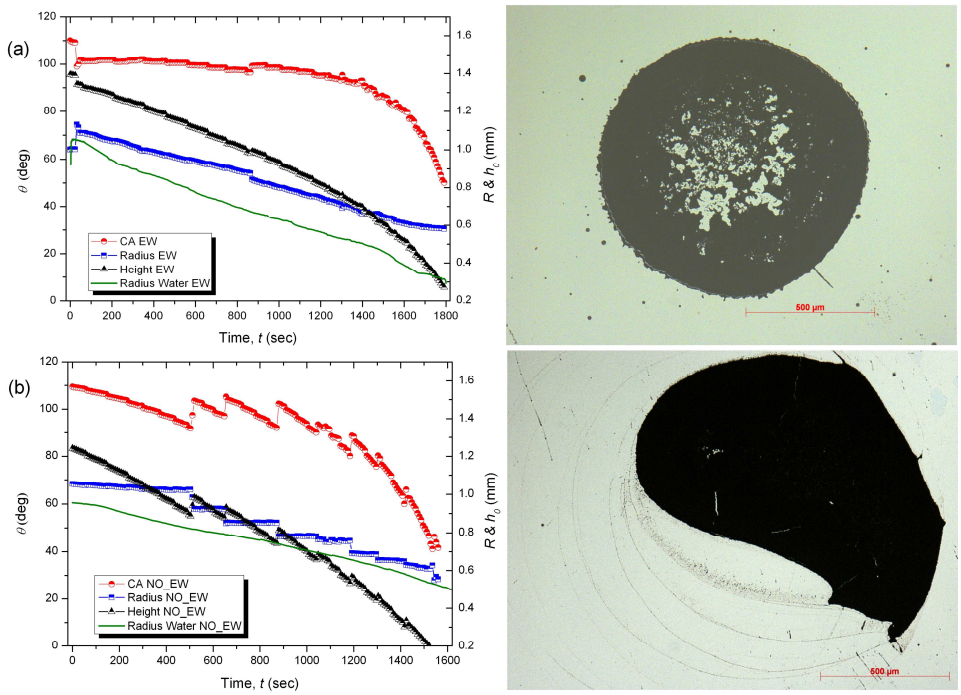

Figure 8. 2 - Evolution of the contact radius, R (mm) (squares), contact angle, θ (deg) (circles), and height of the droplet, h_0 (mm) (up-triangles), with time, t (seconds); (a) under electrowetting conditions and (b) under free evaporation for: 0.1%. Corresponding deposits also included.

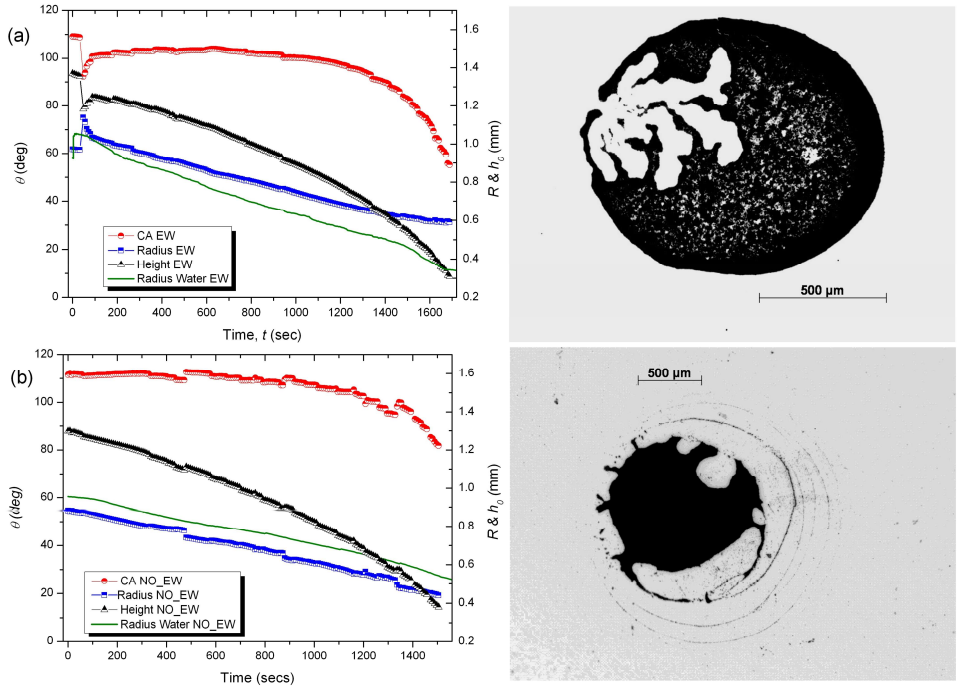

Figure 8. 3 – As for Figure 8. 2, but for 0.05% TiO_2-water nanofluid.

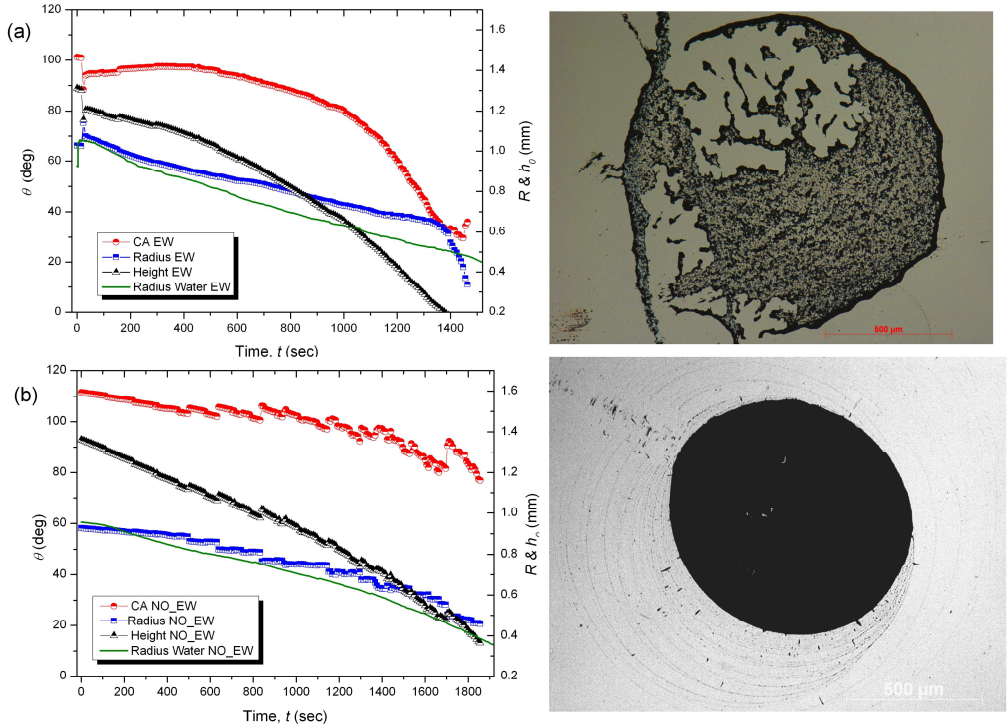

Figure 8. 4 – As for Figure 8. 2, but for 0.025% TiO_2-water nanofluid.

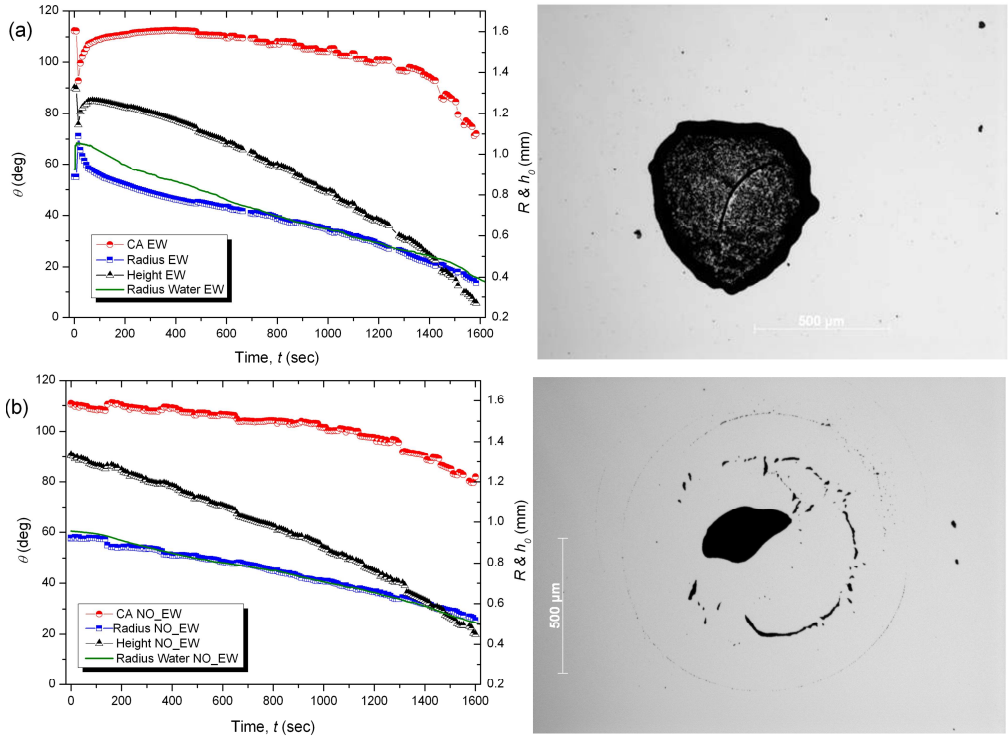

Figure 8. 5 – As for Figure 8. 2, but for 0.01% TiO_2-water nanofluid.

According to the figures presented above and as reported during Section 2.3, the *free* evaporation of nanofluid droplets with or without an electrode immersed into a droplet leads to "stick-slip" behaviour, where jumps of the contact line with the correlated changes in contact angle are observed [58, 106, 141]. Pictures of deposits are in agreement with rings-like stain reported previously [97, 106]. It is worth noting that although the number of steps and the magnitudes of the jumps decrease when an electrode is immersed into a nanofluid droplet, "stick-slip" behaviour is still clearly noticeable.

On the other hand, when a voltage is applied to a droplet, there is a quick reduction in both contact angle and droplet height, and a swift increase in the base radius as it can be extracted from the figures above: Figure 8. 2 (a), Figure 8. 3 (a), Figure 8. 4 (a) and Figure 8. 5 (a). Thereafter the droplet shape evolves; contact line recedes monotonically following the same behaviour of pure water on hydrophobic substrates (see Chapter 4) whereas contact angle shows a constant value for at least 70% of the droplet lifetime. The most important feature during evaporation under EW conditions is the absence of jumps or discontinuities on the variables that represent the droplet profile evolution. Of great importance is the continuous receding of the contact line and the more attractive and homogeneous deposits with the absence of rings observed. Also bigger stains are evident for greater concentrations.

As an approximation and supported by the figures of the deposits presented, it is likely that nanoparticles present in the bulk of the droplet might be attracted by the substrate under an external electric field applied. Evaporative behaviour and deposits presented for TiO_2-water nanofluids, suggest a net negative charge of these particles in suspension since the grounded electrode, i.e. the substrate, is charged positively as described in Chapter 3.

In order to be able to explain the deposits presented and the suppression of the "stick-slip" behaviour, a comparison between the forces attracting the particles towards the substrate and capillary flow of particles towards the contact line to replenish the liquid evaporated is proposed.

8.2 Electrophoresis versus Evaporation

Considering an isolated nanoparticle in the bulk of a droplet, under *free* evaporation capillary flows drive the particle towards the contact line following the features predicted by Deegan et al. [28, 102]. On the other hand, under an applied electric field another force comes into play: electrophoresis (EP), which was observed more than two centuries ago to explain the motion of clay particles in suspension under an electric field [130]. More recently other authors have used EP for controlling the deposition of colloidal particles [162, 163]. Then an analysis of the timescales of the two main particle motions present within a droplet under an applied electric field is carried out. Figure 8. 6 shows the different forces acting on an isolated nanoparticle.

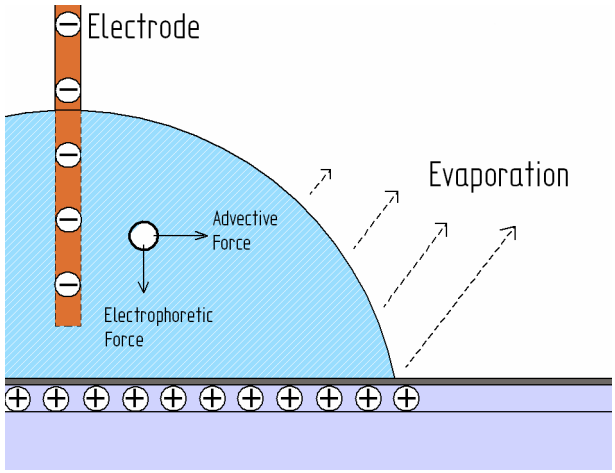

Figure 8. 6 – Sketch of the different forces present during evaporation and under an electric field applied.

8.2.1 Advective Flow

The accumulation of particles at the TCL following the evaporation of colloidal suspensions under marked evaporation and pinning of the contact line was predicted and mathematically demonstrated more than a decade ago, Equation 8.1 [14, 102, 164]:

$$\rho \frac{\partial h}{\partial t} = -\rho \frac{1}{r} \frac{\partial}{\partial r}(rhv_{adv}) - J_s(r,t)\sqrt{1+\left(\partial h / \partial r\right)^2} \qquad (8.1).$$

Equation 8.1 explains the averaged radial outward flow inside the droplet, v_{adv}, for initially pinned contact lines. This equation considers the continuity of the fluid evaporated at the contact line arising from the vertical flow generated as the local height of the droplet, $h(r)$, falls in time, t. ρ and J_s are liquid density and evaporative mass flux at the droplet centre respectively. Since we are interested on the region close to the droplet centre, the evaporative mass flux at the top of the droplet can be approximated to the evaporative flux of a flat meniscus, i.e. $J_s \approx J_0$ and equal to $1.7x10^{-5}$ Kg·m^2/s (obtained by additional experiments) where $\partial h/\partial r \approx 0$. Droplet height at the centre, h_0, can be extracted from Figure 8. 2 (a), Figure 8. 3 (a), Figure 8. 4 (a) and Figure 8. 5 (a), and approximated as a constant, i.e. $\partial h_0/\partial t \approx -K$. Then Equation 8.1 can be simplified and written as:

$$v_{adv}(r) \approx \frac{r}{2h}\left(K - \frac{J_0}{\rho}\right) \qquad (8.2).$$

From the evaporative behaviour, values of contact radius, R, K and h as $h(r) = (R-r)\tan\theta$, at the beginning of the evaporative process can be extracted and substituted in Equation 8.2. Then in the vicinity of the triple contact line $(r \sim R)$, $(h \sim (1-r)\cdot\tan(100\,°)$ mm) and $K = 6\cdot10^{-4}$ mm/s, an average radial advective liquid or particle speed can be obtained as approximately $v_{adv} \sim 3$ µm/s. This advective velocity is in agreement with experimental radial particle velocity found by Marin et al. at the vicinity of the contact line during the last period of evaporation where particle velocity folds [98]. It is worth mentioning that Equation 8.2 does not describe the vertical flow at $r = 0$ but gives an approximation of the advective flow near the droplet centre.

In order to validate this model built for pinned contact lines, a comparison between the outward flow velocity and the receding velocity of the contact line is carried out. From Figure 8. 2 (a), Figure 8. 3 (a), Figure 8. 4 (a) and Figure 8. 5 (a), the receding movement of the contact line can be approximated as $v_{CL} = \partial R/\partial t \approx 0.3$ µm/s. Then the ratio particle velocity to contact line movement can be calculated as follows: $v_{adv}/v_{CL} = 3/0.3 \approx 10$. Receding movement of the contact line is at least one order of magnitude shorter than particle velocity, hence a quasi-stationary movement of the can be considered, and Equation 8.1 can be used for our purpose.

8.2.2 Electrophoresis

During evaporation and due to the characteristic features of nanofluids, any vertical movement of the particles can be negligible unless these latter are in suspension and under the presence of an electric field, i.e. case of evaporation under EW conditions. The electric field present inside the droplet is given by $E = -\partial V/\partial y \approx V/h_0$ where V is the difference of voltage applied to the droplet and h_0 the droplet height. Nanoparticles used in this experimental research possess negative net surface charge, i.e. negative zeta-potential as electrophoretic mobility measurements included in Table 3. 2 show. Then under an applied electric field, E , nanoparticles will be attracted by the electrode with opposite charge, the substrate, with a force equal to $F \downarrow = qE$, where q is the charge of the particle. However, a Stokes-type viscous force will oppose to this movement, $F \uparrow = 6\pi\eta a v_{ep}$, where v_{ep} is the electrophoretic velocity of the particles towards the substrate, a is the particle radius and η the liquid viscosity. Balancing these forces, an expression of the electrophoretic velocity is obtained:

$$v_{ep} \approx \frac{qV}{6\pi h \eta a} \qquad (8.3).$$

Typically, the net surface charge for a spherical particle can be expressed as [165, 166]:

$$\zeta = \frac{q}{4\pi\varepsilon_r\varepsilon_0 a} - \frac{q}{4\pi\varepsilon_r\varepsilon_0\left(a+\frac{1}{k}\right)} \rightarrow \zeta = \frac{q}{4\pi\varepsilon_r\varepsilon_0 a(ka+1)} \qquad (8.4).$$

And considering $ka < 1$, the effective charge, q, can be written as:

$$q = 4\pi a\varepsilon_r\varepsilon_0\zeta \qquad (8.5).$$

If we now combine Equation 8.3 and Equation 8.5, the well known Hückel equation, Equation 8.6, can be demonstrated and electrophoretic velocity calculated as [165, 167]:

$$v_{ep} = \frac{2}{3}\frac{\varepsilon_r\varepsilon_0}{\eta}\zeta\frac{V}{h} \qquad (8.6).$$

Substituting the different data: $\varepsilon_{H_2O} = 80$, $\varepsilon_0 = 8.85\cdot10^{-12}$ F/m, $\eta_{H_2O} = 1$ cp, $V = 18$ V, $h = 0.0014$ m and ζ with an approximate value of 20 mV taken from literature [168, 169], an electrophoretic speed greater than 100 µm/s is reported. It is worth mentioning that the electrophoretic speed calculated above is in agreement with electrophoresis experiments carried out by Lee et al. using the same system, TiO_2 nanoparticles and deionized water [132].

To support the electrophoretic velocity calculated above using assumptions and values from literature, additional experiments of electrophoretic mobility, μ_{ep}, for

the different nanofluid concentrations tested were carried out and included in Table 3. 2. The next equation, Equation 8.7, is an association between electrophoretic mobility and electrophoretic velocity:

$$v_{ep} = \mu_{ep} \cdot E = \mu_{ep} \cdot V/h \qquad (8.7).$$

Using the values obtained by experimental means, Table 3.2, for an $\mu_{ep} = 1.6$ (μm/s)(V/cm)$^{-1}$ under 18 V applied and a distance between electrodes $h = 1.4$ cm, an v_{ep} ca. 200 μm/s is calculated, which is in the same order of magnitude with the above calculated values.

To summarize these calculations, electrophoretic velocity of the particles towards the electrode with opposite charge ($v_{ep} \sim 100$ μm/s) is at least one order of magnitude greater than the advective motion of particles towards the contact line ($v_{adv} \sim 10$ μm/s) [98, 160].

8.2.3 Comparison Between the Two Motions

Although the preferential motion of TiO_2 nanoparticles to migrate towards the substrate instead of being swept towards the contact line has been numerically demonstrated, a comparison between the two main timescales, advective and electrophoretic is required. Ratio, $\overline{R}$, shows this comparison as Equation 8.8:

$$\overline{R} = \frac{t_{adv}}{t_{ep}} \approx \frac{v_{ep}}{v_{adv}} \frac{d_{adv}}{d_{ep}} \approx \frac{v_{ep}}{v_{adv}} \frac{1}{1.4} \approx \frac{qV}{4.2\pi\eta a r \dot{h}} = \frac{4}{4.2} \frac{\varepsilon_r \varepsilon_0 \zeta V}{\eta r \dot{h}} \approx \frac{\varepsilon_r \varepsilon_0}{\eta r \dot{h}} \zeta V \qquad (8.8).$$

Equation 8.8 shows that for large $\overline{R}$; particles takes longer to reach the vicinity of the contact line than the substrate. In this case, electrophoretic motion of the particle will be preferential leading to more homogenous deposits with the absence of rings stains, pictures of deposits in Figure 8. 2 (a), Figure 8. 3 (a), Figure 8. 4 (a) and Figure 8. 5 (a). If we now substitute reasonable values in Equation 8.9, obtained either experimentally of from literature, for a 3 µl water droplet, unless $K \sim \partial h_0 / \partial t$ is close to 10^{-4} m/s ~ 0.1 mm/s, electrophoretic motion will be preferential to advective one.

With this comparison we may conclude that electrokinetic motion net surface charged particles suspended in a low viscous liquid under an strong applied electric field will be preferential to advective one. This semi-quantitative analysis suggests a plausible explanation of the more homogeneous deposits observed under EW conditions compared to the rings stain deposits found under *free* evaporation. Sedimentation phenomenon (electrophoresis) results preferential to the motion of nanoparticles towards the TCL (advective) for the different nanofluid concentrations tested. Particles are attracted towards the substrate hindering the build-up of artificial defects at the TCL, thus preventing the "stick-slip" motion, at least to some extent. Particle speed, migration distance and characteristic time due to electrophoretic effect, advective flow and the motion of the contact line are presented in Table 8. 1:

Table 8. 1 - Electrophoretic, v_{ep}, advective, v_{adv}, and contact line, v_{CL}, speeds (μm/s), particle migration distance (m), and characteristic time, t_c (seconds), are included.

	EP Effect	**Advective Effect**	**CL Motion**
Speed (μm/s)	~100.0	~10.0	~0.3
Migration Distance (mm)	1.4	1.0	0.6
Characteristic Time (s)	10	100	2000

Table 8. 1 shows the more relevant data gathered during this experimental research, clearly showing one order of magnitude of difference between the different timescales proposed. The preferential electrophoretic motion over the advective one obtained by additional calculations is supported by the suppression of "stick-slip" behaviour observed experimentally since fewer nanoparticles tend to reach the contact line and a smooth/continuous receding of the contact line is visible.

Although either minimum irregularities on the surface or the small addition of nanoparticles, i.e. 0.001% TiO_2-water (Chapter 4), can prompt the pinning of the contact line, this suggests that for high concentrations the suppression of the "stick-slip" behaviour might not be complete. Indeed a small jump is noticed for the highest of the concentrations, Figure 8. 2 (a). The author would like to point out that the suppression of "stick-slip" performance is a combination of both electrophoretic effect and the hydrophilicity of the wire presented in Figure 8. 1.

Commenting on the deposits found, a typical set of rings corresponding to "stick-slip" behaviour is found on the case of *free* evaporation. Nanoparticles are accumulated at the TCL inducing the pinning of these latter. From the evaporative behaviour shown in Figure 8. 2 (b), Figure 8. 3 (b), Figure 8. 4 (b) and Figure 8. 5 (b), a slight drift of the contact line is noticed due to the presence of the wire that pulls the contact line upwards. Due to both evaporation and the pinning of the contact line, the internal energy of the droplet increases until this energy is high

enough for the jump to ensue, at this point particles are left behind on the substrate leading to rings stain as explained in Chapter 5 [97].

On the opposite case, under EW conditions, a more homogeneous single pattern where particles are accumulated mainly at the centre and not at the edge is observed. The suppression of the rings stain reported for TiO_2-water nanofluids is evident. Results do not show the complete suppression of the coffee ring stain by accumulation of particles at the centre as reported by other authors [66, 109] but it does prevent the accumulation of particles at the contact line, which is a way of controlling the deposits of colloidal particles in suspension under an applied electric field. As further investigations the author would like to suggest the study of the evaporative behaviour of for different nanofluids, cells, bacteria under EW conditions and the analysis of this effect on particle structuring [150, 160].

Another aim of this research was to compare, if possible, the internal flows due to under AC electric field [66, 68] to those under DC electric field. It is then demonstrated that, electrophoresis is the main mechanism governing the internal flow of particles within an evaporating droplet under a DC electric field.

8.2.4 Additional Considerations

We would like to address the case in which particles in suspension will posses a zero net surface charge. Then due to the heterogeneity features of the electric field (droplet shape), particles in the bulk of the droplet will move following dielectrophoresis (DEP) [170]. Due to the different dielectric properties between fluid and nanoparticles, the existence of a non-homogeneous electric field will induce a dipole in the particles inducing DEP motion [171]. Values calculated were in the order of nanometers per second.

Thus, from the more homogeneous patterns and the additional electrophoretic mobility measurements, we conclude that electrophoresis is the mechanism governing the motion of TiO_2 nanoparticles in a non-viscous fluid under an applied electric field.

8.3 Summary

Electrophoresis is proposed and demonstrated, for the first time, as the mechanism governing the motion of TiO_2 nanoparticles present in the bulk of a droplet under an applied DC electric field during evaporation. A shorter timescale for the nanoparticles to reach the substrate has been reported, when compared to outward capillary flows that swipe the particles towards the contact line following advection. Due to fewer particles deposit at the triple contact line, during EW no pinning of the contact line is attained and a monotonic receding of the contact line during almost the complete evaporation is observed. This technique represents potential applications for the manipulation of colloidal suspensions and pattern formation, leading to more homogeneous and a single ring pattern in contrast to the multiple rings observed during the evaporation of TiO_2-water nanofluids. EP is proposed to control nanofluid deposits without manipulating continuously the dynamics of the contact line.

Experiments could be extended to cells, bacteria or proteins due to similar surface charge present when compared to TiO_2 nanoparticles in suspension. The negative net surface charge of the nanoparticles can be demonstrated in plain sight *only* attending to the deposits formed.

Once presented the main results, discussions and conclusions dragged from this experimental research, the main overall conclusions and what could be subsequently done is included next.

Chapter 9: Conclusions and Further Work

In this work, a study on the dynamics of the contact line and the mechanisms present during wetting, evaporation and electrowetting, of fluids and nanoparticle laden fluids, has been conducted. Different techniques, tools, approaches and methods, have been explored pursuing to uncover the interplay particle-particle, particle-solid, particle-liquid, liquid-solid and liquid-gas at the macro-, micro- and nanoscale. The main findings revealed during this experimental research, aiming to shed further light on the fundamental physics, chemistry and engineering present during these non equilibrium phenomena, are included next.

9.1 Wetting and Dynamics of the Contact Line throughout Evaporation

The evaporative behaviour of pure fluids on real, smooth, solid substrates varying in hydrophobicity, has been investigated at the macroscale. Different evaporative modes have been identified and a simple force balance at the triple contact line has been proposed to seize the droplet intrinsic energy barrier required for the depinning of the contact line during evaporation. Applying an energy-minimization approach at the triple contact line, a threshold for the force required for the depinning of the contact line is set at 0.02 N/m. The effect of hydrophobicity on the depinning of the contact line is evident, favoured by high initial contact angle.

The intrinsic energy barrier observed for pure fluids on hydrophilic substrates, for example water on Silicon, is increased further by the addition of small amount of nanoparticles to the base fluid. The complete pinning of the contact line is reported for concentrations as small as 0.001% TiO_2-water by weight. On the other hand, on hydrophobic substrates, TiO_2-water nanofluid concentrations ranging from 0.001% to 0.1% “stick-slip” behaviour is reported. In addition, a clear increase in the magnitude of the jumps of the contact line besides greater changes in contact angle are visible when increasing nanoparticle concentration since there are larger quantities of nanoparticles accumulating at the triple contact line and thus hindering

further the receding movement of the latter. It is worth noting that the concentration of Al_2O_3–water nanofluid required for a similar "stick-slip" behaviour to that found for TiO_2-water is ten-fold smaller, suggesting that Al_2O_3 nanoparticles interactions with the substrate or between the same nanoparticles are, somehow, stronger than those of TiO_2. The excess of droplet free energy before the jump has been seized and compared for the different nanofluids using experimental data and theoretical expressions from literature. The dependence of contact line dynamics on concentration and type of nanoparticle is evident.

To fully understand the evaporative behaviour of fluids laden with nanoparticles and the structuring of these particles following evaporation, an analysis of the deposits left after the complete dry-out at the nanoscale becomes vital. Height, width and profile of the ring-stain deposit following *free* evaporation of TiO_2-ethanol nanofluid were successfully imaged for the first time using AFM. Using the experimental data of the droplet profile gathered at the macroscale, a deposition theory to explain the accumulation of nanoparticles at the triple contact line was developed. The agreement between deposition theory presented and the profile of the deposits imaged by AFM is evident. Thus a plausible theoretical description of the structuring of TiO_2 nanoparticles following evaporation is presented.

The dynamics of the contact line of Al_2O_3-water nanofluid and pure fluid on rough rather than smooth substrates for different kinetics of evaporation have been also investigated. Heterogeneities present on the aluminium tested are great enough to attain the complete pinning of the contact line for both nanofluid and pure fluid, i.e. intrinsic energy barrier exerted by irregularities on the surface overcomes the depinning force required for the contact line to recede, for both fluids. No appreciable differences in droplet lifetime between evaporation of Al_2O_3-water nanofluid or the pure fluid case are observed since pinning contact lines ensures the same evaporative mode. Reducing the pressure of the system also increases the evaporation rate and a power relationship between rate of evaporation per unit length and pressure is presented, which can be used to predict droplet lifetime on rough substrates for any water based fluid at different sub-atmospheric pressures.

9.2 Electrowetting

The ability of manipulating droplet interfaces without requiring mechanical parts has received important attention in the past decade. In this experimental research, we focus on the control of the droplet interface and the mechanisms present during evaporation under an external force applied. Different approaches are examined to try to uncover some of the mechanisms, fundamental physics, and interactions particle-particle, particle-liquid, particle-substrate, liquid-substrate, or liquid-gas, present under an external voltage applied.

Preliminary studies revealed that nanofluid droplets can be manipulated in a similar way as deionized water following the features predicted by Gabriel Lippmann more than one century ago. However, for a same voltage applied, an enhancement in electrowetting behaviour when adding TiO_2 nanoparticles when compared to the base fluid was observed. In addition, greater changes in droplet interface were observed when increasing nanoparticle concentration. An accumulation of nanoparticles near the triple contact line that lowers locally the interfacial tension solid-liquid with the consequent increase in the extent of spreading is reported. A modified Young-Lippmann equation to account for the decrease in solid-liquid surface tension of the dielectric layer due to the presence of nanoparticles and triggered by voltage at the solid-liquid interface has been developed.

The dynamics of spreading/receding of the contact line, i.e. voltage On/Off, on substrates varying in thickness of the amorphous fluoropolymer covering the dielectric electrode have also been investigated. A quick and reliable advancing/receding movement of the contact line under electrowetting and non-electrowetting conditions is of great importance for the fabrication of quick and stable electro-optic switches. A quicker receding movement of the contact line is reported when increasing the thickness of the aFP layer, although greater voltages are required for a same observable change in droplet shape. The thinner the aFP layer covering the electrode the greater the interactions between nanoparticles, water molecules and the dielectric electrode at the solid-liquid interface. An analogy

between the receding movement of contact line after switching Off the voltage and the exponential decay observed when discharging capacitors approximates fairly well.

The last part of this experimental research consisted in uncovering the mechanisms present during the evaporation of TiO_2-water nanofluids droplets under direct current (DC) voltage applied. Following the complete dry-out of these nanofluids, different nanoparticle patterns when compared to those reported under *free* evaporation were observed. Deposits that are more homogeneous (no rings observed) and the absence of "stick-slip" behaviour of the contact line suggests the preferential motion of nanoparticles towards the substrate when compared to capillary flows towards the contact line. Electrophoretic mobilities and analysis of the timescales confirm the latter. The author would like to point out that the suppression of "stick-slip" behaviour observed for all four concentrations is a combination of the electrophoretic transport of nanoparticles towards the substrate and the hydrophilic effect of the wire that pulls the triple contact line upwards and inwards.

In conclusion, the experimental research carried out under electrowetting conditions has led to two major contributions; firstly the adsorption of particles onto the dielectric substrate triggered by voltage has been proposed, and secondly, the electrophoretic motion of nanoparticles under DC voltage applied in contrast to the hydrodynamic flows reported under AC electric field has been demonstrated.

9.3 Future Work

Once concluded with the remarks and findings achieved during this experimental research, different ideas and further work is included next. The complexity of the non-equilibrium phenomena studied during this experimental research makes each nanoparticle-liquid-substrate system, somewhat, unique. This certainly offers the possibility to study and to uncover new interactions when changing either substrate or nature of the nanoparticles dispersed. Despite the wide range of substrates used

during this experimental research and the study of two different nanoscale particulates, research can be extended to investigate the interactions on structured substrates and for novel and ready available nanoparticles. However this can be an everlasting topic since everyday, new substrates and particles are created. Of special interest would be the study of the structuring and the layering of graphene sheets to try to seize the interactions during pinning and depinning of these fluids.

On other hand, electrowetting has been proposed as one of the most promising techniques for the manipulation of the droplet interface and for the control of the deposits left following evaporation without requiring mechanical parts. Of great significance is the enhancement in electrowetting behaviour of TiO_2 nanoparticles triggered by voltage reported in this experimental work. Thus the study of other fluids rather than TiO_2-water and the use of different EWOD substrates under electrowetting conditions is of paramount importance to expand the knowledge regarding this phenomena.

Of great importance is the study of other nanoparticles varying in size, shape or chemistry, which might lead to novel interactions. For instance, stronger interactions between Al_2O_3 nanoparticles and the dielectric substrate following evaporation of Al_2O_3-water under an external voltage applied were observed. This latter points out towards chemisorption of these nanoparticles onto the substrate since the standard cleaning procedure used during this experimental research was not able to remove these particles from the substrate. A more detailed research to uncover the mechanisms governing the interactions particle-particle, particle-fluid, particle-substrate and fluid-substrate of these particles triggered by voltage is essential.

Since nanofluids have potential applications for cooling purposes, the author would like to explore nanofluid flow in microchannels for single and two-phase heat transfer. The main problem of these nanofluids is sedimentation, erosion or clogging originated by the presence of these particles in suspension, which are exacerbated when scaling the channels down to the microscale. The author would like to take research substrates that will enhance the repulsive charges between particles in suspension and the substrate avoiding sedimentation problems.

References

1. Young, T., *An Essay on the Cohesion of Fluids.* Philosophical Transactions of the Royal Society of London, 1805. **95**: p. 65-87.

2. Dussan V, E.B., *On the Spreading of Liquids on Solid Surfaces: Static and Dynamic Contact Lines.* Annual Review of Fluid Mechanics, 1979. **11**: p. 371-400.

3. de Gennes, P.G., *Wetting: statics and dynamics.* Reviews of Modern Physics, 1985. **57**(3): p. 827.

4. Neinhuis, C. and W. Barthlott, *Characterization and Distribution of Water-repellent, Self-cleaning Plant Surfaces.* Annals of Botany, 1997. **79**(6): p. 667-677.

5. Bonn, D., J. Eggers, J. Indekeu, J. Meunier and E. Rolley, *Wetting and spreading.* Reviews of Modern Physics, 2009. **81**(2): p. 739-805.

6. Zhao, X.-T., K. Sakka, N. Kihara, Y. Takada, M. Arita and M. Masuda, *Structure and photo-induced features of TiO2 thin films prepared by RF magnetron sputtering.* Microelectronics Journal, 2005. **36**(3–6): p. 549-551.

7. Fleming, R.A. and M. Zou, *Fabrication of stable superhydrophilic surfaces on titanium substrates.* Journal of Adhesion Science and Technology, 2012: p. 1-10.

8. Picknett, R.G. and R. Bexon, *The evaporation of sessile or pendant drops in still air.* Journal of Colloid and Interface Science, 1977. **61**(2): p. 336-350.

9. Birdi, K.S., D.T. Vu and A. Winter, *A study of the evaporation rates of small water drops placed on a solid surface.* The Journal of Physical Chemistry, 1989. **93**(9): p. 3702-3703.

10. Birdi, K.S. and D.T. Vu, *Wettability and the evaporation rates of fluids from solid surfaces.* Journal of Adhesion Science and Technology, 1993. **7**(6): p. 485-493.

11. Bourges-Monnier, C. and M.E.R. Shanahan, *Influence of Evaporation on Contact Angle.* Langmuir, 1995. **11**(7): p. 2820-2829.

12. Erbil, H.Y. and R.A. Meric, *Evaporation of Sessile Drops on Polymer Surfaces: Ellipsoidal Cap Geometry*. The Journal of Physical Chemistry B, 1997. **101**(35): p. 6867-6873.

13. Erbil, H.Y., G. McHale and M.I. Newton, *Drop Evaporation on Solid Surfaces: Constant Contact Angle Mode.* Langmuir, 2002. **18**(7): p. 2636-2641.

14. Hu, H. and R.G. Larson, *Evaporation of a Sessile Droplet on a Substrate.* The Journal of Physical Chemistry B, 2002. **106**(6): p. 1334-1344.

15. Cachile, M., O. Bénichou, C. Poulard and A.M. Cazabat, *Evaporating Droplets.* Langmuir, 2002. **18**(21): p. 8070-8078.

16. Panwar, A.K., S.K. Barthwal and S. Ray, *Effect of evaporation on the contact angle of a sessile drop on solid substrates.* Journal of Adhesion Science and Technology, 2003. **17**(10): p. 1321-1329.

17. Sefiane, K., L. Tadrist and M. Douglas, *Experimental study of evaporating Water-Ethanol mixture sessile drop: influence of concentration.* International Journal of Heat and Mass Transfer, 2003. **46**: p. 4527-4534.

18. Hu, H. and R.G. Larson, *Analysis of the Effects of Marangoni Stresses on the Microflow in an Evaporating Sessile Droplet.* Langmuir, 2005. **21**(9): p. 3972-3980.

19. Poulard, C., G. Guéna and A.M. Cazabat, *Diffusion-driven evaporation of sessile drops.* Journal of Physics: Condensed Matter, 2005. **17**(49): p. S4213.

20. Zhang, X., S. Tan, N. Zhao, X. Guo, X. Zhang, Y. Zhang and J. Xu, *Evaporation of Sessile Water Droplets on Superhydrophobic Natural Lotus and Biomimetic Polymer Surfaces.* ChemPhysChem, 2006. **7**(10): p. 2067-2070.

21. Carné-Sánchez, A., I. Imaz, M. Cano-Sarabia and D. Maspoch, *A spray-drying strategy for synthesis of nanoscale metal-organic frameworks and their assembly into hollow superstructures.* Nature Chemistry, 2013. **5**(3): p. 203-211.

22. Dugas, V., J. Broutin and E. Souteyrand, *Droplet Evaporation Study Applied to DNA Chip Manufacturing.* Langmuir, 2005. **21**(20): p. 9130-9136.

23. Man, W. and W.B. Russel, *Direct Measurements of Critical Stresses and Cracking in Thin Films of Colloid Dispersions.* Physical Review Letters, 2008. **100**(19): p. 198302.

24. Manoharan, V.N. and D.J. Pine, *Building Materials by Packing Spheres.* MRS Bulletin, 2004. **29**(02): p. 91-95.

25. Zhang, L., S. Maheshwari, H.-C. Chang and Y. Zhu, *Evaporative Self-Assembly from Complex DNA−Colloid Suspensions.* Langmuir, 2008. **24**(8): p. 3911-3917.

26. Bigioni, T.P., X.-M. Lin, T.T. Nguyen, E.I. Corwin and H.M. Jaeger, *Kinetically driven self assembly of highly ordered nanoparticle monolayers.* Nature Mater, 2006. **5**(4): p. 265-270.

27. Deegan, R.D., *Pattern formation in drying drops.* Physical Review E, 2000. **61**(1): p. 475-485.

28. Deegan, R.D., Bakajin, O., Dupont, T. F., Huber, G., Nagel, S. R. & Witten, T. A., *Capillary flow as the cause of ring stains from dried liquid drops.* Nature, 1997. **389**(6653): p. 827-829.

29. Adachi, E., A.S. Dimitrov and K. Nagayama, *Stripe Patterns Formed on a Glass Surface during Droplet Evaporation.* Langmuir, 1995. **11**(4): p. 1057-1060.

30. Motte, L., F. Billoudet and M.P. Pileni, *Self-Assembled Monolayer of Nanosized Particles Differing by Their Sizes.* The Journal of Physical Chemistry, 1995. **99**(44): p. 16425-16429.

31. Fischer, B.J., *Particle Convection in an Evaporating Colloidal Droplet.* Langmuir, 2001. **18**(1): p. 60-67.

32. Sommer, A.P., M. Ben-Moshe and S. Magdassi, *Size-Discriminative Self-Assembly of Nanospheres in Evaporating Drops.* The Journal of Physical Chemistry B, 2003. **108**(1): p. 8-10.

33. Maheshwari, S., L. Zhang, Y. Zhu and H.-C. Chang, *Coupling Between Precipitation and Contact-Line Dynamics: Multiring Stains and Stick-Slip Motion.* Physical Review Letters, 2008. **100**(4): p. 044503.

34. Gonuguntla, M. and A. Sharma, *Polymer Patterns in Evaporating Droplets on Dissolving Substrates.* Langmuir, 2004. **20**(8): p. 3456-3463.

35. Li, Q., Y. Zhu, I.A. Kinloch and A.H. Windle, *Self-Organization of Carbon Nanotubes in Evaporating Droplets.* The Journal of Physical Chemistry B, 2006. **110**(28): p. 13926-13930.

36. Park, J. and J. Moon, *Control of Colloidal Particle Deposit Patterns within Picoliter Droplets Ejected by Ink-Jet Printing.* Langmuir, 2006. **22**(8): p. 3506-3513.

37. Widjaja, E. and M.T. Harris, *Particle deposition study during sessile drop evaporation.* AIChE Journal, 2008. **54**(9): p. 2250-2260.

38. Bhardwaj, R., X. Fang, P. Somasundaran and D. Attinger, *Self-Assembly of Colloidal Particles from Evaporating Droplets: Role of DLVO Interactions and Proposition of a Phase Diagram.* Langmuir, 2010. **26**(11): p. 7833-7842.

39. Zhang, B.J., J. Park, K.J. Kim and H. Yoon, *Biologically inspired tunable hydrophilic/hydrophobic surfaces: a copper oxide self-assembly multitier approach.* Bioinspiration & Biomimetics, 2012. **7**(3): p. 036011.

40. Masuda, H., A. Ebata, K. Teramae and N. Hishinuma, *Alteration of Thermal Conductivity and Viscosity of Liquid by Dispersing Ultra-Fine Particles. Dispersion of Al_2O_3, SiO_2 and TiO_2 Ultra-Fine Particles.* Netsu Bussei, 1993. **7**(4): p. 227-233.

41. Choi, S.U.S. and J.A. Eastman, *Enhancing Thermal Conductivity of Fluids with Nanoparticles.* Argonne, IL, 1995.

42. Choi, S.U.S., *Nanofluid technology: current status and future research*, in *Korea - U. S. technical conference on strategic technolgies*. 1999: Vienna.

43. Wang, X., X. Xu and S.U. S. Choi, *Thermal Conductivity of Nanoparticle - Fluid Mixture.* Journal of Thermophysics and Heat Transfer, 1999. **13**(4): p. 474-480.

44. Wasan, D.T. and A.D. Nikolov, *Spreading of nanofluids on solids.* Nature, 2003. **423**(6936): p. 156-159.

45. Krishnamurthy, S., P. Bhattacharya, P.E. Phelan and R.S. Prasher, *Enhanced Mass Transport in Nanofluids.* Nano Letters, 2006. **6**(3): p. 419-423.

46. Wong, K.V. and O. De Leon, *Applications of Nanofluids: Current and Future.* Advances in Mechanical Engineering, 2010. **2010**.

47. Saidur, R., K.Y. Leong and H.A. Mohammad, *A review on applications and challenges of nanofluids.* Renewable and Sustainable Energy Reviews, 2011. **15**(3): p. 1646-1668.

48. Paul, S., C. Pearson, A. Molloy, M.A. Cousins, M. Green, S. Kolliopoulou, P. Dimitrakis, P. Normand, D. Tsoukalas and M.C. Petty, *Langmuir−Blodgett Film Deposition of Metallic Nanoparticles and Their Application to Electronic Memory Structures.* Nano Letters, 2003. **3**(4): p. 533-536.

49. Peer, D., J.M. Karp, S. Hong, O.C. Farokhzad and R. Langer, *Nanocarriers as an emerging platform for cancer therapy.* Nat Nano, 2007. **2**(12): p. 751-760.

50. Taylor, R.A., P.E. Phelan, T.P. Otanicar, C.A. Walker, M. Nguyen, S. Trimble and R. Prasher, *Applicability of nanofluids in high flux solar collectors.* Journal of Renewable and Sustainable Energy, 2011. **3**(2): p. 023104.

51. Kinloch, I.A., S.A. Roberts and A.H. Windle, *A rheological study of concentrated aqueous nanotube dispersions.* Polymer, 2002. **43**(26): p. 7483-7491.

52. Tohver, V., A. Chan, O. Sakurada and J.A. Lewis, *Nanoparticle Engineering of Complex Fluid Behavior.* Langmuir, 2001. **17**(26): p. 8414-8421.

53. Phan, H.T., N. Caney, P. Marty, S. Colasson and J. Gavillet, *Surface wettability control by nanocoating: The effects on pool boiling heat transfer and nucleation mechanism.* International Journal of Heat and Mass Transfer, 2009. **52**(23–24): p. 5459-5471.

54. Pauliac-Vaujour, E., A. Stannard, C.P. Martin, M.O. Blunt, I. Notingher, P.J. Moriarty, I. Vancea and U. Thiele, *Fingering Instabilities in Dewetting Nanofluids.* Physical Review Letters, 2008. **100**(17): p. 176102.

55. Vancea, I., U. Thiele, E. Pauliac-Vaujour, A. Stannard, C.P. Martin, M.O. Blunt and P.J. Moriarty, *Front instabilities in evaporatively dewetting nanofluids.* Physical Review E, 2008. **78**(4): p. 041601.

56. Yunker, P.J., T. Still, M.A. Lohr and A.G. Yodh, *Suppression of the coffee-ring effect by shape-dependant capillary interactions.* Nature, 2011. **476**(7360): p. 308-311.

57. Sefiane, K., *Patterns from drying drops.* Advances in Colloid and Interface Science, 2013(0).

58. Orejon, D., K. Sefiane and M.E.R. Shanahan, *Stick–Slip of Evaporating Droplets: Substrate Hydrophobicity and Nanoparticle Concentration.* Langmuir, 2011. **27**(21): p. 12834-12843.

59. Mugele, F. and J.-C. Baret, *Electrowetting: from basics to applications.* Journal of Physics: Condensed Matter, 2005. **17**(28): p. R705.

60. Quilliet, C. and B. Berge, *Electrowetting: a recent outbreak.* Current Opinion in Colloid and Interface Science, 2001. **6**(1): p. 34-39.

61. Lippmann, G., *Relations entre les phénomènes électriques et capillaires*. 1875: Gauthier-Villars.

62. Pollack, M.G., R.B. Fair and A.D. Shenderov, *Electrowetting-based actuation of liquid droplets for microfluidic applications.* Applied Physics Letters, 2000. **77**(11): p. 1725-1726.

63. Brown, C.V., G.G. Wells, M.I. Newton and G. McHale, *Voltage-programmable liquid optical interface.* Nat Photon, 2009. **3**(7): p. 403-405.

64. Mugele, F., A. Staicu, R. Bakker and D. van den Ende, *Capillary Stokes drift: a new driving mechanism for mixing in AC-electrowetting.* Lab on a Chip, 2011. **11**(12): p. 2011-2016.

65. Yeo, L.Y., R.V. Craster and O.K. Matar, *Drop manipulation and surgery using electric fields.* Journal of Colloid and Interface Science, 2007. **306**(2): p. 368-378.

66. Eral, H.B., D.M. Augustine, M.H.G. Duits and F. Mugele, *Suppressing the coffee stain effect: how to control colloidal self-assembly in evaporating drops using electrowetting.* Soft Matter, 2011. **7**(10): p. 4954-4958.

67. Hwang, W.M. and C.Y. Lee, *Separation of nanoparticles in different sizes and compositions by capillary electrophoresis.* Bulletin of the Korean Chemical Society, 2003.

68. Ko, S.H., H. Lee and K.H. Kang, *Hydrodynamic Flows in Electrowetting.* Langmuir, 2008. **24**(3): p. 1094-1101.

69. Millefiorini, S., A.H. Tkaczyk, R. Sedev, J. Efthimiadis and J. Ralston, *Electrowetting of Ionic Liquids.* Journal of the American Chemical Society, 2006. **128**(9): p. 3098-3101.

70. Vallet, M., M. Vallade and B. Berge, *Limiting phenomena for the spreading of water on polymer films by electrowetting.* The European Physical Journal B - Condensed Matter and Complex Systems, 1999. **11**(4): p. 583-591.

71. Mugele, F. and S. Herminghaus, *Electrostatic stabilization of fluid microstructures.* Applied Physics Letters, 2002. **81**(12): p. 2303-2305.

72. Park, J., X.-Q. Feng and W. Lu, *Instability of electrowetting on a dielectric substrate.* Journal of Applied Physics, 2011. **109**(3): p. 034309-6.

73. Sluhan, C.A., *Industrial applications of wetting agents.* Journal of Chemical Education, 1943. **20**(1): p. 38.

74. Gibbs, J.W., H.A. Bumstead and R.G. Van Name, *Scientific Papers of J. Willard Gibbs ...: Thermodynamics*. 1906: Longmans, Green and Company.

75. Dupré, A. and P. Dupré, *Théorie mécanique de la chaleur*. 1869: Gauthier-Villars.

76. Gauss, C.F., J.C. Morehead and A.M. Hiltebeitel, *General investigations of curved surfaces of 1827 and 1825*. 1902: The Princeton university library.

77. Laplace, P.S., Marquis de, 1749-1827, *Traité de mécanique céleste*. Vol. 2. 1799: Paris, Duprat.

78. Zisman, W.A., *Relation of the Equilibrium Contact Angle to Liquid and Solid Constitution*, in *Contact Angle, Wettability, and Adhesion*. 1964, AMERICAN CHEMICAL SOCIETY. p. 1-51.

79. Kabza, K.G., J.E. Gestwicki and J.L. McGrath, *Contact Angle Goniometry as a Tool for Surface Tension Measurements of Solids, Using Zisman Plot Method. A Physical Chemistry Experiment.* Journal of Chemical Education, 2000. **77**(1): p. 63.

80. Shanahan, M.E.R., *Effects of surface flaws on the wettability of solids.* Journal of Adhesion Science and Technology, 1992. **6**: p. 489-501.

81. Marmur, A. and M.D. Lelah, *The spreading of aqueous surfactant solutions on glass.* Chemical Engineering Communications, 1981. **13**(1-3): p. 133-143.

82. Beni, G. and S. Hackwood, *Electro-wetting displays.* Applied Physics Letters, 1981. **38**(4): p. 207-209.

83. McHale, G., C.V. Brown, M.I. Newton, G.G. Wells and N. Sampara, *Dielectrowetting Driven Spreading of Droplets.* Physical Review Letters, 2011. **107**(18): p. 186101.

84. Maddox, D.E. and I. Mudawar, *Single- and Two-Phase Convective Heat Transfer From Smooth and Enhanced Microelectronic Heat Sources in a Rectangular Channel.* Journal of Heat Transfer, 1989. **111**(4): p. 1045-1052.

85. Forbes, R.J., *A short history of the art of distillation*. 1970: Brill.

86. Moffat, J.R., *Experimental investigation into the evaporating behaviour of pure and nanofluid droplets*, in *School of Engineering*. 2011, University of Edinburgh.

87. Morse, H.W., *On Evaporation from the Surface of a Solid Sphere. Preliminary Note.* Proceedings of the American Academy of Arts and Sciences, 1910. **45**(14): p. 363-367.

88. McHale, G., S.M. Rowan, M.I. Newton and M.K. Banerjee, *Evaporation and the Wetting of a Low-Energy Solid Surface.* The Journal of Physical Chemistry B, 1998. **102**(11): p. 1964-1967.

89. Shanahan, M.E.R., K. Sefiane and J.R. Moffat, *Dependence of Volatile Droplet Lifetime on the Hydrophobicity of the Substrate.* Langmuir, 2011. **27**(8): p. 4572-4577.

90. Chandra, S., M. di Marzo, Y.M. Qiao and P. Tartarini, *Effect of liquid-solid contact angle on droplet evaporation.* Fire Safety Journal, 1996. **27**(2): p. 141-158.

91. Gelderblom, H., Á.G. Marín, H. Nair, A. van Houselt, L. Lefferts, J.H. Snoeijer and D. Lohse, *How water droplets evaporate on a superhydrophobic substrate.* Physical Review E, 2011. **83**(2): p. 026306.

92. Maxwell, J.C., *Diffusion.* In Encycolpedia Britannica (Ninth ed.), 1878a. **7**: p. 214-221.

93. Fuchs, N.A., *Evaporation and droplet growth in gaseous media*. 1959, London: Pergamon Press.

94. Smith, R.A., *The life and works of Thomas Graham, D.C.L., F.R.S.* 1884: Glasgow: J. Smith & Sons.

95. Yakhno, T.A., O.A. Sedova, A.G. Sanin and A.S. Pelyushenko, *On the existence of regular structures in liquid human blood serum (plasma) and phase transitions in the course of its drying.* Technical Physics, 2003. **48**(4): p. 399-403.

96. Sefiane, K., *On the Formation of Regular Patterns from Drying Droplets and Their Potential Use for Bio-Medical Applications.* Journal of Bionic Engineering, 2010. **7, Supplement**(0): p. S82-S93.

97. Askounis, A., D. Orejon, V. Koutsos, K. Sefiane and M.E.R. Shanahan, *Nanoparticle deposits near the contact line of pinned volatile droplets: size and shape revealed by atomic force microscopy.* Soft Matter, 2011.

98. Marín, Á.G., H. Gelderblom, D. Lohse and J.H. Snoeijer, *Order-to-Disorder Transition in Ring-Shaped Colloidal Stains.* Physical Review Letters, 2011. **107**(8): p. 085502.

99. Blossey, R. and A. Bosio, *Contact Line Deposits on cDNA Microarrays: A "Twin-Spot Effect"*. Langmuir, 2002. **18**(7): p. 2952-2954.

100. Maxwell, J.C., *A treatise on electricity and magnetism*. 1873: Oxford: Clarednon Press.

101. Einstein, A., *Eine neue Bestimmung der Moleküldimensionen.* Annalen der Physik, 1906. **324**(2): p. 289-306.

102. Deegan, R.D., O. Bakajin, T. Dupont, G. Huber, S. Nagel and T. Witten, *Contact line deposits in an evaporating drop.* Physical Review E, 2000. **62**(1): p. 756-765.

103. Hu, H. and R.G. Larson, *Analysis of the Microfluid Flow in an Evaporating Sessile Droplet.* Langmuir, 2005. **21**(9): p. 3963-3971.

104. Hu, H. and R.G. Larson, *Marangoni Effect Reverses Coffee-Ring Depositions.* The Journal of Physical Chemistry B, 2006. **110**(14): p. 7090-7094.

105. Wong, T.-S., T.-H. Chen, X. Shen and C.-M. Ho, *Nanochromatography Driven by the Coffee Ring Effect.* Analytical Chemistry, 2011. **83**(6): p. 1871-1873.

106. Moffat, J.R., K. Sefiane and M.E.R. Shanahan, *Effect of TiO_2 Nanoparticles on Contact Line Stick−Slip Behavior of Volatile Drops.* The Journal of Physical Chemistry B, 2009. **113**(26): p. 8860-8866.

107. Sefiane, K., *On the role of structural disjoining pressure and contact line pinning in critical heat flux enhancement during boiling of nanofluids.* Applied Physics Letters, 2006. **89**(4): p. 044106.

108. Maenosono, S., C.D. Dushkin, S. Saita and Y. Yamaguchi, *Growth of a Semiconductor Nanoparticle Ring during the Drying of a Suspension Droplet.* Langmuir, 1999. **15**(4): p. 957-965.

109. Eral, H.B., D. van den Ende and F. Mugele, *Say goodbye to coffee stains.* Physics World, 2012. **April 2012**.

110. Grier, D.G., *A revolution in optical manipulation.* Nature, 2003. **424**(6950): p. 810-816.

111. Darhuber, A., J. Valentino, S. Trojan and S. Wagner, *Microfluidic actuation by modulation of surface stresses.* Applied Physics Letters, 2003. **82**: p. 657-659.

112. Wixforth, A., C. Strobl, C. Gauer, A. Toegl, J. Scriba and Z. v Guttenberg, *Acoustic manipulation of small droplets.* Analytical and bioanalytical chemistry, 2004. **379**(7-8): p. 982-991.

113. Tsai, Y.-T., C.-H. Choi and E.-H. Yang, *Low-Voltage Manipulation of an Aqueous Droplet in a Microchannel via Tunable Wetting on PPy(DBS).* Lab on a Chip, 2012.

114. Hayes, R.A. and B.J. Feenstra, *Video-speed electronic paper based on electrowetting.* Nature, 2003. **425**(6956): p. 383-385.

115. Krupenkin, T. and J.A. Taylor, *Reverse electrowetting as a new approach to high-power energy harvesting.* Nature communications, 2011. **2**: p. 448.

116. Sobel, A., *Electronic paper: High-speed inks.* Nature Mater, 2003. **2**(10): p. 643-644.

117. Kuiper, S. and B.H.W. Hendriks, *Variable-focus liquid lens for miniature cameras.* Applied Physics Letters, 2004. **85**(7): p. 1128-1130.

118. Kim, D.Y. and A.J. Steckl, *Electrowetting on Paper for Electronic Paper Display.* ACS Applied Materials & Interfaces, 2010. **2**(11): p. 3318-3323.

119. Orejon, D., K. Sefiane and M.E.R. Shanahan, *Young-Lippmann equation revisited for nano-suspensions.* Applied Physics Letters, 2013. **102**(20): p. 201601.

120. Orejon, D., K. Sefiane and M.E.R. Shanahan, *Evaporation of Nanofluid Droplets with Applied DC Potential.* Journal of Colloid and Interface Science, 2013(0).

121. Gibbs, J.W., *On the equilibrium of heterogeneous substances [microform] / by J. Willard Gibbs*. 1874, [New Haven :: The Academy.

122. Mugele, F. and J. Buehrle, *Equilibrium drop surface profiles in electric fields.* Journal of Physics: Condensed Matter, 2007. **19**(37): p. 375112.

123. Quinn, A., R. Sedev and J. Ralston, *Contact Angle Saturation in Electrowetting.* The Journal of Physical Chemistry B, 2005. **109**(13): p. 6268-6275.

124. Papathanasiou, A.G., A.T. Papaioannou and A.G. Boudouvis, *Illuminating the connection between contact angle saturation and dielectric breakdown in electrowetting through leakage current measurements.* Journal of Applied Physics, 2008. **103**(3): p. 034901.

125. Dash, R.K., T. Borca-Tasciuc, A. Purkayastha and G. Ramanath, *Electrowetting on dielectric-actuation of microdroplets of aqueous bismuth telluride nanoparticle suspensions.* Nanotechnology, 2007. **18**(47): p. 475711.

126. Roques-Carmes, T., F. Aldeek, L. Balan, S. Corbel and R. Schneider, *Aqueous dispersions of core/shell CdSe/CdS quantum dots as nanofluids for electrowetting.* Colloids and Surfaces A: Physicochemical and Engineering Aspects, 2011. **377**(1–3): p. 269-277.

127. Berge, B., *Electrocapillarité et mouillage de films isolants par l'eau.* Comptes Rendus de l'Academie de Sciences. Serie III, Scviences de la Vie (Paris), 1993. **317**.

128. Saeki, F., J. Baum, H. Moon, J.-Y. Yoon, C.-J. Kim and R.L. Garrell, *Electrowetting on Dielectrics (EWOD): Reducing Voltage Requirements for Microfluidics.* Polym. Mater. Sci. Eng., 2001. **85**: p. 115-116.

129. Li, Y., W. Parkes, L.I. Haworth, A. Ross, J. Stevenson and A.J. Walton, *Room-Temperature Fabrication of Anodic Tantalum Pentoxide for Low-Voltage Electrowetting on Dielectric (EWOD).* Journal of Microelectromechanical Systems, 2008. **17**(6): p. 1481-1488.

130. Reuss, F.F., *Notice sur un nouvel effet de l'électricité galvanique*. 1809.

131. Lee, J.-K., *Surface Charge Effects on Particulate Retention by Microporous Membrane Filters in Liquid Filtration.* Environmental Engineering Research, 1998. **3**(2): p. 97-104.

132. Lee, P.F., *Electrophoretic studies of surface charge on unicellular bacteria*, in *Faculty of Science*. 2009, University of Malaya.

133. Bandy, J., Q. Zhang and C. Guozhong, *Electrophoretic Deposition of Titanium Oxide Nanoparticle Films for Dye-Sensitized Solar Cell Applications.* Materials Sciences and Applications, 2011. **2**(10): p. 1427-1431.

134. Surugau, N. and P.L. Urban, *Electrophoretic methods for separation of nanoparticles.* Journal of Separation Science, 2009. **32**(11): p. 1889-1906.

135. Golovko, D.S., H.-J.r. Butt and E. Bonaccurso, *Transition in the Evaporation Kinetics of Water Microdrops on Hydrophilic Surfaces.* Langmuir, 2008. **25**(1): p. 75-78.

136. BIC, *Instruction Manual for ZetaPALS, Zeta Potential Analyzer*, ed. B.I. Corporation. 1999, New York.

137. Cazabat, A.-M. and G. Guena, *Evaporation of macroscopic sessile droplets.* Soft Matter, 2010. **6**(12): p. 2591-2612.

138. Anderson, D.M. and S.H. Davis, *The spreading of volatile liquid droplets on heated surfaces.* Physics of Fluids, 1995. **7**(2): p. 248-265.

139. Sefiane, K., J. Skilling and J. MacGillivray, *Contact line motion and dynamic wetting of nanofluid solutions.* Advances in Colloid and Interface Science, 2008. **138**(2): p. 101-120.

140. Craster, R.V., O.K. Matar and K. Sefiane, *Pinning, Retraction, and Terracing of Evaporating Droplets Containing Nanoparticles.* Langmuir, 2009. **25**(6): p. 3601-3609.

141. Shanahan, M.E.R., *Simple Theory of "Stick-Slip" Wetting Hysteresis.* Langmuir, 1995. **11**(3): p. 1041-1043.

142. Shanahan, M.E.R. and K. Sefiane, *Contact Angle, Wettability and Adhesion*. 2009: Mittal, K. L. - Brill Academic Pub.

143. Duursma, G.R., K. Sefiane and S. David, *Advancing and receding contact lines on patterned structured surfaces.* Chemical Engineering Research and Design, 2010. **88**(5-6): p. 737-743.

144. Heslot, F., N. Fraysse and A.M. Cazabat, *Molecular Layering in the Spreading of Wetting Liquid-Drops.* Nature, 1989. **338**(6217): p. 640-642.

145. Aoki, I., *Analysis of characteristics of water flash evaporation under low-pressure conditions.* Heat Transfer—Asian Research, 2000. **29**(1): p. 22-33.

146. Hutter, C., K. Sefiane, T.G. Karayiannis, A.J. Walton, R.A. Nelson and D.B.R. Kenning, *Nucleation site interaction between artificial cavities during nucleate pool boiling on silicon with integrated micro-heater and temperature micro-sensors.* International Journal of Heat and Mass Transfer, 2012. **55**(11–12): p. 2769-2778.

147. Kandlikar, S.G., *A General Correlation for Saturated Two-Phase Flow Boiling Heat Transfer Inside Horizontal and Vertical Tubes.* Journal of Heat Transfer, 1990. **112**(1): p. 219-228.

148. Kuo, C.-J. and Y. Peles, *Critical heat Flux of Water at Subatmospheric Pressures in Microchannels.* Journal of Heat Transfer, 2008. **130**(7).

149. Zheng, Z., X. Liu, Y. Luo, B. Cheng, D. Zhang, Q. Meng and Y. Wang, *Pressure controlled self-assembly of high quality three-dimensional colloidal photonic crystals.* Applied Physics Letters, 2007. **90**(5): p. 051910-3.

150. Askounis, A., K. Sefiane, V. Koutsos and M.E.R. Shanahan, *Structural transitions in a ring stain created at the contact line of evaporating nanosuspension sessile drops.* Physical Review E, 2013. **87**(1): p. 012301.

151. Sefiane, K., S.K. Wilson, S. David, G.J. Dunn and B.R. Duffy, *On the effect of the atmosphere on the evaporation of sessile droplets of water.* Physics of Fluids, 2009. **21**(6): p. 062101-9.

152. Rowan, S.M., M.I. Newton and G. McHale, *Evaporation of Microdroplets and the Wetting of Solid Surfaces.* The Journal of Physical Chemistry, 1995. **99**(35): p. 13268-13271.

153. Berge, B. and J. Peseux, *Variable focal lens controlled by an external voltage: An application of electrowetting.* The European Physical Journal E, 2000. **3**(2): p. 159-163.

154. Moon, H., S.K. Cho, R.L. Garrell and C.-J.C.J. Kim, *Low voltage electrowetting-on-dielectric.* Journal of Applied Physics, 2002. **92**(7): p. 4080-4087.

155. Shapiro, B., H. Moon, R.L. Garrell and C.-J.C.J. Kim, *Equilibrium behavior of sessile drops under surface tension, applied external fields, and material variations.* Journal of Applied Physics, 2003. **93**(9): p. 5794-5811.

156. Paneru, M., C. Priest, R. Sedev and J. Ralston, *Static and Dynamic Electrowetting of an Ionic Liquid in a Solid/Liquid/Liquid System.* Journal of the American Chemical Society, 2010. **132**(24): p. 8301-8308.

157. Shanahan, M.E.R., M.-C. Houzelle and A. Carré, *Strange Spreading Behavior of Tricresyl Phosphate.* Langmuir, 1998. **14**(2): p. 528-532.

158. Ward, C.A. and K. Sefiane, *Adsorption at the solid–liquid interface as the source of contact angle dependence on the curvature of the three-phase line.* Advances in Colloid and Interface Science, 2010. **161**(1–2): p. 171-180.

159. Kinge, S., M. Crego-Calama and D.N. Reinhoudt, *Self-assembling nanoparticles at surfaces and interfaces.* Chemphyschem : a European journal of chemical physics and physical chemistry, 2008. **9**(1): p. 20-42.

160. Mampallil, D., H.B. Eral, D. van den Ende and F. Mugele, *Control of evaporating complex fluids through electrowetting.* Soft Matter, 2012. **8**(41): p. 10614-10617.

161. García-Sánchez, P., A. Ramos and F. Mugele, *Electrothermally driven flows in ac electrowetting.* Physical Review E, 2010. **81**(1): p. 015303.

162. Hayward, R.C., D.A. Saville and I.A. Aksay, *Electrophoretic assembly of colloidal crystals with optically tunable micropatterns.* Nature, 2000. **404**(6773).

163. Velev, O.D. and K.H. Bhatt, *On-chip micromanipulation and assembly of colloidal particles by electric fields.* Soft Matter, 2006. **2**(9): p. 738-750.

164. Popov, Y.O., *Evaporative deposition patterns: Spatial dimensions of the deposit.* Physical Review E, 2005. **71**(3): p. 036313.

165. Lyklema, J.H., *Fundamentals of Interface and Colloid Science: Solid-Liquid Interfaces*. 1995: Acad. Press.

166. Shaw, D.J., *Introduction to Colloid and Surface Chemistry*. 4th ed. 1992: Butterworth-Heinemann / Elsevier Science, Oxford.

167. Hückel, E., Phys. Z., 1924. **25**(204-10).

168. Hussain, S., S. Smulders, V. De Vooght, B. Ectors, S. Boland, F. Marano, K. Van Landuyt, B. Nemery, P. Hoet and J. Vanoirbeek, *Nano-titanium dioxide modulates the dermal sensitization potency of DNCB.* Particle and Fibre Toxicology, 2012. **9**(1): p. 15.

169. Tso, C.P., C.M. Zhung, Y.H. Shih, Y.M. Tseng, S.C. Wu and R.A. Doong, *Stability of metal oxide nanoparticles in aqueous solutions.* Water science and technology: a journal of the International Association on Water Pollution Research, 2010. **61**(1): p. 127-133.

170. Jones, T.B., *Electromechanics of Particles*. 1995: Cambridge University Press.

171. Landau, L.D., E.M. Lifshitz and L.P. Pitaevskiĭ, *Electrodynamics of continuous media*. 1984: Pergamon.